Toward Functional Imaging of the Placenta

Gordon N. Stevenson

Lady Margaret Hall

University of Oxford

A thesis submitted for the degree of

Doctor of Philosophy

Trinity 2012

Acknowledgements

First and foremost, I wish to thank my supervisor, Professor Alison Noble, for her encouragement, patience and effort throughout the course of writing this thesis.

I am grateful to the Oxford Biomedical Research Centre and the Oxford Fetal Medicine Unit for funding my research. I owe Mr Laurence Impey a debt of gratitude for his belief in my work and the provision of an extra year's funding. His ideas and encouragement for 'cracking' some of the problems we encountered along the way are deeply appreciated.

A DPhil for some can be a lonely pursuit however I have been lucky enough to work with the best clinician an engineer could have. Dr Sally Collins has been a great colleague and friend throughout my time at Oxford. Her boundless enthusiasm and determination has gone a long way to make this work possible. I hope our research partnership will continue long after submitting this work. Thanks go to Prof. Alec Welsh for his expertise on Doppler estimation and his willingness to be cajoled back into this area of research.

Drs J.D Morrison and Paul Siebert must be acknowledged for their mentoring and introducing me to the realms of physiology and image analysis, respectively, whilst at Glasgow University. Without my exposure to these subjects and their tuition this DPhil would not have been possible.

Thanks also go to my labmates at the IBME, in particular those handy with a cafetèrie, and my peers in Lady Margaret Hall's MCR. The college's support towards conference expenses is appreciated as well as my teammates from the rugby and rowing clubs who provided so much fun as well as lasting friendships.

Finally, thanks must go to my family for their help, advice, love and support throughout this enterprise. In particular, my little sister Lyndsay (a doctor who can actually help people!) and my Mum and Dad. This thesis is dedicated to them.

Statement of Originality

This thesis is submitted to the Department of Engineering Science, University of Oxford, in fulfillment of the requirements for the degree of Doctor of Philosophy. The thesis is entirely my own work and, except where otherwise stated, describes my own research.

Gordon Stevenson, Lady Margaret Hall, University of Oxford.

Abstract

In obstetrics, the application of computer-based image analysis to provide deeper insight into pathology in early pregnancy is highly desirable but underdeveloped. One such pathology, fetal growth restriction (FGR) is a leading cause of mortality and morbidity in pregnancy. FGR affects approximately 3-10% of pregnancies in the western world leading to increased risk of stillbirth and health problems in later life. Morphometric or functional measurement of the placenta in pregnancy *in utero* may aid diagnosis of this pathology as the interface between placenta and mother is the site where the pathology manifests itself. Detection of growth restriction is yet to be resolved as poor, unreliable biochemical and image-based biomarkers have made it hard to detect and manage these pregnancies effectively.

By the provision and development of tools for quantification of the placenta by three dimensional (3D) ultrasound (US) using image segmentation and mesh processing, this thesis aims to better facilitate clinical investigation of this major problem in obstetric healthcare.

In a first contribution, 3D placental volume measurement using 3D US is used to classify the difference between normal and FGR pregnancies. Volume was estimated using the semi-automated random walker (RW) algorithm. The repeatability and reliability of the method was tested between three observers and showed the new method to be equivalent to manual segmentation. In a study of 143 women performed by our clinical partners, significantly smaller placental volume was found in pregnancies defined as small-for-gestational age (SGA).

Expanding on volumetry, the utero-placental interface (UPI) is the location where the pathology that leads to FGR occurs. Manual manipulation of the volume is required to visualise the interface, so we investigated applying a "mesh flattening" process to convert the contorted UPI into a disc to provide a standardised way to view the interface between acquistions and subjects.

Finally, an existing, two dimensional (2D) Doppler standardisation technique was extended into 3D to provide standardisation of values of Doppler vascularity. This technique was then applied to measure the vascularity of volumes of interest relative to the interface between placenta and mother. This test was then applied clinically in 143 women and found that the vascularity of the small-for-gestational age (SGA) pregnancies was significantly smaller than that of the population who produced appropriately sized babies.

These three tools each provide augmentation of our understanding of placental health and function in pregnancy. From measuring the gross volume to estimating the blood flow we show the potential clinical application for image analysis performed on 3D power Doppler (PD) ultrasound volumes.

Contents

List of Figures

List of Tables

List of Acronyms

2D	two dimensional
3D	three dimensional
4D	four dimensional
A-mode	amplitude-mode
ADAM12s	Disintegrin and metalloproteinase domain-containing protein 12
AGA	appropriate for gestational age
AUC	area under the curve
B-mode	brightness-mode
BiCG	biconjugate gradient stabilized method
BMI	body mass index
CFI	colour flow imaging
CG	conjugate gradient
CPD	colour pixel density
cPDF	cumulative probability density function
CRL	crown-rump length
CNR	contrast to noise ratio
CT	computed tomography
CW	continuous wave
EDT	Euclidean distance transform
FGR	fetal growth restriction
FMBV	fractional moving blood volume
fMRI	functional magnetic resonance imaging
FI	flow index
GE	General Electric
GPU	graphics processing unit
GS	Gordon Stevenson
ICC	intra class correlation co-efficient
ITK	insight toolkit

IUGR	intra-uterine growth restriction
IVS	intervillous space
LOA	limits of agreement
JD	Dr. Jane Ding
MIP	Maximum intensity projection
MoMs	multiples of the median
MPI	mean pixel intensity
MPR	multi-planar reconstruction
MRI	magnetic resonance imaging
NHS	national health service
NICU	neonatal intensive care unit
NT	nuchal translucency
PAPP-A	pregnancy associated plasma protein-A
PD	power Doppler
PET	positron emission tomography
PI	pulsatility index
PP13	placental protein 13
PQ	placental quotient
PRF	pulse repetition frequency
PW	pulsed wave
RBC	red blood cell
REC	research ethics service
ROC	receiver-operating characteristics
ROI	region of interest
RI	resistance index
RMS	radioactive microspheres
RW	random walker
SC	Dr. Sally Collins
SCBU	special care baby unit
SE	standard error
SGA	small-for-gestational age
SNG	sub-noise gain
TRUS	trans-rectal ultrasound
TUI	Tomographic Ultrasound Imaging
UPI	utero-placental interface
US	ultrasound
VI	vascularisation index
VFI	vascularity flow index
VOI	volume of interest

VOCAL™ Virtual Organ Computer-aided AnaLysis

VNL visual numeric library

Chapter 1

Introduction

In the last twenty years it has become apparent that the first scheduled visit of a pregnant women to hospital at 11-13 weeks is increasingly more important as patient-specific risk of chromosomal and other disorders can be identified at this early stage in pregnancy. The combination of maternal characteristics, patient history and biochemical and biophysical tests can define the risk for a variety of complications including miscarriage, stillbirth, diabetes, macrosomia and fetal growth restriction[1]. As a result, there is increasing clinical interest in the use of any marker, biochemical or image-based, that can predict with greater accuracy any potential risk of disease or complication in pregnancy.

With the increasing ubiquity of 3D ultrasound technology that can function in real time in a clinical setting this leads to the pursuit of whether volumetric measurement of the placenta can provide any kind of imaging biomarker. As placental weight at term is known to correlate with outcome[2] we wish to investigate whether placental markers such as volume (and others that can derived from the segmentation of the organ) *in utero* can predict potential risk. As a starting point, whether placental volume can

indicate those babies at risk of being below the tenth centile of the overall population and so classed as SGA is an important clinical question. This is because these small babies at term are at greater risk of complications *in utero* and in later life[3] so accurate prediction of their outcome that can lead to better management of them as a high risk population is important for their development and beyond.

The goals of this thesis are clearly clinically based however they can only be accomplished with the provision of medical imaging tools to provide the placental volume measurements. Beyond volumetric measurement of the placenta, this thesis describes a new method to visualise the interface where maternal blood enters the placenta and extend this method into taking measurement of the blood flow derived from Doppler ultrasound at and around this anatomical boundary. Currently, the adoption of 3D ultrasound has been limited due to the reliance of tools that are either bespoke to a particular manufacturer or require training or manual manipulation to provide repeatable results. The application of an automated solution that can reduce the complexity of the problem and move away from manual interaction should allow clinicians to generate results across large portions of data and provide additional insight into the interactions between placenta and mother. The tools we describe although aimed specifically at the problems described above are defined generally and have potential application in other imaging areas, beyond obstetrical medical ultrasound.

1.1 Main Contributions

The contributions of this thesis are threefold:

- ◇ The implementation and adaptation of an existing graph-based 3D segmentation algorithm, Random Walker, for the calculation of placental volume.
- ◇ A new visualisation technique for viewing the interface between the uterus and placenta using a combination of B-mode and power Doppler 3D ultrasound.
- ◇ Measurement of utero/placental blood flow with 3D power Doppler ultrasound at the anatomical interface of the placenta and uterus in normal and SGA fetuses using a pre-existing standardisation technique adapted for 3D use, for the first time.

1.2 Thesis Overview

This thesis is organised into an introduction, literary critique and three chapters based upon the contributions stated in section 1.1 with a final chapter that concludes the work and outlines future work based upon these contributions. Chapter 2 introduces placental physiology and pathology and in particular fetal growth restriction from a clinical perspective. Technical aspects of the work such as image segmentation, ultrasound physics, 3D acquisition methodology and current visualisation and Doppler measurement techniques are also summarised. As this thesis marries together many different ideas from the fields of obstetric medicine and biomedical engineering a large review of the current state of art is required to show the foundations on which this work is built and how it will advance the field.

Chapter 3 introduces placental volume segmentation and the work we have performed on implementation and validation of an existing technique for 3D placental segmentation. Based upon these segmentations, chapter 4 describes a new visualisation method which allows automated viewing of the most clinically interesting area of the placenta and from this allows automated functional quantification of the placenta as shown in Chapter 6. These three contributions described in their respective chapters when combined together provide a framework that provides a variety of new measures for the placenta. These can be used clinically on a population of normal and SGA fetuses to show whether these new metrics can accurately detect growth restriction at the 11-13 week scan.

1.3 Publications arising from this work

1.3.1 Oral presentations at international conferences

- G.N. Stevenson, S.L. Collins, L.W. Impey and J.A. Noble. "An image processing technique for 3-D fractional moving blood volume (FMBV) estimation using power Doppler ultrasound (PD-US)", 22nd World Congress on Ultrasound in Obstetrics and Gynecology, Copenhagen, Denmark, September 2012. *Awarded best presentation in "Imaging Technologies" category.*

- S.L. Collins, G.N. Stevenson, L.W. Impey and J.A. Noble. "Utero-placental interface vascularity in early pregnancy estimated by 3D fractional moving blood volume (3D FMBV) predicts fetal growth restriction." 22nd World Congress on Ultrasound in Obstetrics and Gynecology, Copenhagen, Denmark, September 2012. *Awarded best presentation in "Maternal fetal Doppler" category.*

- S.L. Collins, G.N. Stevenson, L.W. Impey and J.A. Noble. "Size is everything: the search for a 3-D morphometric marker to predict fetal growth restriction", International Federation of Placenta Associations (IFPA) Meeting, Geilo, Norway, September 2011. *Awarded the Trophoblast Research New Investigator Award.*

- G.N. Stevenson, S.L. Collins, L.W. Impey and J.A. Noble. "Surface Parameterisation of the Utero/Placental Interface using 3D power Doppler Ultrasound", IEEE International Symposium of Biomedical Imaging (ISBI), Chicago, USA, March 2011.

- G.N. Stevenson, S. L. Collins, L. Impey and J.A. Noble. "A novel semi-automated (SA) technique for 3D ultrasound measurement of placental volume", 20th World Congress on Ultrasound in Obstetrics and Gynecology, Prague, Czech Republic, September 2010.

1.3.2 Publications in peer reviewed journals

- S.L. Collins, G.N. Stevenson, J.A. Noble, L.W. Impey, and A. Welsh,(2011) "Influence of power Doppler gain setting on Virtual Organ Computer AnaLysis (VOCAL^{TM}) indices *in vivo*: Can use of the individual sub-noise gain (SNG) level optimise information?" Ultrasound in Obstetrics & Gynecology (*in press*).

- A.W. Welsh, S.L. Collins, G.N. Stevenson, J.A. Noble and L.W. Impey,(2012) "Inapplicability of the Fractional Moving Blood Volume (FMBV) technique to standardise VOCAL indices for quantified power Doppler", Ultrasound in Obstetrics & Gynecology (*in press*).

1.3.3 Patent applications

- G.N Stevenson, S.L. Collins, L.W. Impey, and J.A. Noble, "Transformation of a three-dimensional flow image", Filing date 25th January 2012, Publication date 9th August 2012. Publication number WO 2012/104577.

Chapter 2

Background and Literary Critique

A broad background review is required to outline the rationale behind quantifying placental function as well as the tools required to solve this challenge as the contributions of this thesis combine aspects of physiology, computer graphics, ultrasound imaging and image processing.

This chapter begins in section 2.1 by reviewing the anatomy, physiology, function and vascular structure of the placenta. The mechanism of utero-placental insufficiency and its adverse effect upon pregnancy resulting in growth restriction is described in section 2.2 as well as the motivation to perform placental quantification and analysis during pregnancy. Quantification *in utero* is performed on acquisitions of 3D pulse-echo and Doppler ultrasound volumes of the organ. The physics and engineering behind this imaging technology is outlined in section 2.3. To provide placental volumetry measurements an image segmentation technique is applied to the ultrasound volumes. The field of segmentation is summarised in section 2.4. Finally, an outline of current methods to visualise objects in 3D volumes produced in medical imaging is discussed in section 2.5.

2.1 Placental Anatomy

The placenta is an organ that provides nutritional support for the unborn child throughout pregnancy. It performs a wide range of physiological functions which after birth are performed by the lungs, digestive tract, endocrine glands and kidneys of the newborn. It mediates the transfer of respiratory gases, water and nutrients as well as the secretion of a wide array of hormones, cytokines and signalling molecules[4]. As well as these functions the placenta provides an immunological cloak to hide the fetus from any maternal immune response during pregnancy. At term the placenta is typically discoid in shape, with approximate dimensions of 9.0 x 9.0 x 2.25cm[5]. It arises as a portion of the cells from the original conceptus of cells produced at fertilisation (therefore sharing the same genetic makeup as the fetus) and develops in parallel with the embryo to provide nutrient and waste exchange via the mother's blood supply.

Figure 2.1 illustrates the location of the placenta *in utero* and also the shape of the two sides of the organ from the perspective of the maternal tissue and the uterine cavity. Figure 2.1 shows the smooth maternal side of the placenta divided into functional units (cotyledons). This differs to the fetal side which is illustrated in both figure 2.1 and 2.2 as containing a thick bundle of veins and arteries that splay out into the individual

The diagram showing placental location and illustration of maternal and fetal side of the placenta at late pregnancy originally presented here cannot be made freely available via ORA because of copyright. The diagram was sourced at Medline Plus (online).[6]

Figure 2.1: Diagram showing placental location *in utero* and illustration of maternal and fetal side of the placenta at late pregnancy. Taken from Medline Plus (online)[6].

branches of vasculature that support the finger-like chorionic villi that are the site of nutritional transfer in the placenta.

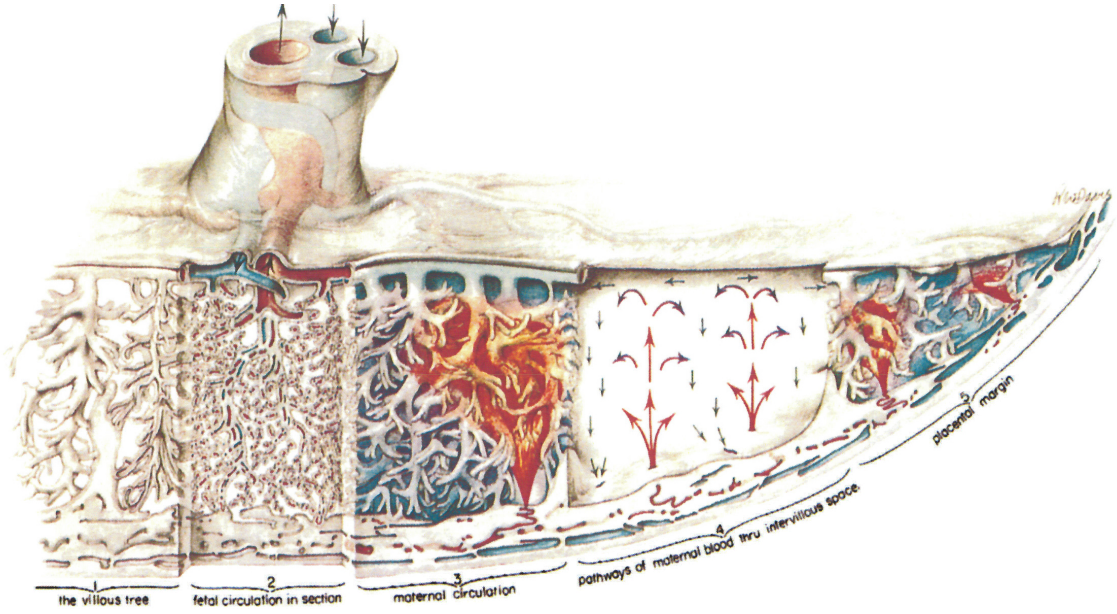

Figure 2.2: The structure and circulation of the human placenta. Section 1 shows the gross anatomy of the villi, section 2 the fetal circulation and sections 3 and 4 of the diagram shows the pattern of maternal blood flow out of the spiral arterioles into fountain-like streams. Reproduced by permission of the Carnegie Institute, Washington[7].

The placenta provides a location for the exchange of nutrients without the mixing of the blood of fetus and mother. This compartmentalisation of different blood systems was first discovered by the Scottish anatomist William Hunter in the 18th century[8]. He outlined the conveyance of maternal blood into the intervillous space (IVS) of the placenta from the maternal spiral arterioles and the action of the blood bathing the villi in nutrient rich blood. By diffusion, respiratory gases and nutrients pass between the thin tissue layer that separates the intervillous space from the villi. The villi are supplied by the chorionic vessels of the fetal side of the placenta. Once nutrients are transferred they are carried from the villus tree by the fetal circulation via the umbilical

vessels to the developing baby. A lithograph illustrating placental structure and the area of nutritional exchange between mother and placenta is shown in Figure 2.2. It shows in detail the placental villi, the umbilical artery and veins that supply the fetus with nutrition as well as the dynamics of the blood movement into and out of the placenta.

As well as his discovery of two separate circulatory systems within the placenta, Hunter was the first to describe the uterine lining as “decidua”, from the latin “decidere” meaning to “to fall off”. The etymology is significant as it describes the sloughing action of the tissue during menstruation and parturition and has implications for the anatomy of the spiral arterioles that supply this tissue with blood. This has consequences to the anatomy of the spiral arterioles which is discussed later in section 2.1.1.1 but first the anatomy of the uterus needs to be further understood.

Figure 2.3 illustrates the three distinct layers of tissue in the uterus. From furthest from where the placenta attaches to the uterine wall is the perimetrium, then to the intermediate muscular layer of the myometrium and finally the endometrium or decidua in pregnancy. At the level of the decidua, there are two distinct sections - the *basal plate* and the *placental bed*. The portion that adheres to the placenta and forms the bottom portion of the IVS is defined as the *utero-placental interface (UPI)* and is illustrated in Figure 2.2. For the purposes of this thesis, the ”utero-placental interface” refers to the maternal-fetal interface, which is effectively the floor of the IVS and the plane along which the placenta separates from the uterus[9] at birth. Figure 2.2 also shows the *placental bed* which is the part of the decidua that remains as part of the uterus at parturition. With this nomenclature defined, we can now investigate the vascular structure of the uterus and how it alters to the demands of pregnancy in the next section.

2.1.1 Anatomy and Physiology of the Uterine Vasculature System

The uterus is supplied by the two uterine arteries and veins on the left and right side respectively. These vessels bifurcate into smaller branches providing blood supply right up to the uterine lining. The uterine arteries divide into the basal then further splitting occurs to produce radial arterioles that supply the small bore spiral arterioles that convey blood to the tissue closest to the uterine wall.

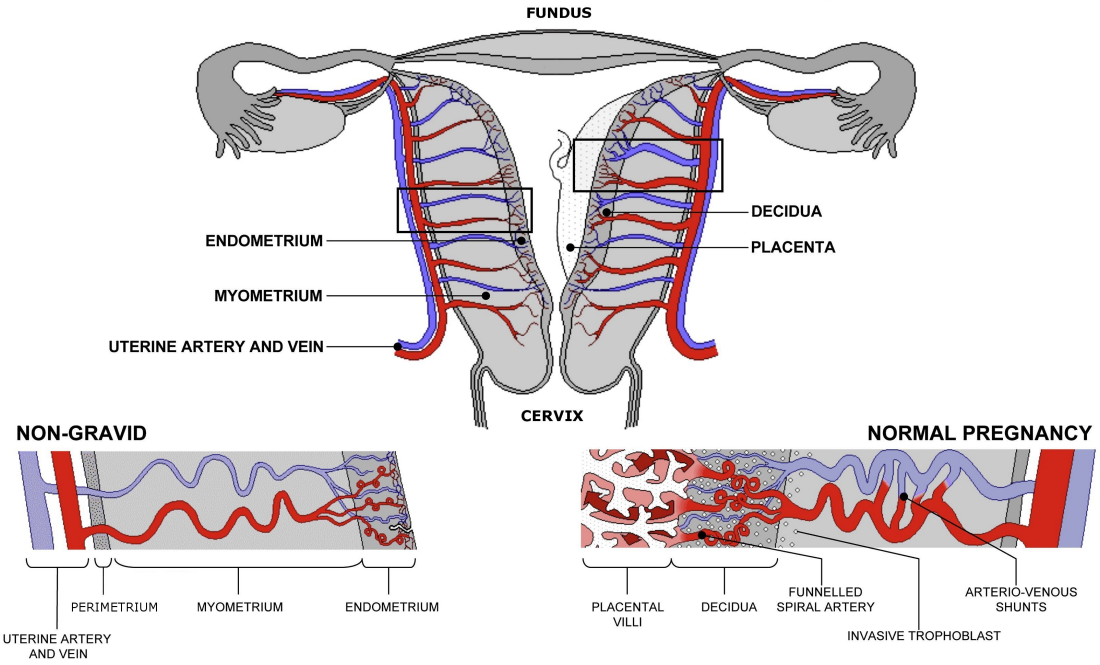

Figure 2.3: Overview of the uterine vasculature and anatomy in normal (left) and gravid/pregnant (right) states. Reproduced with permission from Burton et al. [10].

The spiral arterioles of the uterus have been a keen research interest for decades as they govern the degree of flow between mother and fetus over pregnancy at the point of transfer between maternal vasculature through to placenta. They are described as coiled narrow-bore vessels whose spiral shape effects the dynamics of flow at the

distal end of the uterine circulation[10]. In the non-pregnant uterus, such a vessel would seem to be effective as a dampener of pressure and flow for when the top layer of uterine tissue is "sloughed away" at menstruation. However, such a tortuous conveyor of nutritional supply in a system that needs to dramatically increase its throughput of nutrients to the feto-placental unit can immediately be seen as a potential obstacle to nutritional support.

Cardiovascular adaptation of the mother over pregnancy to meet the requirements of the developing placenta and fetus show in the increase in cardiac output and uterine perfusion. Maternal cardiac output increases by 30-40% over pregnancy[11] with uterine perfusion rising from around 50ml min^{-1} to 1300ml min^{-1} [12]. In animal studies, the sheep is most often used in pregnancy study and has shown uterine blood flow as a proportion of cardiac output rising from 0.5% to around 20% over the course of pregnancy[13]. These results reflect the requirement for the uterine vasculature to adapt itself to accommodate this increase in perfusion, and does so through a unique process of remodelling of the spiral arterioles through a process known as trophoblastic invasion.

2.1.1.1 Trophoblastic Invasion

Research into the mechanisms behind the alteration of blood flow in human pregnancy have been challenging to study due the to potential for any investigation to negatively impact human fetal development. Animal studies, *ex-vivo* models and human histopathological studies in extreme cases such as complete hysterectomy have been the only way to gain further insight into the developmental process.

Despite these challenges, correlation between disturbed placental perfusion and pregnancy outcome has been observed[14]. Histopathological investigations of the 1950s

and 1960s showed that a "physiological change" occurs in the spiral arterioles of the uterus to accommodate the increase in blood flow required to sustain the growing feto-placental unit to term[7,15,16]. This change is caused by trophoblastic invasion where placental trophoblast cells travel through the uterine tissue and via the lumen of the spiral arterioles and alter the anatomy of the maternal vessel walls proximal to the placenta. They convert the smooth muscle walls of the spiral arterioles into flaccid, non-resistive wide bore surfaces to accommodate the need for increased nutritional supply. By abolishment of the muscle wall there is a loss of contractility and vasomotor control irrespective of any maternal attempts to regulate blood distribution within the body, which is important in providing a constant large flow rate to the placenta and fetus over the course of pregnancy.

Figure 2.4 illustrates the remodelling process. This is a highly invasive process and is susceptible to failure. The extent of invasion is not as deep into the uterus as in normal pregnancy This incomplete conversion restricts entrance of blood into the placenta and alters the haemodynamics which has pathological consequences as described in the next section.

2.2 Utero/Placental Pathology

It is a large generalisation to state that depth of invasion is the sole cause of poor vascular remodelling. The underlying biological framework behind successful trophoblastic invasion remains illusive but it is known that a combination of mechanisms are required for successful arteriole remodelling[17]. There is still large debate as to the pattern, rate of change of the vessels and whether this physiological change occurs progressively or

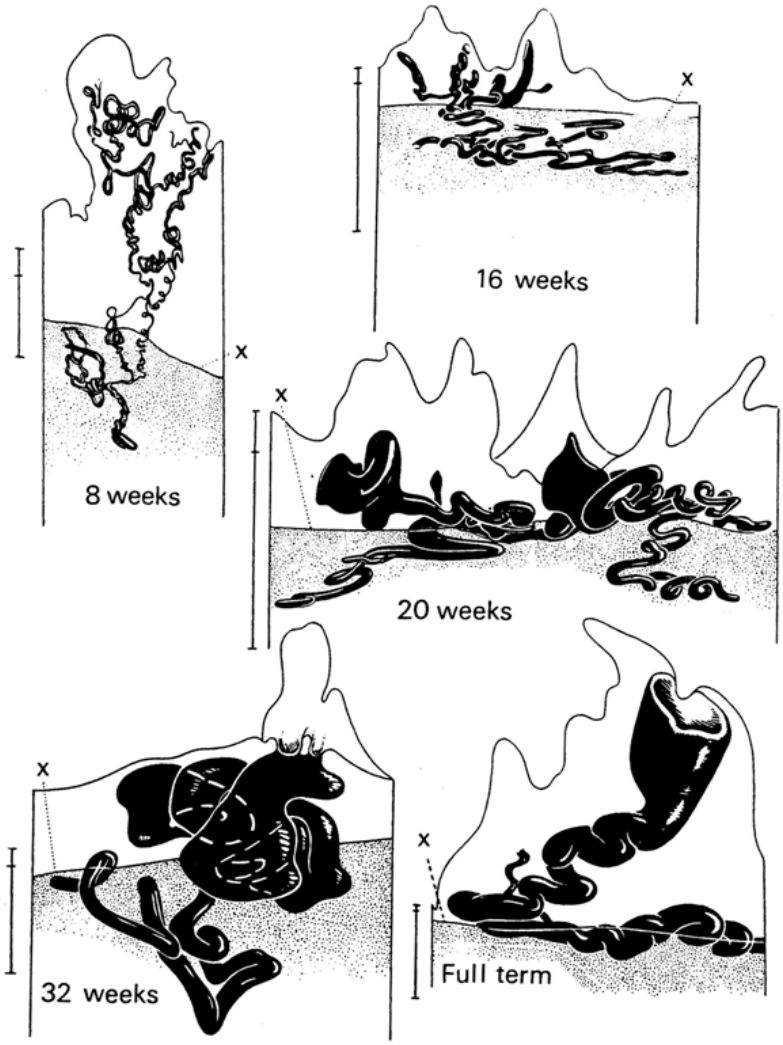

Figure 2.4: Diagrammatic representations of the course and congiruartion of the utero-placental arteries at various stages of pregnancy. The 'x' indicates the myometrial surface and the scale bars show the relative thickness of the endometrium and myometrium. Reproduced by permission of the Carnegie Institute, Washington[7].

in two distinct stages[18–21]. However, to avoid a situation where nutritional demand exceeds supply through the whole of pregnancy remodelling of the spiral arterioles must take place.

In the pathological case, impairment of nutritional support is considered a failure

of the utero-placental unit. This failure is one of the leading aeitologies in obstetrics and is leading cause of fetal growth restriction and pre-eclampsia[16,22]. The seriousness of these pathologies is compounded by the negative effect of these syndromes on the outcome of the fetus long after birth. The review by Godfrey and Barker (the latter being the researcher who originally proposed the theory[3]) on the role of the placenta in "fetal programming" emphasises this point. Fetal programming is the hypothesis that a stimulus or insult at a sensitive point in early life has permanent effects on structure, physiology and metabolism[23]. Many studies have shown significant associations between placental weight and placental weight/birth weight ratio and long term cardiovascular and metabolic outcomes such as high blood pressure, coronary heart disease and increased stroke death rate[24,25]. The serious implications of restricted development *in utero* of the fetus warrants further investigation as well as definition of when a fetus does not reach its inherent growth potential and whether this can be detected during pregnancy.

Understanding of the timing and pattern of blood flow into the placenta has altered since the first researchers made observations on the subject. It was initially assumed that shortly after implantation of the conceptus on the uterine wall circulation of maternal blood into the intervillous space is established[26]. This view has been challenged by the work of Hustin and Schaaps[27,28] who, by using injections of barium sulfate into the arterial circulation of pregnant hysterectomy specimens, showed that during the first trimester the intervillous space of the developing placenta is separated from the uterine circulation by plugs of trophoblastic cells. These cells occlude the distal ends of the spiral arterioles[27] which blocks the entrance of blood into the intervillous space until around the end of the first trimester of life[29]. At this point in pregnancy, these plugs are eroded and the maternal circulation is allowed to enter the intervillous space.

Given the invasive nature of Hustin and Schapp's study, other researchers attempted to replicate their findings using non-invasive techniques such as Doppler ultrasound. By measurement of the flow waveform as an estimate of blood flow, no flow was found inside the intervillous space before 10 weeks gestation[30–32]. This finding has provoked major debate between clinical sonographers[33] and anatomists[34] about the precise status of blood flow within the intervillous space during the first trimester[35].

Although there is controversy about the presence of blood flow in normal pregnancy it is accepted that in complicated pregnancies the placenta appears to be vascularized well before the end of the first trimester[30,36]. In these pregnancies, trophoblastic invasion is severely restricted compared to the normal situation[37]. This has led to the theory that this plugging prevents passage of oxygen-rich blood into the intervillous space. This is believed to occur as in the absence of the plugging, oxygen concentration will fluctuate too rapidly or rise too high and overwhelm the developing cellular antioxidant defences, resulting in oxidative stress[38]. The mechanisms and impact of oxidative stress upon the developing feto-placental unit are beyond the scope of this thesis but the pathology shows the importance of better understanding the underlying dynamics of blood flow entering and circulating within the placenta.

Plugging is determined by the migration and invasion of trophoblastic cells. The action of plugging has been shown to occur most extensively in the central area of the placental bed compared to the periphery[39]. This asymmetrical invasion leads to the theory that the abolishment of the plugs occurs first in the periphery where invasion is weakest and gradually progresses toward the centre of the placental bed where plugging is most extensive[39,40].

2.2.1 Defining Growth Restriction

Fetal growth restriction (FGR), intra-uterine growth restriction (IUGR) and small-for-gestational age (SGA) are terms used in obstetric medicine to distinguish the growth restricted population from the normal. However, each term represents a subtly different cohort of the population and further can be defined differently depending on literature source. For the purposes of this work, it is importantly to clearly define what these terms mean and their context in this study. Growth restriction (FGR or IUGR) implies that there is a pathological issue that impedes the pre-determined genetic growth potential of the fetus whereas SGA is a simple threshold partitioning a set of birth weights that are below a selected threshold for the overall population.

It is important to try to define a metric that can separate the normal but low birth weight baby from the pathologically small one as best as possible. Many birth weight models have been proposed to predict potential growth restriction for small baby with respect to population. The use of a customised antenatal growth chart is attractive as it attempts to predict weight for an individual whilst taking into account maternal characteristics such as previous pregnancies, weight and ethnicity that impact on growth. The best studied individually customised model is produced by Gardosi[41,42] who incorporates the above characteristics into a weight calculation that is then projected backwards, using an ultrasound derived proportionality curve, to predict the expected optimal weight at all gestations[43].

For any clinical work produced as part of this thesis the birth weight model proposed by Gardosi was used to define fetal growth restriction as below the 10^{th} centile in the population. As this definition is not based upon any pathological markers such as Doppler abnormalities any clinical results will refer to SGA instead of FGR and IUGR.

Any babies whose birth-weight was above the 10^{th} centile is defined as appropriate for gestational age (AGA).

The importance of defining these terms is due to growth restriction being one of the most significant causes of perinatal morbidity and mortality in pregnancy in developed and resource-constrained countries. FGR is caused by compromised supply of nutrients and oxygen to the fetus (80–90% of all cases)[44,45] as a result of placental insufficiency, where the placenta is unable to provide the appropriate nutritional support for the growing demands of the fetus over pregnancy. As this insufficiency leads to FGR, it is clear that a better understanding of the causes of insufficiency are required as well as an ability to clinically detect if insufficiency is occurring in a pregnancy. The next section outlines potential methods to detect fetal growth restriction.

2.2.2 The Importance of FGR Detection

Interest in prediction of FGR is high due to the clinical benefits of identifying such pregnancies at an early stage. Screening would provide precise recognition of high-risk pregnancies which would better focus consultant care and reduce serial growth scans as well as provide increased accuracy in detecting pregnancies that lead to stillbirth[43]. Epidemilogical study of occurrence of stillbirth since the early 1990s has shown little decrease in occurrence to the present day. Until recently, as many as 50-70% of stillbirths were categorised as unexplained after postmortem investigation.[46] However, inclusion of FGR as a category in stillbirth classifications drops the rate of unexplained cases to around 15%[47] and has been shown to be the lead risk factor for stillbirth, ahead of smoking and obesity.[48] Most importantly, the risk of stillbirth increases where detection of FGR does not occur. Normal risk of stillbirth approximates

to around four births in a thousand nationally.[47] In a study of 92,000 women in the NHS West Midlands region, the risk rate was reported for all pregnancies as 4.2 per 1000 births (a composite of a rate of 2.4 for non-FGR and 16.7 for those pregnancies with FGR).[48] The rates reported for FGR where detection occurred was 9.7 whereas it increased to 19.8 where detection was not possible. This work shows that compared with normal pregnancy, FGR pregnancies have a fourfold increase in risk compared to normal pregnancies which increases further to eightfold if FGR is not detected. The clinical relevance of this work is that although FGR cannot be fully treated *in-utero* appropriate identification can lead to a well timed delivery in a non-adverse uterine environment (i.e. before failure of the placenta to provide nutritional input for the fetus) and lower risk of adverse pregnancy outcome.

2.2.3 Screening for FGR using Biomarkers

Current methods to screen and identify FGR early in pregancy suffer from poor sensitivity and specificity. The research into screening for FGR is currently based around investigating if certain biomarkers are indicative of raised risk of FGR in pregnancy.

In medicine, a biomarker typically refers to a blood protein whose concentration correlates to a pathology in some way but generally refers to a biologic feature that correlates with disease in some manner[49]. Recently, imaging measures to describe these features have been used effectively to indicate pathology[50].

Using protein markers has proved successful in prediction of Trisomy 21 (Down's Syndrome) and pre-term delivery[51] with success which points to the potential to use these markers as predictors of FGR. Studies investigating whether various biochemical markers may be indicative of FGR pregnancies have been performed that show weak

correlation between biomarker concentration and pregnancy outcome[52,53]. These results lead us to focus upon investigation of new techniques to define image-based markers that can better identify FGR pregnancies from the typical population.

2.2.3.1 The Search for Biomarkers of FGR

Several biochemical markers have been investigated that may be linked to FGR including placental protein 13 (PP13)[54], Disintegrin and metalloproteinase domain-containing protein 12 (ADAM12s)[55] and cystatin C[56]. A large cohort study showed a link between low pregnancy associated plasma protein-A (PAPP-A) and low birth weight[52] with another demonstrating that low PAPP-A at 10 weeks is strongly associated with stillbirth related to placental dysfunction[57]. However, no single biochemical marker has yet proved either sensitive or specific enough to be used as a screening test for fetal growth restriction[43].

Ultrasound based biomarkers for FGR have been proposed using different anatomy and ultrasound modality such as Doppler measurement of the uterine artery[58,59], umbilical artery[60] or ultrasound measurement of biometry such as abdominal circumference[61] or femur volume[62]. These studies found weak correlation between biochemical and ultrasound markers and FGR and as a result are not currently strong enough predictors of restriction. However, when combined into a composite test for FGR, there may be potential for a future screening test akin to the nuchal translucency (NT) scan for identification of Trisomy 21[63]. The NT scan combines serum analyites such as PAPP-A and free beta human chorionic gonadotropin (free β-HCG) and are used in combination with an ultrasound scan to investigate the accumulation of fluid behind the neck of the fetus to test for this chromosomal abnormality. This test provides a rate of detection of 90.2% with a false positive rate of 5%[64].

A recent study has proposed creation of similar models comprised of uterine artery Doppler waveform, nuchal translucency, five biochemical markers and mean arterial pressure to predict SGA outcome at 11-13 weeks[65]. In Karagiannis et al. a detection rate of 46% was identified at 11-13 weeks using this method[65]. Our work explores prediction of FGR using biochemical and other placental-based markers of growth restriction. Building on prior work[63,66] we propose to investigate if any ultrasound-based markers provide an indicator which could augment a predictive model of FGR.

Although it is known that the tissue border between the placenta and the uterus is a site of pathology in pregnancy, it has proved difficult to create fast, useful clinical tests to quantify size or measure change in the anatomy or structure. As a result, surrogate measures such as waveforms of the uterine or umbilical arteries have been proposed as an upstream or downstream marker of the vascular remodelling of the uterine tissue in the placental bed.f

We hypothesize that a focus on the anatomy closest to the pathology will provide imaging biomarkers that could indicate a potential abnormality. Quantification of the placenta is already part of clinical routine at birth with the weighing and examination of the organ in hospital and has been for many years including a qualitative assessment of its health. As placental weight is indicative of fetal outcome[24] at term it seems logically to think that measurement of the placenta *in utero* could provide a strong predictor of FGR as the correlation between placental size and fetal outcome may begin before birth. This research path has only become feasible recently due to the advances in the quality of ultrasound imaging which is discussed in the next section along with an outline of ultrasound physics.

2.3 Ultrasound Imaging

In order to investigate the placenta during early pregnancy we are limited in medical imaging modalities to ultrasound. Due to the detrimental impact on the fetus, no imaging technique that uses ionising radiation (X-ray, computed tomography (CT) scan or positron emission tomography (PET)) can be used. Despite being non-ionising, magnetic resonance imaging (MRI) is not used before 20 weeks in pregnancy due to concerns that tissue heating and acoustic noise may be detrimental to early development[67].

Ultrasound imaging can be used in several different modes: B-mode scans a plane using a linear array of transducers to provide a 2D image of an object whereas Doppler imaging makes use of the Doppler effect to measure and visualise blood flow. Either mode uses a "pulse echo" technique that creates a visualisation based on the mechanical interaction of short pulses of high frequency sound with biological tissue and their returning echoes[68]. Although safe for use in obstetrics, ultrasound images are often of lower quality than other medical images acquired by different modalities. They are very acquisition dependent and so can result in poor signal-to-noise ratio as well as idiomatic characteristics such as shadowing, attenuation and scattering. Despite these drawbacks, obstetricians are adept at learning how to interpret ultrasound images and it is an invaluable tool in fetal medicine.

2.3.1 B-Mode Image Formation

Ultrasound imaging uses sound of a frequency greater than the upper limit of human hearing (20,000Hz) to produce a wave that can penetrate a medium. The reflection produced by the wave's interactions with the medium can then be converted to a tomo-

graphic image that can visualise soft tissue and organs. Use of ultrasound in obstetrics was pioneered by Donald[69] at the University of Glasgow in the 1960s and has been used ever since in diagnostic medicine to observe fetal growth[70] and to investigate the placenta[71].

The transducer that emits the ultrasound waves is composed of a number of piezoelectric elements that each produce a pulse of ultrasound and then convert the mechanical pressure caused by the returning echoes from these pulses into an electrical signal. As the sound propagates away from the transducer and down through the tissue, sound is reflected at the interface between tissues with different acoustic impedances. Some of this reflected sound is the returned echo and based on factors such as the amplitude of the returned signal and time taken for the pulse to be received by the transducer an image of the underlying biological tissue can be produced. Figure 2.5 shows the A-mode signal indicating echo amplitude on the *y*-axis versus time on *x*-axis. The 2D B-mode image that is used for clinical diagnosis is constructed from multiple A-mode signals stored as a linear array where amplitude fluctuations from the A-mode correspond to displayed greyscale intensity. This link between the A-mode and B-mode signals is illustrated in the example presented in Figure 2.5a.

The interactions of ultrasound with matter as the beam is sent from the transducer into the body results in scattering, attenuation, refraction and reflection of the sound impulse. Each of these actions has effects upon on the displayed ultrasound image which need to be considered when attempted in measure anything investigated by an ultrasound scan.

Scattering is one type of reflection, caused by small irregularities in the tissue relative to λ (where λ is the wavelength of the ultrasound wave). In the situation where

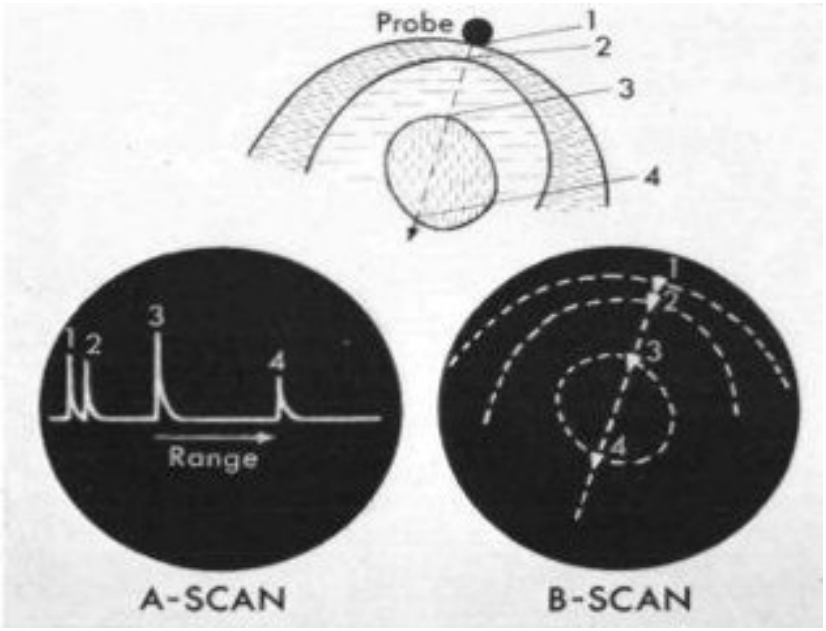

(a)

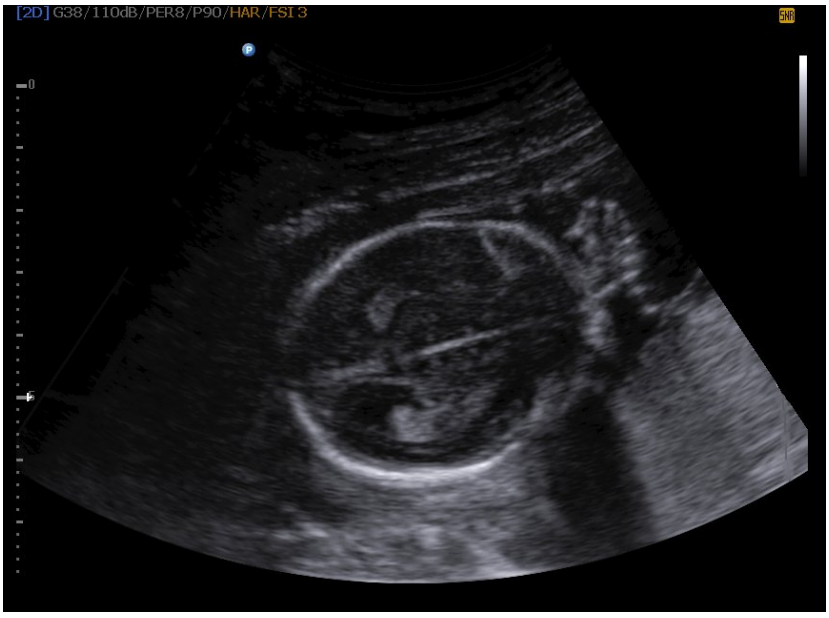

(b)

Figure 2.5: Figure 2.5a illustrates the difference between A-mode and B-mode imaging using a diagrammatic example. A probe is positioned upon a body with three distinct tissue types with different acoustic properties. Reproduced from Donald[70] with permission. Figure 2.5b shows a modern 2D B-mode acquisition of the fetal cranium acquired as part of the Intergrowth 21st Study[72] and shown as a rough *in vivo* representation of the diagrammatic example above.

the objects are small ($\leq \frac{1}{10}$ of λ) they act as a point re-radiator, scattering sound energy in all directions in a spherical field. For objects with size $\approx \lambda$ the radiation of energy is non-uniform and is dependant on the object's size and shape. As the objects get even bigger to the size of a large, flat surface the reflection of energy is identical to specular reflection where the angle of incidence equals the angle of reflection. Where the surface is perpendicular to the beam, this will provide a mirror-like reflection but where the incidence is non-perpendicular energy is reflected away from the transducer.

Scattering of ultrasound in this way impacts on image appearance, as boundaries between tissues and objects are best seen when they are perpendicular to the beam. Figure 2.5b shows an ultrasound image of the fetal head that presents the boundary of the cranium clearly where the head is perpendicular to the transducer but fades at the periphery of the skull. As a result of these characteristics, images are typically acquired with this in mind. A special case of scattering is speckle which is caused by constructive and destructive interference of ultrasound by minute stochastically placed scatterers in tissue. This scattering is the reason behind the granular appearance of ultrasound images[73].

Attenuation is a final factor in the appearance of the images based on interactions between ultrasound and the medium. Attenuation of the beam is caused by energy loss through reflection or absorption (as heat). As a result, the intensity of the ultrasound beam decreases exponentially with distance.

All the factors listed above contribute to the appearance of ultrasound images and the artefactual noise that affects the ability for one to discern an anatomical object from an ultrasound view. In particular, the positioning of the placenta, maternal BMI and time in gestation at which the image is acquired. These factors are discussed in greater depth in chapter 5. Despite these obstacles to providing high quality images,

it is important to note that technological advancements have increased the acquisition quality and resolution of images. Figure 2.5b shows a transverse slice of the fetal brain taken from the Intergrowth 21^{st} study[72]. It exemplifies the increase in tissue detail shown in the appearance of the ventricles and white matter of the developing brain as well the dense lateral and axial image resolution. This advancement is due to improved transducer design as well as advancements such as the use of harmonic imaging to increase contrast to noise ratio (CNR) and reduce image artefacts[74]. Where contrast is defined as the difference in intensity to percieve different objects in the same field of view

This section outlines the underlying physics that contribute to the appearance of an ultrasound image. In the case of ultrasound imaging of the placenta, there are specific artefacts and challenges in the interpretation of the these images. These are described in greater detail in section 3.2 but are based upon the interactions of the ultrasound with the surrounding anatomical features.

Despite these challenges, with the enhancement of ultrasound image quality, both B-mode and other ultrasound modalities provide increasingly more robust acquisitions. As a result, we believe that the ability to combine the latest Doppler techniques to identify the underlying changes to the arterioles in the uterus over the course of pregnancy is both possible and may provide further markers for FGR.

2.3.2 3D Ultrasound

Three dimensional ultrasound imaging has flourished in the last two decades, providing volumetric imaging of organs and pathologies in faster time and with higher fidelity than ever before. Using conventional 2D US imaging, quantification and visualisation

of an organ's complete anatomy is hindered and requires a user to mentally integrate multiple 2D images to form an impression of the overall volume. This is further compounded where an organ (such as the placenta) is irregular in shape and structure. The adoption of 3D ultrasound as a clinical tool has been mired as unlike CT and MRI, the interactive, dynamic nature of ultrasound image formation requires that 3D ultrasound imaging can provide volumetric images in real-time. Until recently, clinically useful 3D US systems were limited due to the cost to provide such a scanning machine that had the appropriate computational speed. With the increasing ubiquity of 3D imaging, there is a growing clinical interest in investigating if volumetric metrics add diagnostic power over currently used 2D measures or biomarkers.

A variety of methods exist to produce 3D US volumes but are typically defined by the dimensionality of the transducer used. Our study uses 3D data acquired using a linear array transducer using a mechanical tilt method to acquire the 3D images. For further detail on freehand and 2D scanning, the reader is recommended to refer to Fenster et al.'s recent review on 3D ultrasound[75]. Illustrations of the different types of 3D US acquisition are shown in Figure 2.6.

This review also outlines three requirements for 3D volume acquisition: rapid acquisition of images to avoid alteration by respiratory or fetal movement, continuous knowledge of probe orientation and location to nullify any geometric distortion and that probe apparatus is simple to use so as to be easily appended to any clinical consultation as well as allowing consistent anatomical placement when acquiring images.

In obstetrics, the usage of "tilt" mechanical ultrasound scanners is becoming more commonplace and volumes from these machines are the subject of this body of work. Ultrasound data acquired in a 3D ultrasound scan was stored in a proprietary, vendor

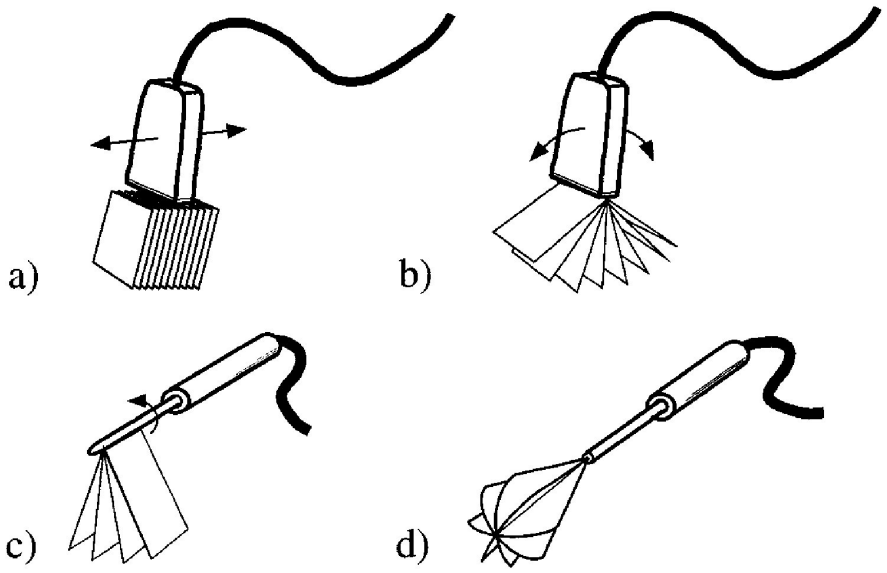

Figure 2.6: Schematic diagrams showing four different mechanical approaches to 3D ultrasound acquisition - (a) Linear scanning approach, in which a series of parallel 2D images are acquired (b) Tilt scanning approach (c) Tilt scanning approach used with a side-firing TRUS transducer (d) Rotational scanning approach. Taken from Fenster et al.[76]

specific format. This is based upon the non-parallel acquisition (mathematically represented in a pyramidal or polar co-ordinate system) of ultrasound data at each point of interest in the field of view. Based on the geometry of the scan-lines produced from the transducer and acquisition settings the volume would be transformed into a Cartesian coordinate system for visual display, archiving or analysis.

Data conversion is required to provide the 3D ultrasound scans in the form of a Cartesian volume for image analysis which although not part of this research was a technical development required to produce aspects of the work that follows so is outlined briefly. The original format represents each voxel of data based on its distance r and angle θ to a point of origin (the transducer head) for each 2D slice of data. In most modern abdominal transducers, the probe is then swept using a motor over a set swing angle, collecting a set of 2D sweeps as it is swings. The truncated cone

of 3D ultrasound data is then transformed into a cuboidal volume for visual display using one of many methods that exist for the transformation of the scanline representation (θ,r) of the data into a Cartesian (x,y,z) system.[77,78] The image quality and time to convert from polar to Cartesian is dependent on interpolation technique (trilinear, nearest-neighbour or, spline-based)[79] and hardware architecture.[80]

The image acquisition and conversion to a different geometric system will result in an anisotropic volume due to the non-parallel acquisition of the different scanlines. As the scanlines travel deeper into the tissues so the distance between data points increases, as the scanlines diverge away from each other. This results in fine resolution between data points close to the scan head which then degrades as the distance from the acquired point to the transducer head increases. This anisotropy is an important consideration when converting images from those saved by the US system to a Cartesian format that is then able to used for image analysis. By trilinear interpolation, isotropic volumes can be constructed from the original polar acquisition, however this is not as representative of the original acquisition which is anisotropic. To provide an image volume as close to the original acquisition, we reconstruct the volume in a Cartesian setting using a resolution that is coarser in axial direction. This has the added advantage of reducing the voxel count of a given organ and so the computational burden of any image analysis over the whole volume.

Our conversion process was tested comparing ultrasound scans of phantoms such as ping-pong balls and other shapes whose volume was measured by manual segmentation of ultrasound images and also determined by displacement in water. With concurrency found between both these volume measurements we considered the conversion to provide accurate representation of any object scanned using the scanning equipment used to obtain images analysed throughout this thesis.

3D ultrasound offers full observation of an organ *in-vivo* which allows any potential area of pathology within that organ to equally be recorded. To analyse an organ from the 3D acquisition it must be extracted from the ultrasound data. This is performed by image segmentation which is introduced in the following section.

2.3.3 Doppler Ultrasound Imaging

Doppler ultrasound imaging uses the phenomena of a shift in frequency of an ultrasound wave caused by the passing of a moving reflector in the beam's path to estimate blood flow. In an *in vivo* biological system this is typically a red blood cell or soft tissue depending on the clinical application. By using this technique, ultrasound and can retrieve some information of the the blood and soft tissue movement in the body.

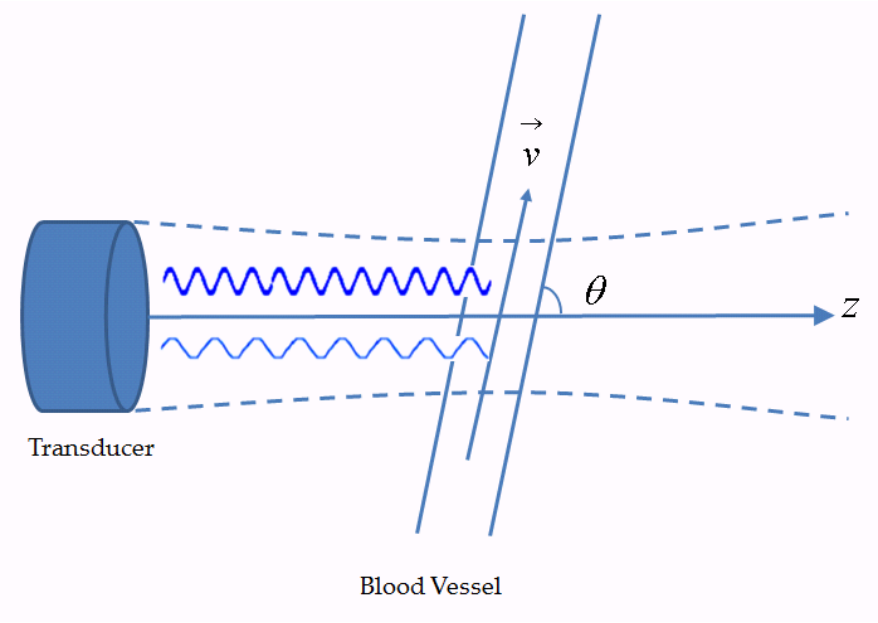

Figure 2.7: A simple continuous wave Doppler ultrasound system. Ultrasound wave travels in z direction and is returned with frequency shift corresponding to the angle of the beam with respect to the object, θ and its velocity, $\vec{v}$.

Continuous wave Doppler systems as shown in Figure 2.7 were the first to be introduced in the field and used a simple transducer with two distinct areas to transmit the ultrasound wave and then separately to receive the backscattered signal from blood. The backscattered signal exhibits a frequency shift proportional to the velocity relative to the direction of the beam[81]. This shift is determined by the Equation 2.1 where Doppler shift (f_d) is determined by

$$f_d = \frac{2v f_o \cos\theta}{c} \tag{2.1}$$

where v is speed of the scattering particle, f_o is the transmitted ultrasound frequency, c the speed of sound in the medium and θ the angle between the particle's velocity vector and the beam direction.

continuous wave (CW) Doppler ultrasound although simple to calculate suffers from depth selectivity and struggles when multiple vessels are overlaid upon each other[68]. This has led to the introduction of pulsed wave (PW) systems that uses bursts of sinusoidal waves in distinct pulses to provide range discrimination[82]. The pulse repetition frequency (PRF) is the frequency at which these bursts are transmitted and is used in the calculation as the Doppler shift is calculated from multiple returned pulses over time.

As the emitted pulses have a finite duration unlike CW systems, the pulse has a finite bandwidth and as such each of the frequencies in the bandwidth can have its own Doppler shift. Therefore PW can be considered a "Doppler" measure that is linked to a degree by the velocity of moving scatterers but tissue attenuation and Rayleigh scattering also have an impact upon the shift of the centre frequency of a given pulse[83].

As a result, the shift of the centre frequency would provide an inaccurate estimate of blood flow and so other estimation strategies are required. These are broadly defined as narrow and wideband estimation techniques of which the most widely used is the auto-correlator method of Kasai et al.[84]; other methods are outlined in Jensen[85] and Goldberg[86].

2.3.3.1 Colour Flow Imaging

Modern ultrasound systems provide the ability to use an array of transducers and also produce a steerable beam. The operations described for a single ultrasound beam can be performed for a number of lines to yield a 2D map of blood flow. This CFI map of axial blood velocity is overlaid upon the B-mode structural image to provide the anatomical detail that relates to the observed blood flow. Interleaving of the pulses for the different ultrasound modalities is required to provide real-time measurement. Quality of CFI acquisition has improved due to improved signal processing methods and increased computational performance in the processing of the backscattered signal returned to the transducer and reconstructed to a image. In real time (around 30 frames per second) 128 azimuthal lines from the transducer are used to produce the 2D image which each require 4-18 firings per line[86] to produce the signal to estimate Doppler shift. This shows the challenge of a modern US system to scan a large number of azimuthal lines whilst providing a sufficient number of frames per second.

2.3.3.2 Colour and Power Doppler

Figure 2.8a shows the estimation of blood velocity by colour Doppler and the concentration of vascularity provided by power Doppler (PD). Both methods are based

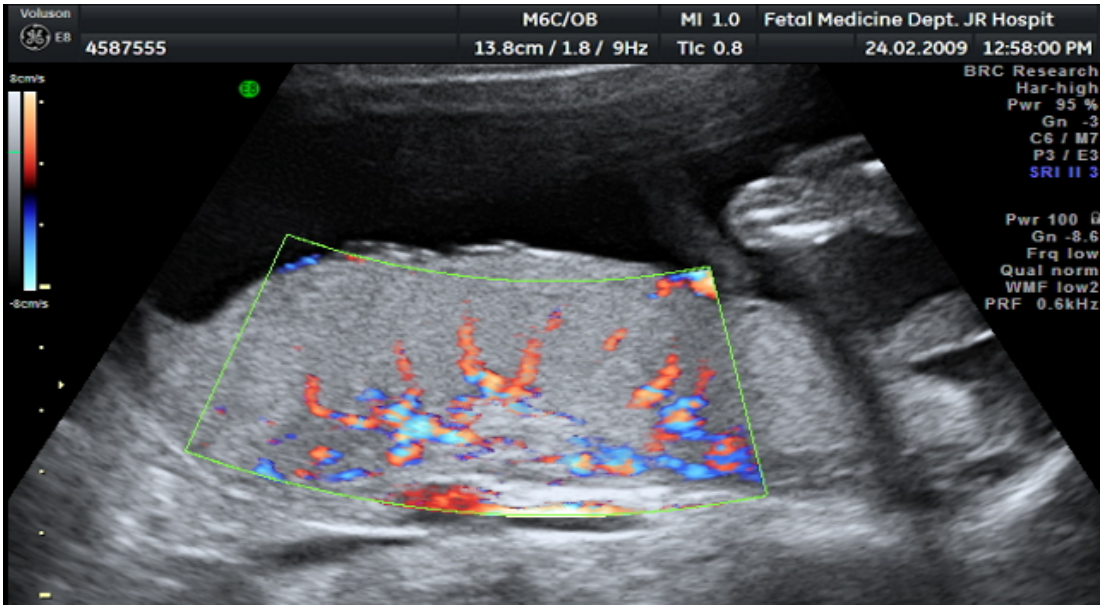

(a)

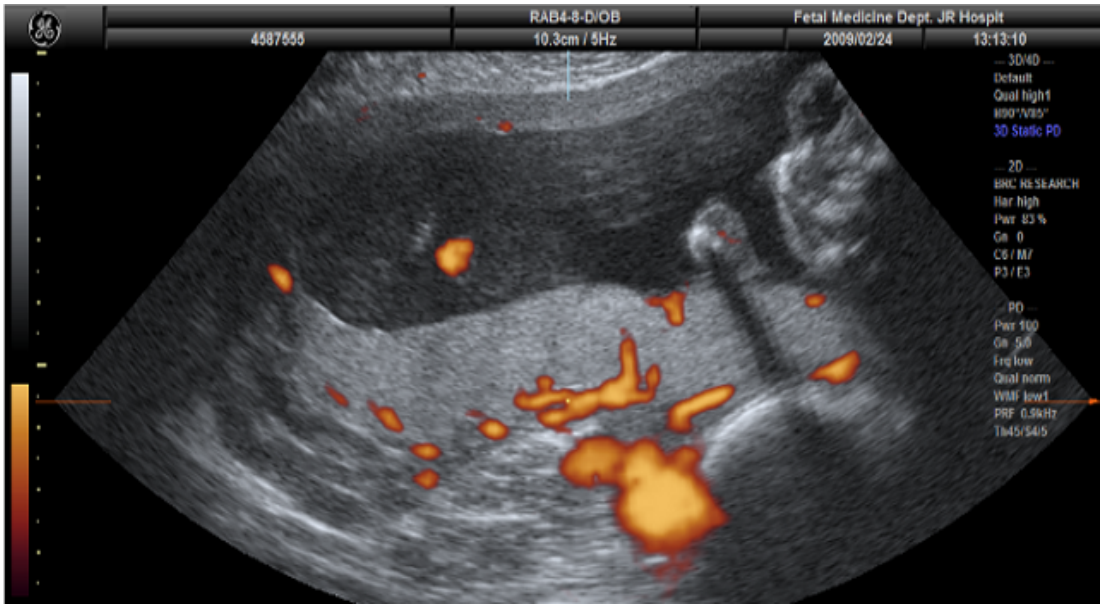

(b)

Figure 2.8: CFI and PD images of the vasculature of the placenta taken from a patient as part of the Spiral 3D study.

upon the Doppler spectrum produced as described previously but provide different representations of the underlying estimated blood flow. Power or energy Doppler is calculated from the integral of the Doppler spectrum. As a result of this integration, it is indicative of the concentration of moving scatters rather than the mean of the spectrum as, displayed by colour Doppler[81]. Colour Doppler is advantageous in producing a map of the directionality and magnitude of flow, whereas power Doppler can only indicate presence of flow.

Colour Doppler has a number of methodological problems that make consistent and accurate estimation of blood flow difficult. As a frequency detection technique, aliasing artefacts are an issue where the frequency is above half the sampling frequency (based upon the pulse repetition frequency). Noise is also a problem as it has a random distribution with time and as a result can impact on the mean Doppler shift. Most importantly, and especially in a case where CFI may be used in 3D, is the angle dependency of the method. Equation 2.1 shows that due to the $\cos\theta$ term any flow perpendicular to the beam is not estimated and in tortuous vessels such as the spiral arterioles, this is clearly problematic.

In considering measurement of the vascularity of the basal plate of the placenta colour Doppler must be excluded because of the reasons above, this leaves only power Doppler as a potential methodology to study the complete basal plate in 3D. Due to PD using the integral of the Doppler spectrum the method is more sensitive to low moving blood flow with an increase in sensitivity of 10-15dB relative to colour Doppler imaging[87]. PD values are far less dependent on the angle at which the vessels are insonated with respect to the ultrasound beam so increased detection of vascularity a lower velocities is created. Received power remains the same from any direction a Doppler shift is detected, in reality there is a slight angle dependency since very small

shifts will be removed by noise filters at the signal processing level. However, there are drawbacks to using PD; the loss of measurement of blood velocity has already been discussed. Motion sensitivity is also greatly increased so minimal fetal, maternal or transducer movement is required to avoid "flash" artefact.

The final reason behind choice to use power over colour Doppler is the sizeable body of research that has investigated the standardisation of PD measurement. Outside of a singular examination using 3D PD, any measurements of PD values are meaningless due to the impact of machine settings and the variation of the subject (maternal habitus, fetal depth, intervening tissue type) impacting upon the backscattered signal[88]. In the application of PD upon the placenta, these influences need to considered and compensated for before any attempts at estimation of flow can be performed.

2.3.3.3 Estimation of Blood Flow Using Power Doppler Ultrasound

The clinical desire to develop methods to better understand and measure the placenta and surrounding vasculature has resulted in a large number of clinical publications using various techniques to measure blood flow within the placenta. These methods have used many different Doppler modalities such as continuous wave, pulse wave and colour flow imaging for vascular quantification.

A group of papers have used the Doppler waveform of the spiral arteriole on the basis that flow at the distal end of the arteriole should be unidirectional. In practice however, this has led to ambiguity as unidirectional flow could be detected due to noise or overlay of multiple arterioles and as such is not a perfect indicator of the location of the spiral arteriole which has led to conflicting results[92–97]. Another technique developed by clinical collaborators at the John Radcliffe Hospital, Oxford used 2D

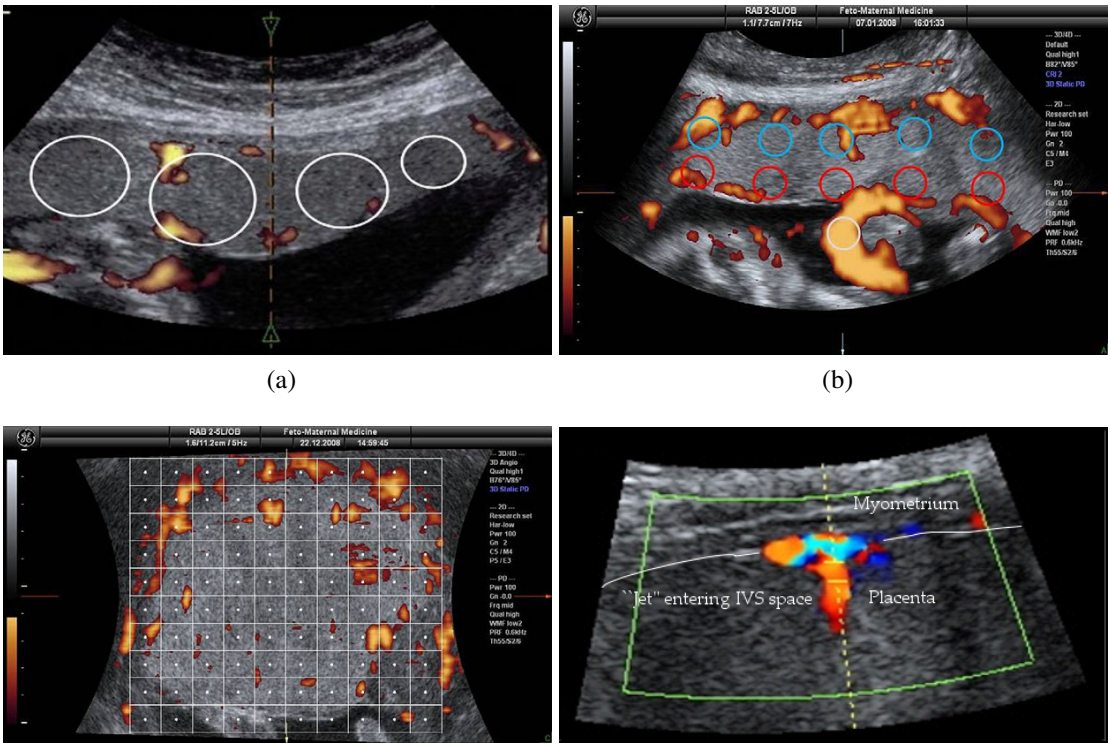

Figure 2.9: Illustration of different techniques for measurement of blood flow in the placenta. Clockwise from top-left - sphere biopsy method of Noguchi et al.[89], a method using 2D colour Doppler upon the blood entering the placenta from a single spiral artery[90]

and an extension of previous technique investigating fetal and maternal sides of the placenta[91] and finally a similiar technique using spheres sampled on a discrete grid[91].

CFI of maternal blood flow as it enters the intervillous space. These spiral arteriole "jets" of blood flow provide an indicator of flow entering the placenta but require training and large amounts of time (20 minutes plus per scan) to acquire such precise images[90]. This work does show that the underlying information from the jets from CFI can be extracted and correlates with the underlying anatomy, this shows promise that there is a rationale for using this form of imaging to make inferences about the maternal vascular anatomy.

With the ubiquity of 3D Doppler acquisition other researchers in the field have moved away from 2D measurement as described and have begun measurement of the Doppler information found in the entire placental volume. Typical examples of the current clinical output in the field is illustrated in Figure 2.9a. Figures 2.9a and 2.9b show the use of spheres to encapsulate a volume of interest or "virtual biopsy" as described in the papers[89,91]. This method although interesting in terms of its desire to add additional information to the underlying blood flow introduces a number of additional aspects of variability in its attempt to sample the placental blood flow. Placement and position of the sphere within the volume is decided by the observer which adds another layer of variability - the repeatability of which has been investigated with conflicting results[98–100]. To remove this ambiguity, efforts have now moved to sampling the placenta as a whole or using spheres on different aspects of the placenta volume to measure the blood flow on the fetal and maternal sides of the placenta. This is an attempt to reduce the observer error and variability of the underlying anatomy that may boost the overall robustness of any PD measurement technique.

Currently no technique in press has shown any degree of automation in terms of its selection of a VOI. The measurement methods to use once a VOI has been found also vary and are fully described in Chapter 5. The issue of attempting to standardise measurement between patients and between scans longitudinally is discussed along with the other factors that affect power Doppler values and the attempts by our work to minimise their influence upon our results. A framework to identify and measure the pathological area of the placenta involved in poor trophoblastic invasion is introduced. This framework aims to show if measurement of PD signal at the anatomically interesting area of the placenta boosts any prediction of the SGA fetus and aims to reduce the variances introduced by acquisition and measurement techniques that have led to

conflicting results in previous works.

2.4 Image Segmentation

Image segmentation is the process of partitioning an image into a number of foreground objects that are distinct from the background. More precisely, this can be considered a process whereby each pixel in an image is labelled such that pixels with the same label share certain characteristics. Segmentation is used in a variety of applications found in computer vision and medical image analysis such as face detection[101], iris recognition[102], traffic control[103], organ detection and measurement and computer guided surgery[104].

Image segmentation can be considered a manual, semi-automatic or fully automated process. This reflects the amount of automation used in production of the segmentation. Computer based medical segmentation is an attractive for a number of reasons compared to manual segmentation. Manual segmentations are typically performed by outlining and highlighting the objects of interest in the image by a clinical observer. In the 3D case, this requires multiple outlines that can take more than 30 minutes per dataset depending on size of volume and complexity of structure. Given the long time required to perform this repetitive procedure, automation is an attractive strategy to increase the speed of placental volume calculation. There are two types of automated segmentation - semi or fully automatic. Semi-automation involves a manual initialisation step for an algorithm that then performs further processing to generate the final segmentation whereas automatic segmentation requires no user initialisation.

There are a number of techniques used in the field of image segmentation. Typically, many segmentation techniques are originally developed from natural image seg-

mentation before being applied to the medical image domain. Fast naïve techniques such as region growing and thresholding are used in simple situations, with more complex techniques used for challenging segmentation problems. As processing power has increased, the ability to use much more computationally intense algorithms that provide much more robust segmentation results is now possible as well.

Segmentation methods can be grouped in many different ways depending on the strategy they use to solve the problem. Edge-based, region-based, deformable, graph or statistical models, and machine-learning methods can all be used to perform segmentation. A broad choice is clearly on offer as to which strategy to use however the choice of imaging modality and characteristics of the organ of interest have impact on the method.

A large number of methods can be described as performing an energy-minimisation of a type of energy function. The majority of members of the set of segmentation algorithms producer their output in this way with slight differences in strategy. A number of methods optimise a functional defined upon a continuous contour or surface. These include snakes[105], active contours[106], region competition[107] and level sets[108]. A separate group uses an energy function but typically on over a finite set of variables. This set is typically a collection of nodes that correspond to pixel values, the graph formed from these nodes would therefore be the region of interest. Examples of this include graph cuts[109,110], random walker[111], fuzzy connectedness[112] and methods to compute best paths in 2D such as intelligent scissors[113] and live-wire[114].

We propose the use of a relatively new graph based method, random walker to segment the placenta in 3D. It requires a manual initialisation step and so is semi automated. This is in line with other multi-planar techniques currently clinically used in research. A broader background review is described in the following chapter in sec-

tion 2.5. This method was implemented and validated as a first part of this thesis from which other research avenues were explored. A key problem in using 3D volumetric scans is the ability to view anatomical surfaces and areas deep within the volume quickly without manual intervention. Based upon the segmentations produced by Random Walker we propose a new visualisation method for viewing these areas. A background of the brief review of medical 3D visualisation is outlined in the next section.

2.5 3D Visualisation of Ultrasound Images

To maximise the understanding of a 3D ultrasound scan, many different visualisation methods have developed to allow a user to manipulate and view the image interactively. In particular MPR and volume rendering have been used to provide greater insight into the volume data displayed.

Volume rendering is a frequently used technique to view anatomy in CT and MRI to visualise highly contrasting areas of tissue. Using a "camera" as a point to view the 3D dataset, multiple 2D lines (rays) are cast through the 3D dataset to produce a 2D projection of the data[116,117] based upon the interaction between the ray and the underlying scalar data. Figure 2.10a illustrates volumetric rendering. In ultrasound, soft tissue contrast is poor but rendering has been used with good effect in visualising the fetal skeleton and the features of the fetal face where contrast between the amniotic fluid and bone is high. Clinically this has been useful in measurement of face abnormalities such as cleft palate[118]. For more information on the different techniques to produce volumetric projections they are recommended to read Meißner's et al's review[119].

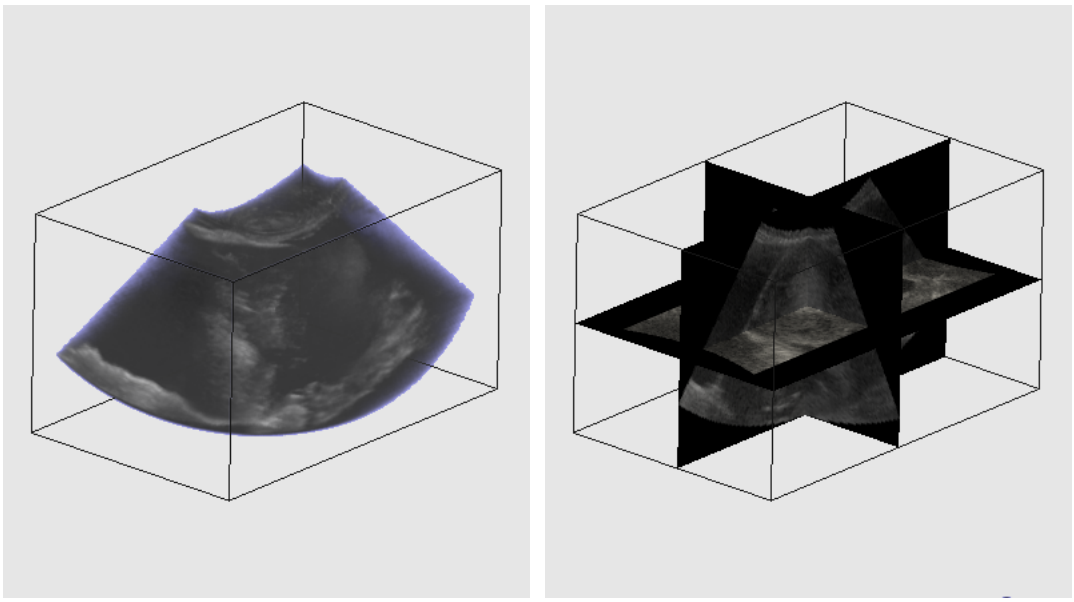

(a) (b)

Figure 2.10: Ray casting (left) and MPR (right) visualisations of a 3D ultrasound volume. Figure created using ParaView 3.8 (Kitware Inc, Clifton Park, NY, USA) [115].

In contrast to volumetric rendering, MPR uses slices of data extracted from the complete volume to allow comprehension of the 3D geometry (Figure 2.10b). These planes typically intersect each other and can be moved and manipulated by the user to reveal anatomy or a location of interest. Either method requires the manual selection and manipulation of a volume to create a suitable visualisation that shows the region of interest within the acquisition. This can be time-consuming and when performed on many different datasets becomes quickly redundant as anything that could be used to aid the understanding of the imaging data.

These techniques are used for many different modalities other than ultrasound however there are applications that have been developed that provide specific methods for 3D ultrasound. There exist a number of bespoke ultrasound imaging viewers produced by ultrasound system manufacturers such as 4D View and QLab produced by General

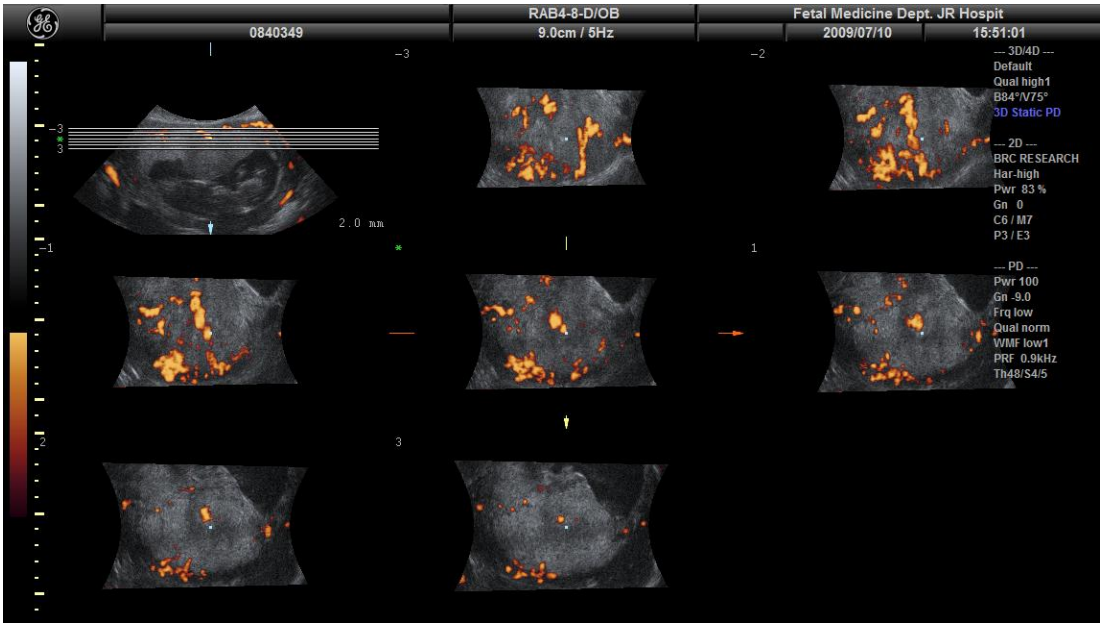

(a)

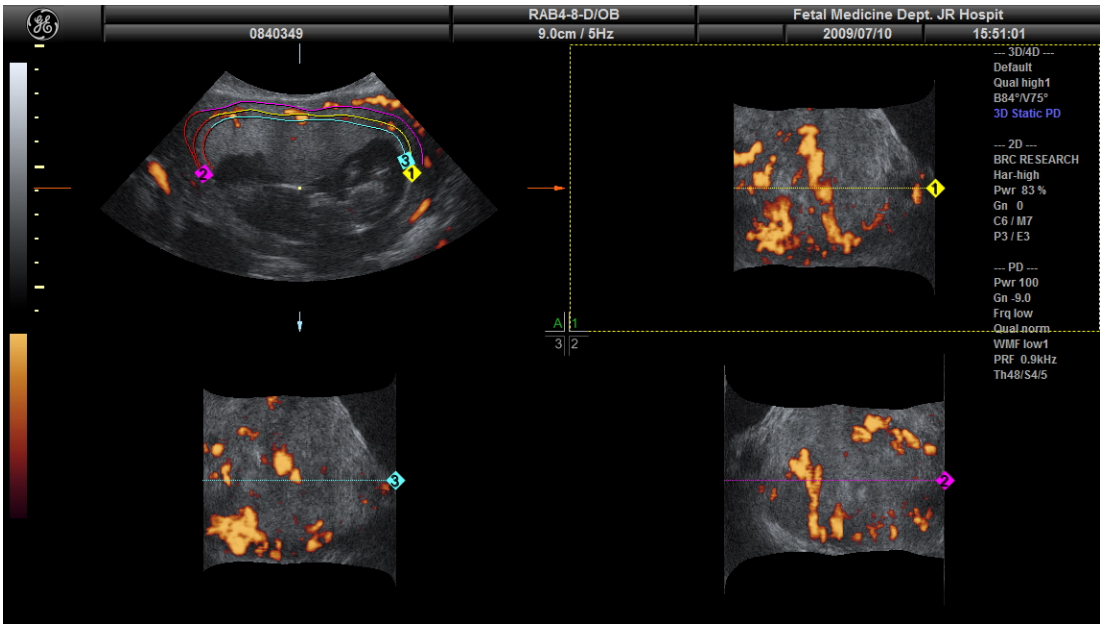

(b)

Figure 2.11: Visualisation of the basal plate of a placenta using imaging tools provide by 4D View®. Top - TUI. Bottom - "OmniView".

Electric and Phillips Healthcare respectively. These applications provide commercial methods to manipulate the 3D volumes produced by the companies respective ultrasound machines to provide greater flexibility in viewing these volumes. Examples of two particular methods using 4D View are shown in Figure 2.11. The first method is TUI which allows the sequential analysis of slices that are a user determined number and spacing apart. Figure 2.11a shows TUI applied to the basal plate of the placenta, and the resulting slices relative to the site of pathology in FGR pregnancies. It shows slices of data relative to the initial defined plane at distinct millimetre intervals relative to the starting plane. This provides a number of advantages over the traditional methods previously described. It provides the use of planes that are typically not possible using conventional ultrasound and the ability to view multiple planes in a single view without having to re-render or adjust any viewer settings. A different style of visualisation method is shown in Figure 2.11b. "OmniView" allows a user to define up to 3 lines, curves, poly-lines or freehand tracings from which projections of 3D surfaces relative to these initialisations can be viewed. The freehand nature of the initialisation allows more flexibility than the starting point of TUI imaging and so for curved tissue interfaces or anatomical parts that are irregular it is more suited than the rigid reconstruction allowed by the TUI method. Unlike TUI, only three different views using this method can be shown for any volume and the projection produced is limited to a perpendicular direction from the initialised curve.

These methods show the field moving toward more custom and bespoke methods of visualisation to overcome the limitations of viewing specific areas in a 3D dataset. The methods described are produced as part of a specific toolkit and so are only available to be used with General Electric (GE) ultrasound data and additional features are only available if the user has the appropriate version of the software which

requires purchase. Despite some research groups investigating the additional value of these tools[120,121], the whole obstetric ultrasound research community is unable to use them unless they have the appropriate data produced by the specific manufacturer's system. These measures also lack a degree of accessibility as scalar values can only be measured using the inbuilt histogram or vascular indices (these are outlined in Chapter 5) available in 4D View or by recovering the scalar data by screenshot of the viewer. The clinician is limited to qualitative diagnostic measurement based on purely image appearance.

Any of these techniques will generate an initial visualisation but will require manipulate to present particular views of interest. We propose in Chapter 4 a technique that can automatically visualise the 3D interface between placenta and uterus and provide the user with greater understanding of the shape of the plate without requiring manual adjustment of the initial object. It moves away from the field of using orthogonal planes to represent aspects of the volume, but rather the geometry from a segmentation.

2.6 Conclusion

This chapter has introduced many different ideas from varying areas of medical and imaging science to show the potential for 3D ultrasound to measure potential growth restriction in pregnancy. Using a 3D ultrasound system, placental volume *in utero* can be measured using fast, accurate image segmentation techniques that can quantify the placental volume which may be a factor in growth restriction. By using new visualisation methods as well as Doppler ultrasound the potential for quantifying the site of the pathology of pregnancy in many cases, the utero-placental interface, can be realised.

Chapter 3

3D Ultrasound Segmentation of the Placenta

PLACENTAL weight and size at birth has long been considered an indicator of fetal outcome. Large studies have shown a significant relationship between fetal outcome and a small placenta at term[2]. As a result, this correlation raises the question of whether measurement of the volume of the placenta *in utero* could be an indicator of fetal health or a predictor of pregnancy outcome. Many studies have reported correlation between placental volume and pregnancy outcome with respectable levels of specificity and sensitivity[122–125]. Volumetric measurement of the placenta to aid in the prediction of pregnancy outcome has not become part of clinical practice for a number of reasons. For instance, most previous studies have used multiple 2D scans to attempt to reconstruct the overall 3D volume. The quality of the reconstruction is based upon the choice of planes (volume sampling) which can lead to errors when choosing consistently repeatable planes in a large population. Additionally, the extra time required to measure organ volume in 3D compared to existing

2D biometric measurements as well as the sparseness of ultrasound machines capable of multi-planar reconstruction or 3D scanning has in the past limited the adoption of such a measure as a serious diagnostic tool. The time-consuming nature of volume calculation is a problem that through automation could eliminate the tediousness delineation of the placenta from the surrounding tissue as well as providing consistent measurement than possible by manual segmentation.

This chapter presents an original implementation of a new method of placenta volume segmentation based on an existing image segmentation technique, random walker (RW)[111]. Section 3.2 outlines the limited prior art in using ultrasound to measure placental volume and introduces methods currently used to perform this calculation. Section 3.3 presents our original approach to solving the problem and results quantifying the performance of the algorithm relative to manual delineation and another existing method are presented in section 3.4. Finally, the algorithm is used in a study of placental volumes acquired at the John Radcliffe Hospital, Oxford (part of the Spiral 3D study) the results of which are presented in Section 3.5.

3.1 Ultrasound Segmentation

The extensive literature survey by Noble and Boukerroui[73] reviews the approaches that have been investigated for ultrasound segmentation. Typically, aspects of the image can be used to garner information about the location of the object relative to the image. Popular characteristics are grey-level distribution, intensity derivatives, feature asymmetry and image texture[126]. Segmentation techniques used in other imaging modalities such as CT, PET and MRI have difficulty mapping over to ultrasound as it is a modality with it's own unique characteristics. Low signal-to-noise and contrast-

to-noise ratios typically led to a failure in "ported" segmentation methods as these rely on consistent and strong features that represent the boundary between an object and background. As a result, methods tend to be adapted to incorporate some from of prior knowledge of shape, motion or appearance in order to overcome the poor image quality. Another way to incorporate prior knowledge is by using a machine learning based approach such as AdaBoost, Probabilistic Boosting Trees or Random Forests which is currently being applied to different ultrasound applications [127–129] or a probabilistic approach such as Fuzzy Connectivity that considers the affinity between pixel neighbours as variable due to noise generated by the imaging device [129]. This has been applied with success in the segmentation and measurement of the subcutaneous fat of the fetal arm or leg *in utero* [130]. Finally, in the event that a fast or interactive segmentation is required with difficult prior conditions a semi-automated method that requires some form of manual initialisation may be required. This can either be considered as a single initialisation point or multiple points to illustrate the difference between the object and background. All these methods have been shown to provide ultrasound based segmentation, the question left to the researcher is choosing an adequate method that best fits the application. Placental segmentation and previous methods to segment and estimate organ size are introduced in the next section.

3.2 Placental Ultrasound Segmentation

In segmenting the placenta, there are clear challenges in accurately defining the organ in a 3D ultrasound sweep. A first step is insuring that the placenta is completely acquired in a single volumetric acquisition. In our work, all 3D data is acquired as part of a study (the Spiral 3D study) which recruited 143 women and scanned them

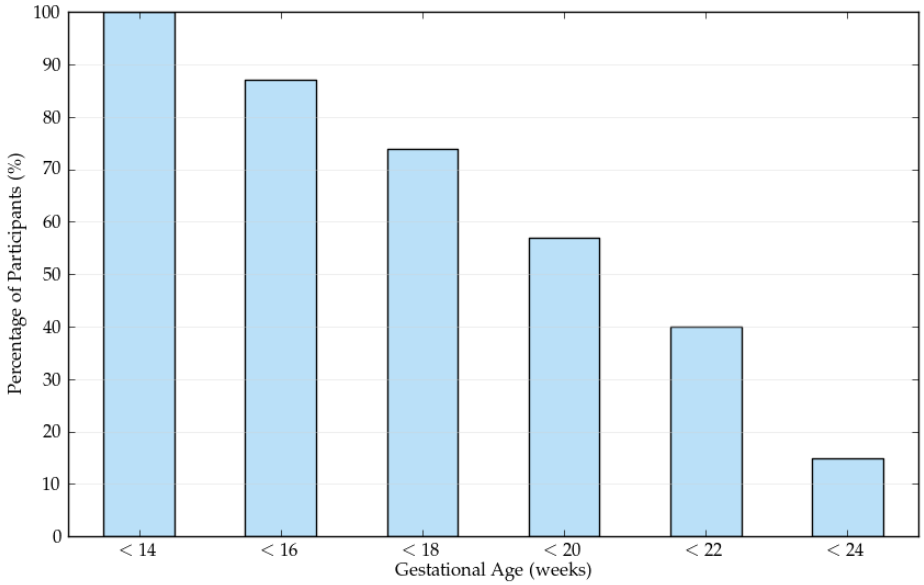

Figure 3.1: Percentage of participants in whom the whole placenta could be captured in a single volume with advancing gestation. Data taken from Spiral 3D Study[43].

biweekly throughout early pregnancy[43]. At scan-time an indication of whether or not the placenta was fully in the field of view was recorded. Figure 3.1 shows that in the study population the full volume for the whole population was completely acquired at up to 14 weeks of gestation. The percentage of study participants for which the whole placenta could be acquired decreased as GA increased. As a result, the focus of segmentation was moved to early pregnancy as defined as 11 weeks to 13+6 weeks as the largest cohort of subjects could be used. This is true where only a single 3D volume sweep is used to capture the placenta in the field of view. It should be noted that by image registration[131] or image fusion[132] multiple sweeps could be merged into a single volume that captures a complete placenta that would otherwise be outside the field of view of a single acquisition.

Placental position is determined by which wall (anterior, lateral or posterior) of the uterus the conceptus attaches itself. Based upon the site of implantation there are challenges upon the appearance of the placenta relative to the probe. When the placenta is posteriorly located with respect to the transducer, attenuation is increased due to the increased distance away from the transducer. Fetal position relative to the ultrasound beam may also lead to drop-out and shadowing that can distort the typical appearance of the placenta (figs. 3.2d, 3.2e) compared to an anterior implantation. Regardless of position, the outer edges of the placenta tend to lose definition, leaving ambiguity as to where the basal plate finishes (fig. 3.2c). In early pregnancy there is a lack of differentiation between uterine tissue and placenta which makes determination of the placenta boundary challenging (fig. 3.2a) as only weak edges delineate the anatomical boundary. Finally, hypoechoic placental lakes can be present in the placenta and lead to a heterogeneous appearance of the placental tissue (fig. 3.2b). It is important to consider these problems when formulating an image segmentation strategy that can accommodate these issues. An excellent pictorial review of these problems using ultrasound and other imaging modalities is presented by Elsayes et al.[133].

$$V = \sum_{j=2}^{n} \frac{1}{2}(A_j + A_{j-1}).(d_j - d_{j-1}) \tag{3.1}$$

Some clinical groups have estimated the volume of the placenta manually or by using semi-automated image analysis tools. Hafner et al.[134] were the first to estimate placental volume using 3D US, using a multi-planar method at early pregnancy (11-13 weeks). This method required an observer to outline multiple slices through the 3D volume at set intervals through the volume sweep and then using Equation 3.1

calculated the whole volume by interpolation from n samples. These parallel sections that were measured were approximately 1cm apart[134,135] where A_j is the area and $d_j - d_{j-1}$ the distance.

Multi-planar techniques use manually traced outlines of the placenta at regular intervals and interpolation is performed to produce a volume by summation of the areas of slices taking into consideration the distances between these slices as shown in Equation 3.1. The accuracy of the volume result is determined by a number of factors, including the accuracy of the tracing, the distance between the areas and the variability of the placenta between these areas. This method is simple to implement but has drawbacks at the periphery of the placenta where shape can become highly irregular. Whether multi-planar interpolation can accommodate this rapid change in shape is an unresolved question. Computation of volume with labelling of each pixel's identity to the background or placenta can be used to provide computation by summation of the number of pixels multiplied by the product of voxel dimensions. In this way and which is performed following segmentation using our method, issues with the method previously described are avoided.

A recent advance on the previous technique is the use of the Virtual Organ Computer-aided AnaLysis (VOCAL^{TM} , GE Healthcare, Milwaukee, WI, USA) imaging tool packaged as a part of the 4D View^{TM} (version 9.1, GE Kretz, Zipf, Austria) image viewer for GE Voluson$^{®}$ultrasound volumes. It performs 3D volume estimation based on interpolation of a number of contours that are generated by rotation around a central point of interest for an arbitrary number of rotation steps defined by angle around the rotational pole (typically 6°, 9°, 15° or 30°). Figure 3.3 shows a placental volume calculated using the VOCAL^{TM} system. The contours can be traced manually or by

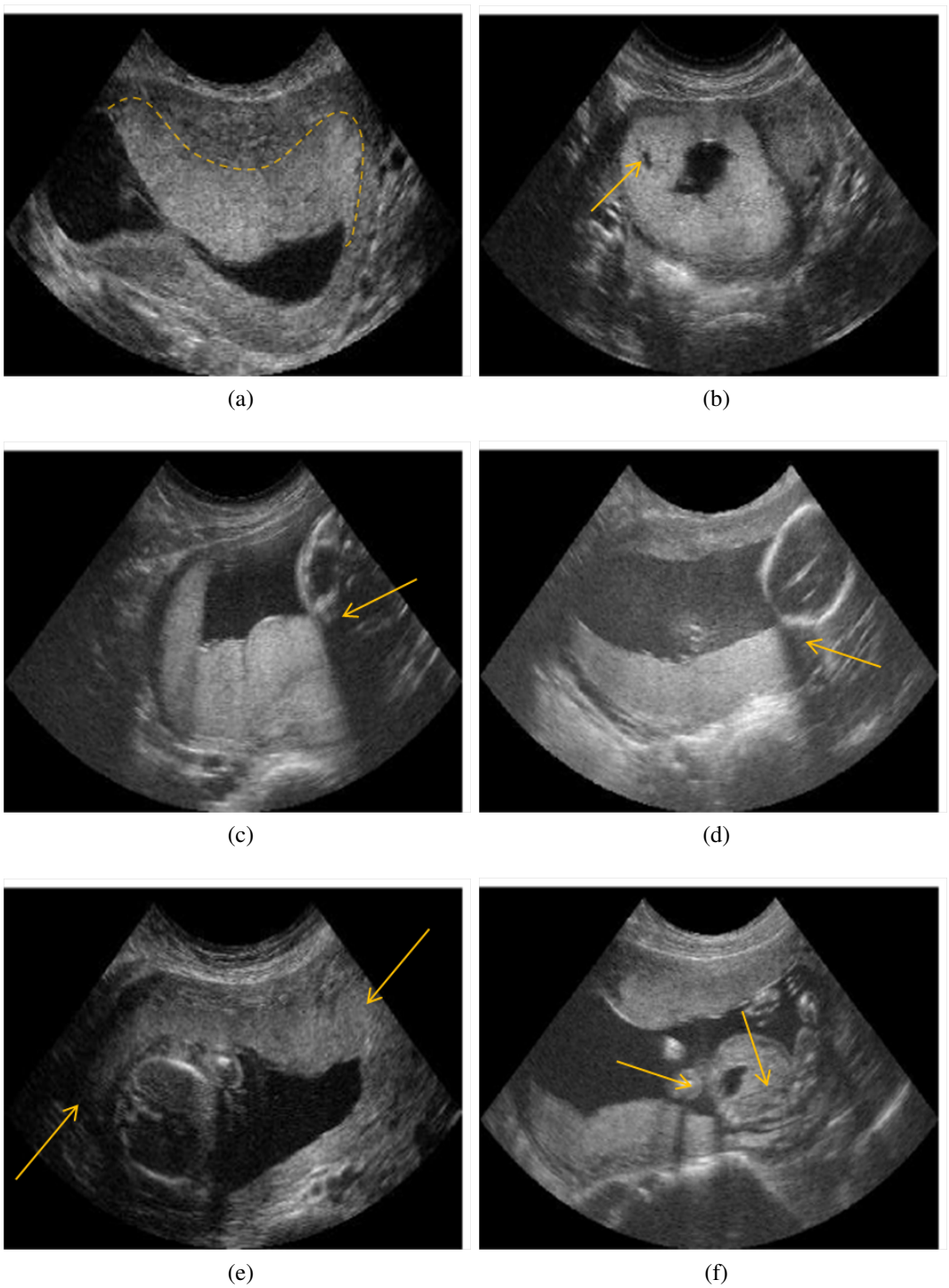

(a) (b)

(c) (d)

(e) (f)

Figure 3.2: Slices of 3D volumes acquired to highlight challenges of identifying the placenta in 3D ultrasound scan. Figures show different issues to overcome : Figure 3.2a – identification of different uterine tissue layers. Figure 3.2b – utero-placental lakes. Figures 3.2c and 3.2d – shadowing. Figure 3.2e – outer borders attentuated. Figure 3.2f – fetal parts.

using a semi-automated active contour method. From *in vitro* validation experiments, there is conflicting reports on what number of rotation steps gives the most repeatable results[136–138]. Two studies have shown a greater number of angular intervals (15°) provide greater repeatability than a 30° setting[136,138]. In contrast to one study at very early pregnancy (7-10 week gestation) showed concordance between 15° and 30° settings[137]. Two clinical data reproducibility studies and studies on phantom models have shown that the VOCAL^{TM} system at the 15° setting is concordant with the multi-planar methodology[138,139].

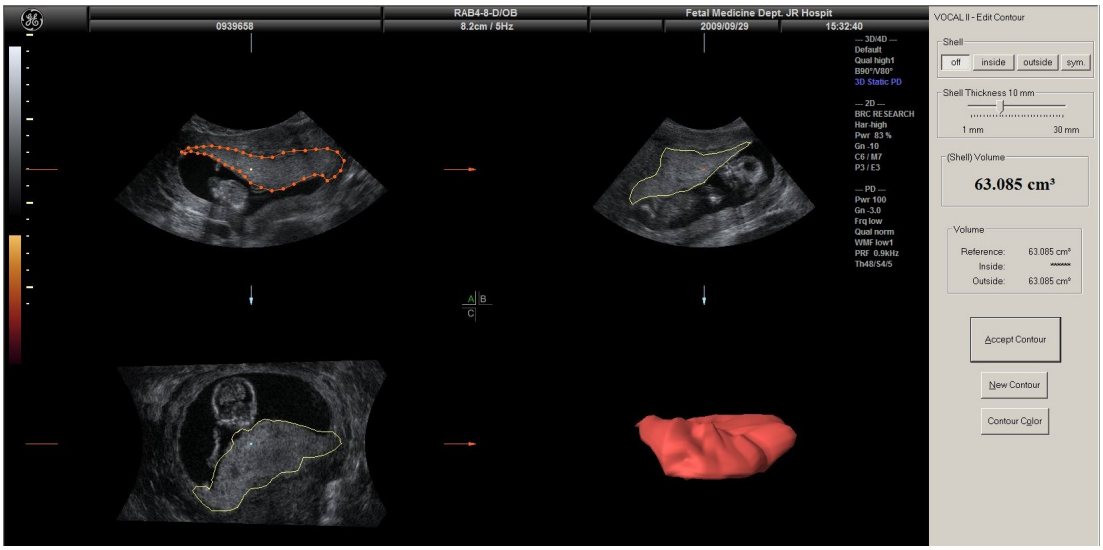

Figure 3.3: Example of VOCAL^{TM} segmentation of the placenta (30° rotation, manual contours). The top left image shows the one of the initial contours and the other two planes illustrate the volume created from interpolation around the rotational point seen in each plane. A 3D mesh to illustrate the segmentation independent of the image is seen in the bottom right window.

In most volume validation studies, VOCAL^{TM} has been shown to be concordant to multi-planar volume calculation but the volume estimate produced is only displayed to the user and cannot be exported as a binary volume which is crucial in allowing voxel-wise comparison of results. As a result, we are forced by the commercial option to

compare only the total volumetric result statistically rather than comparing differences in binary volumes produced by different segmentation techniques. The latter option would provide a far greater understanding into how to optimise these computerised methods to reduce measurement error.

Despite the drawbacks of these methods, a number of studies have correlated 3D volumes of placentas to pathology such as abnormal uterine artery Doppler, pre-eclampsia, chromosomal abnormality, biochemical markers and small-for-gestational age (SGA) outcome[135,140–144]. In particular, a recent study of 600 patients looking at a variety of biochemical and imaging markers (PAPP-A, β-hCG and uterine artery Doppler) found that placental volume was the only independent marker for SGA[63]. There are limitations to the techniques used by previous groups which leads to the potential to implement an algorithm that can overcome the shortcomings of these methods. We propose the use of a graph-based segmentation technique, random walker (RW), to provide fast 3D ultrasound segmentation that can then be used to measure placental volume. The next section reviews the background of the method as well as how it is applied in the case of 3D US images of the placenta.

3.3 Random Walker

The Random Walker algorithm can be described by a user labelling of a number of pixels (e.g for example a particular object or as background). Then for the remaining unlabelled pixels the probability that each pixel belongs to each respective user labelled region is calculated by the likelihood that from many random walkers sent from this pixel we would traverse to a pixel belonging to a particular label. This is computed analytically by solving a system of linear equations where for each region

we compute the probability that from that particular pixel, a random walk would reach a seed labelled for that particular region.

An illustration of a 2D Random Walker segmentation on a 5 by 5 grid is given in Figure 3.4. The algorithm is initialised with three seeds indicating three different regions at pixels L_1, L_2, L_3. Random walks and electrical circuits have similar properties so the performance of the algorithm can be explained using an analogy to circuits. Consider as in Figures 3.4a,3.4b,3.4c that the seeds are set to a voltage source equal to unity and the remaining unlabelled nodes are grounded. Each figure shows the respective probabilities for each region that a random walker would reach that particular seed. Note that the probabilities when added up for each unlabelled node over the figures is equal to unity. The connections between nodes in this case are equal in terms of resistance but can be adjusted based on any features. By taking the maximum probability at each node, a segmentation can be developed as shown in Fig. 3.4d.

For a 3D segmentation the image volume is converted into a weighted, undirected graph $G = (V, E)$ based upon the underlying volume geometry where each voxel is converted to a node/vertex $v \in V$ which are linked together by a edges $E \in E \subseteq V \times V$. Neighbouring vertices/nodes are connected by a set number of edges (e.g. 4, 6 or 16 neighbour connectivity) which are weighted by a weight function. The weight of each edge e_{ij} is denoted as $w(e_{ij})$ or w_{ij}. The degree of a vertex is $d_i = \sum w(e_{ij})$ for all edges e_{ij} incident on v_i. Weighting is based upon a Gaussian function defined as

$$w_{i,j} = \exp \beta (g_i - g_j)^2 \tag{3.2}$$

where g_i is a image intensity at pixel i. β represents the only free parameter set in

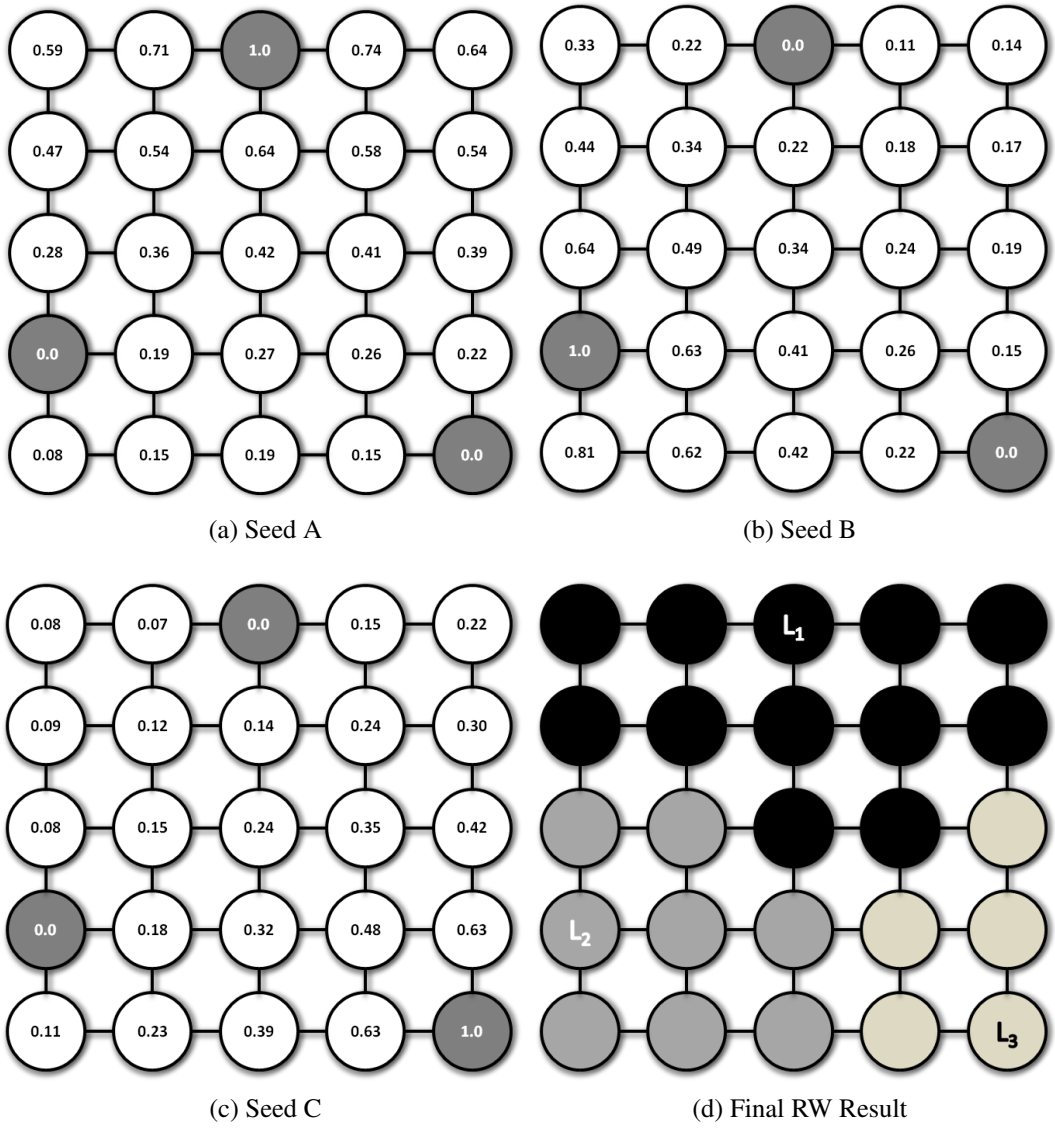

(a) Seed A (b) Seed B

(c) Seed C (d) Final RW Result

Figure 3.4: RWsegmentation on a 5x5 lattice where each node is representative of a pixel. Figures 3.4a,3.4b,3.4c shows for each labelled node that is representative of a class they are set to unity with all others to zero. Note the summation of the probabilities in each node is always equal to one. Figure 3.4d shows a segmentation based upon which label yielded the highest probability.

the algorithm. It should be noted that there is a small positive constant added to all weights to avoid negative weighting as suggested in the original paper[111].The application of weighting to the graph is crucial to the ability of the algorithm to cope with the imaging challenges of ultrasound and the specific issues of imaging the placenta. By weighting the edges of the graph by intensity gradient drive the segmentation to avoid stochastic movement in areas of intensity heterogeneity in preference to more homogeneous pixels.

3.3.1 Formulation

Given a weighted graph and a set of marked nodes V_M and a set of unmarked nodes V_U such that $V_M \cup V_U = V$ and $V_M \cap V_U = \emptyset$ we wish to label those unlabelled nodes based upon the likely labelled node a random walker sent from that particular unlabelled node would reach. From previous work in this domain of mathematics, it has been shown that this problem is equivalent to solving the combinatorial Dirichlet problem[145].

The Dirichlet integral is defined as:

$$D[u] = \frac{1}{2}\int_{\Omega} |\nabla u|^2 \, d\Omega \tag{3.3}$$

for a field u over region Ω. The Dirichlet problem of is to find a function u which satisfies the Laplace equation $\nabla^2 u = 0$. In order to solve for u, we define the combinatorial Laplacian matrix as where L_{ij} is indexed by vertices v_i and v_j.

$$L_{ij} = \begin{cases} d_{v_i} & \text{if } i = j\ , \\ -w_{ij} & \text{if } v_i \text{ and } v_j \text{ are adjacent nodes,} \\ 0 & \text{otherwise.} \end{cases} \tag{3.4}$$

L is then ordered so the labelled nodes are first and the unlabelled second. This partitioning is represented as marked nodes L_M, unmarked nodes L_U and B representing the matrix whose rows correspond to unmarked nodes and columns to marked nodes, respectively.

$$L = \begin{bmatrix} L_M & B \\ B^T & L_U \end{bmatrix} \tag{3.5}$$

The probability at each node v_i for each label, s, is equated to x_i^s. A vector m^s, of size $|V_M|$, where a set of labels seed points are defined as a function $Q(v_j) = s, \forall v_j \in V_M$ where $s \in \mathscr{Z}, 0 < s \leq K$.

$$m_j^s = \begin{cases} 1 & \text{if } Q(v_j) = s, \\ 0 & \text{if } Q(v_j) \neq s \end{cases} \tag{3.6}$$

For a label s, the solution to the combinatorial Dirichlet problem may be solved by Equation 3.7.

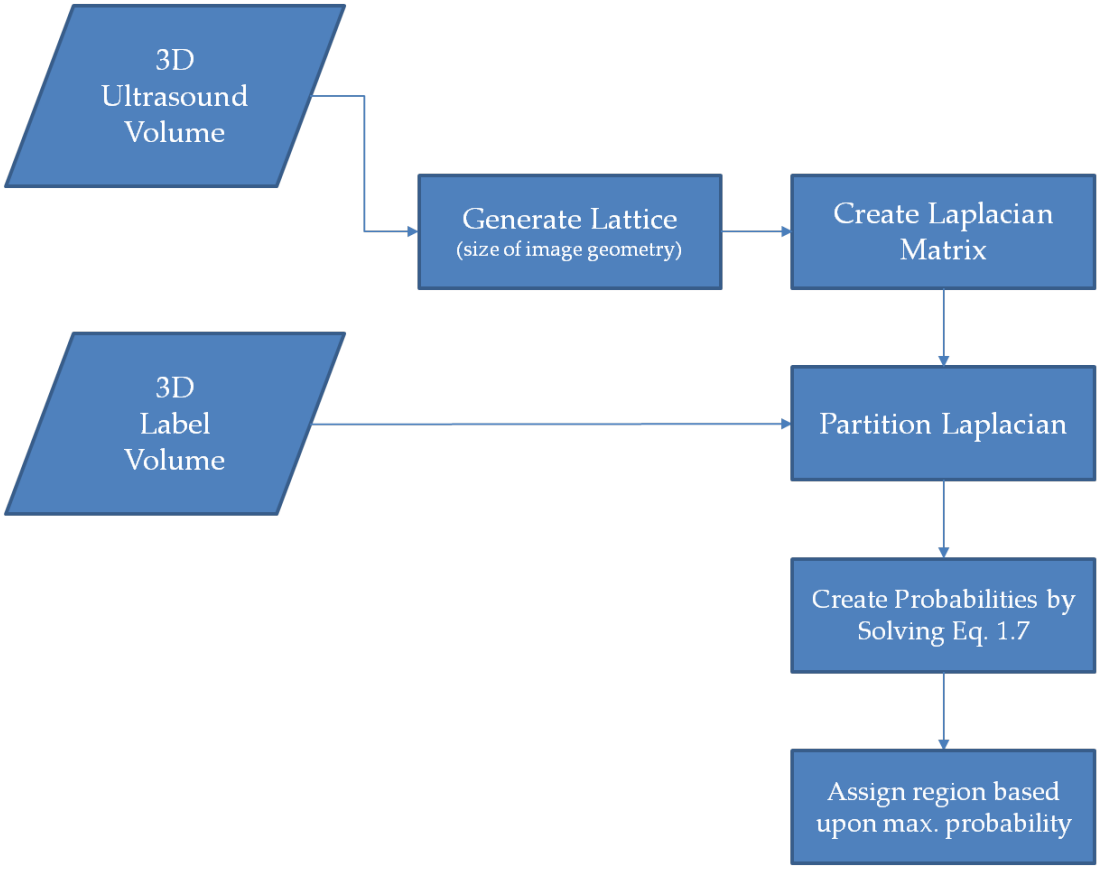

Figure 3.5: Flowchart of implementation of RW algorithm.

$$L_U x_U = -B^T x_M \Leftrightarrow L_U X = -B^T M \tag{3.7}$$

As the probabilities at any node will sum to unity, only $K-1$ linear systems need to be solved, where X has K columns taken by each x^s and M has columns given by each m^s.

A conventional random walker (RW) implementation requires a user labelling in order to provide a segmentation. In our case, this was performed using the segment-

ation protocol outlined in Appendix A. The protocol defines the placement of seeds throughout the volume at set intervals starting from where the placenta arises at one end to where it finishes to the other. Specifically, the initial 3-5 2D slices in the volume where the placenta first arises are labelled. From this point, every tenth slice after this initialisation is labelled until the end of the placenta is reached at which point the final 3-5 slices are labelled. The initialisation is saved to disk as a 3D volume with the same geometric attributes as the original B-mode volume but with the voxel intensities replaced with labels.

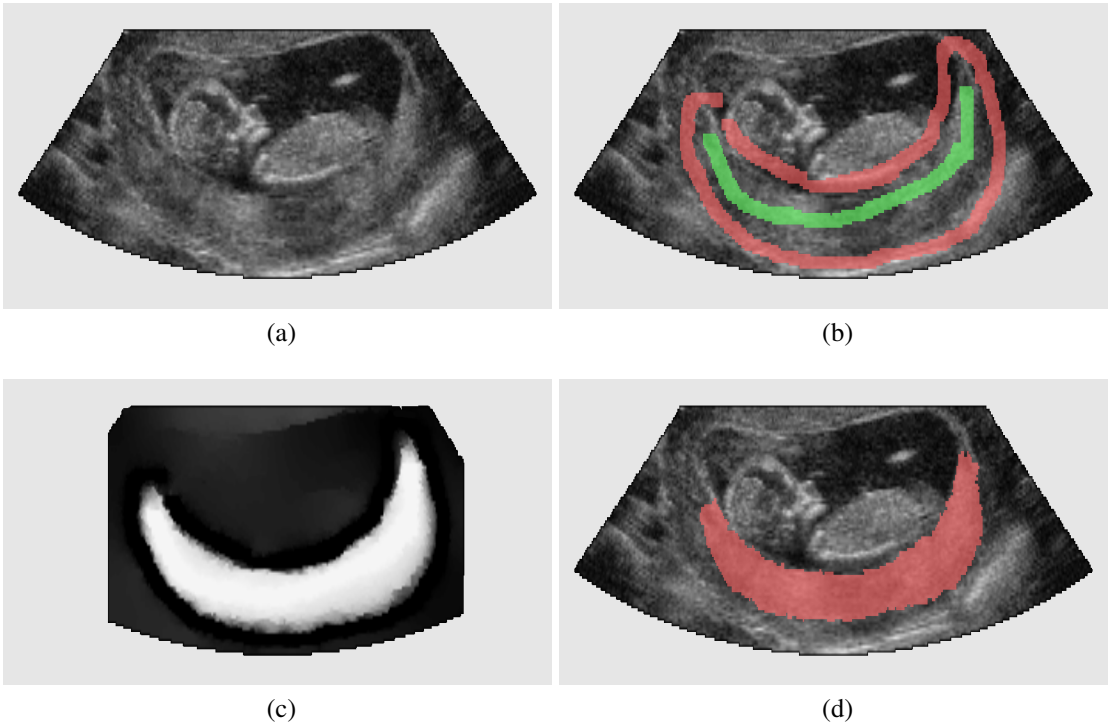

(a) (b)

(c) (d)

Figure 3.6: Illustration of RW segmentation on placental ultrasound. Figure 3.6a shows a B-mode ultrasound slice. Figure 3.6b shows the labelling/seeding where red = background and green = foreground labels. Figure 3.6c shows the probabilities mapped from zero (black) to one (white). Figure 3.6d shows a segmentation produced by segmenting those pixels with a probability of $>= 0.5$

The 3D volume containing the image as well as the user seeding is loaded to

memory and the algorithm implemented as explained in the formulation section. A flowchart in Fig. 3.5 shows how the underlying information from the image and label volume are used in the construction and manipulation of the matrices required to produce the linear system required to produce the probabilities and so the segmentation. Figure 3.6 shows 2D slices illustrating the labelling, probabilities and segmentation.

3.3.2 Implementation

We initially looked at an example MATLAB® (Vers. R2010a, Mathworks®, Natick, MA) implementation provided by the algorithm's author and available online[146]. However, in order to produce 3D segmentations the implementation provided in MATLAB® quickly becomes not fit for purpose due to the reliance upon the direct least-squares solver. The largest image that the implementation can segment was around 1000 pixel square which was insufficient for our needs unless the segmentation was to be performed slice by slice. By taking a sample ($n = 65$) of 3D volumes from the Spiral 3D study the average dimensions of a 3D placental volume approximated $290 \times 187 \times 85$ voxels so the linear system would be equal to around 4.6×10^6 equations!

The original paper notes these numerical practicalities when applying the algorithm in 3D and suggests the use of an iterative linear solver rather than a direct one. Thus an alternate solution was obtained by reimplementation of the RW algorithm in C++ using the open-source insight toolkit (ITK) (Kitware Inc, Clifton Park, NY.) and the visual numeric library (VNL)[147] toolkit for creation of the linear system required to solve Equation 3.7. The implementation was compiled using the 64-bit Microsoft® Visual Studio® 2008 Compiler.

From profiling of the segmentation process, the solution to Equation 3.7 is the main

computational step in the segmentation algorithm. As $|V_U|$ is equal to the number of unmarked nodes any reduction in the number of these nodes will reduce the size of the linear system and thus increase computational performance. The simplest method to perform this is to either increase the number of marked nodes or decrease the overall size of the volume.

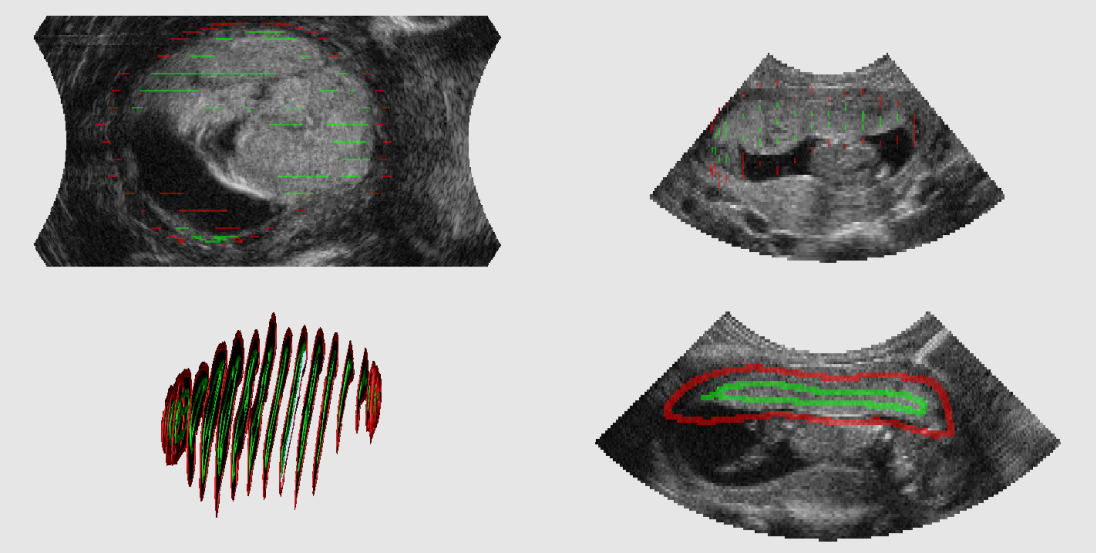

Figure 3.7: Initial Labelling/Seeding of Volume for RW segmentation. Multi-planar display shown in x(top-right), y (bottom-right) and z (top-left) axes. 3D volumetric rendering of seeding labels (bottom right)

As discussed later in the chapter, the segmentation is performed by a consistent initialisation defined by a segmentation protocol (Appendix A). Based upon this the labelling will always generate, in the case of the placenta, initialisation where the area of the placenta will lie within the bounds of any nodes marked as background. Therefore, nodes outside of the boundary of the background seeding can be discarded, and a sub-volume of interest around the initialisation can be considered rather than the volume as a whole. This cropping method provides a simple method to decrease the

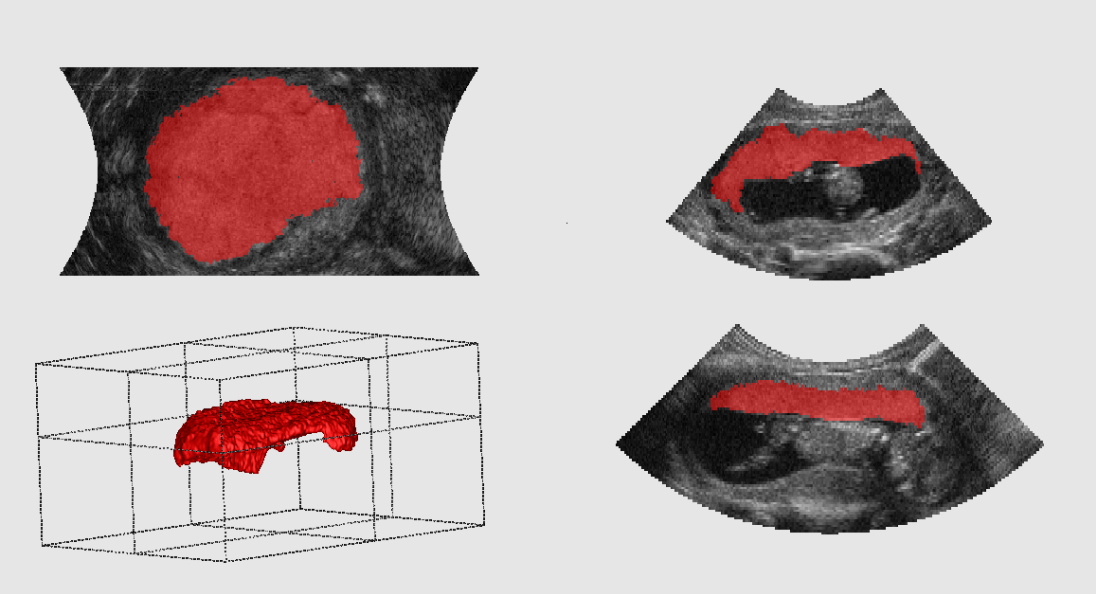

Figure 3.8: 3D segmentation produced by thresholding of probabilities > 0.5. Multi-planar display shown in x(top-right), y (bottom-right) and z (top-left) axes. 3D volumetric rendering of placenta (bottom right).

size of the linear system. A second step is the labelling of voxels outside the ultrasound cone of signal can be simply relabelled as background nodes due to their intensity being equal to 0 whereas any US information has intensity > 0. Both these steps reduce the overall size and number of unmarked nodes and are performed as a pre-processing step prior to the partitioning and creation of the linear system.

A number of other steps can be performed to optimise further the speed of segmentation. The usage of a linear solver that provides the potentials x_u in the fastest possible time will have a large impact. In first producing the algorithm, the VNL numeric library was initially used to solve Equation 3.7 as it is bundled with ITK used in a large portion of this research. Further investigation however, shows that there are linear algebra libraries that provide superior performance than VNL. A study of 58 placental volumes was performed using different linear solvers on an single core of

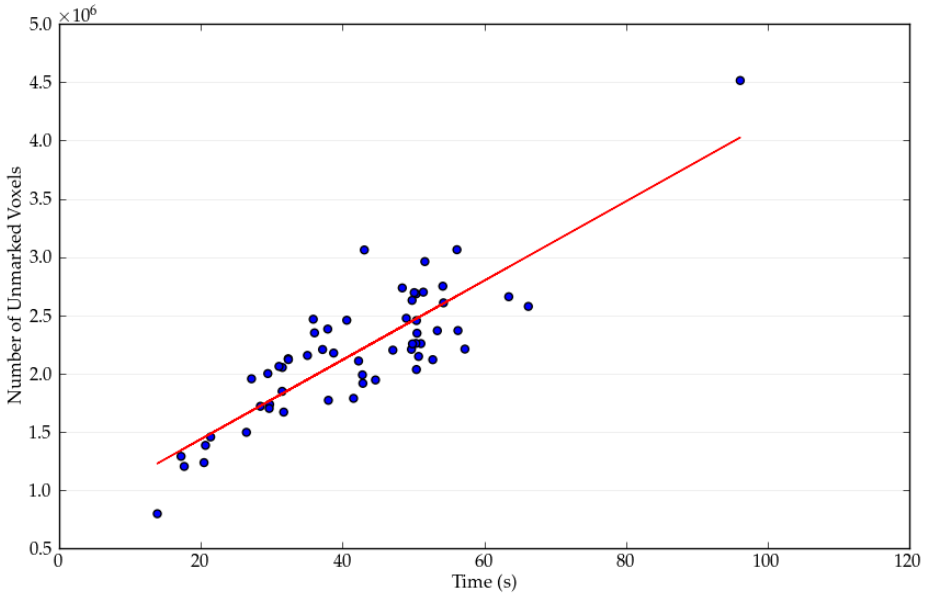

Figure 3.9: Graph showing correlation to increase in time to compute RW probabilities and number of unmarked voxels in the system. Linear regression (red) shows linear trend $R^2 = 0.73$.

an 2.83Ghz Intel® Core™ Quad Q9550. The original VNL conjugate gradient (CG) solver was used and tested in terms of speed against solver methods produced by the linear algebra library, Eigen[148]. The Eigen library provides a variety of different direct and iterative solvers for sparse matrix problems. Testing of three Eigen solvers, one direct (Cholesky decomposition) and two iterative (CG and biconjugate gradient stabilized method (BiCG)[149]). Figure 3.10 shows the different speeds of solution by switching between the different linear solvers. The mean values of segmentation speed and standard error (SE) were calculated as followed, VNL CG: μ = 115.32s SE = 5.10, Eigen Cholksey: μ = 160.48s SE = 7.07, Eigen CG: μ = 59.52s SE = 2.59, Eigen BiCG μ= 43.60s SE = 2.00.

The use of 3D RW in measurement of the placenta is shown to be feasible and a

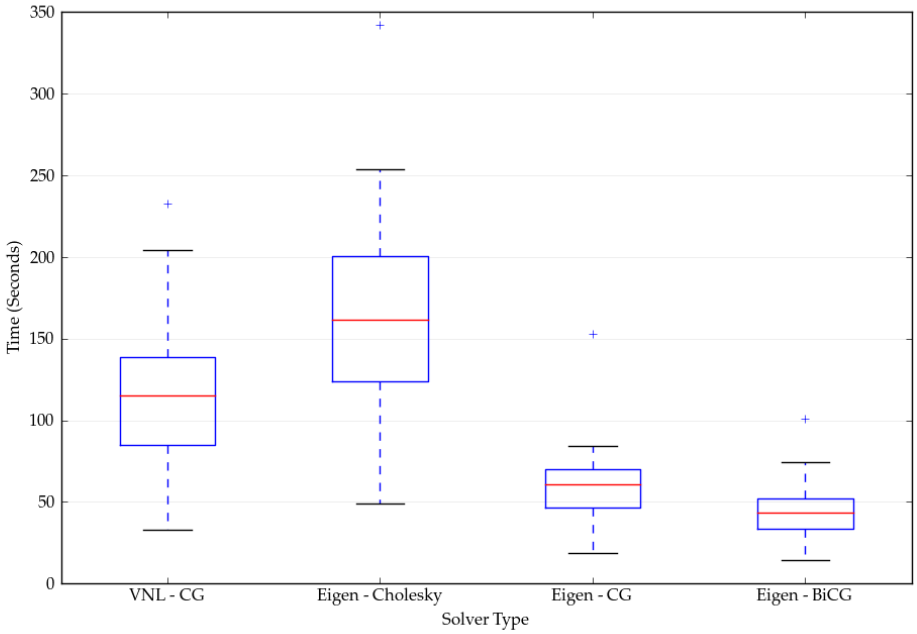

Figure 3.10: Box and whisker plot of time taken to produce RW segmentation versus choice of linear system solver.

result processed in under a minute (43.60s for Eigen BiCG). As all results from this study were compared in volume size to insure that a numerically stable volume was produced for each segmentation we can have confidence that each solver is providing consistent results. With use of Eigen there is potential to port the system to being calculated using a graphics processing unit (GPU), providing parallelism and potential real-time performance through OpenCL™ and ViennaCL[150] that can interface to Eigen classes and datatypes.

Having implemented a stable 3D version of the existing RW technique, the next step was the investigation of using RW against other segmentation methods for the placenta. The next section introduces a study of placental volumes measured using three different segmentation techniques and the statistical analysis produced to determine if

RW can provide a stable, repeatable method for a fast segmentation method for the placenta.

3.4 Validation

The objective of the validation of the algorithm was to evaluate whether this new technique for segmentation of the placenta could perform concordantly or better than manual delineation or the current state-of-the-art semi-automated method, VOCAL^{TM} . We hypothesis that placental volume can be measured by the new technique and produces repeatable and consistent result when compared to manual tracing and the VOCAL^{TM} method.

3.4.1 Method

3D ultrasound scans of the placenta were performed on 10 women with anterior placental implantation and a maternal BMI < 25. Scanning was performed using a GE Voluson®E8 (GE Healthcare, Milwaukee, WI,USA) and two observers (Gordon Stevenson (GS), Dr. Sally Collins (SC)) performed measurement of placenta volume manually, using VOCAL^{TM} and using the new volumetric method on the same scan. Each observer repeated their measurement three times for each technique. Manual tracing was performed by sweeping through each slice in the 3D volume in the original B-mode plane outlining the placental surface - no interpolation was used as in the multi-planar method in order to minimise any error caused by this calculation. Manual tracing was performed using ITK-SNAP (Department of Radiology, University of Pennsylvania, Philadelphia, PA, USA)[151] and saved to disk for later analysis. Placental volume calculation was performed using the VOCAL^{TM} tool using manual

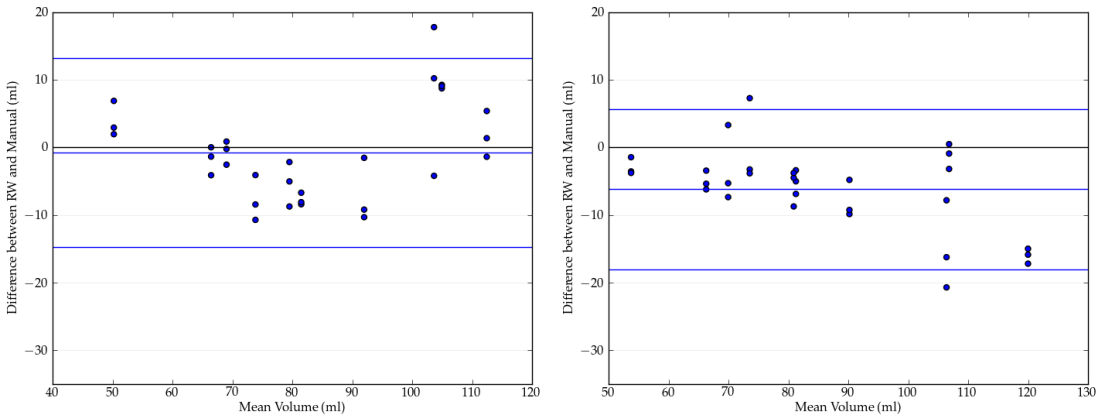

(a) (b)

Figure 3.11: Bland Altman plots illustrating measurement difference between RW and Manual segmentations for Observer 1 (Fig. 3.11a) and Observer 2 (Fig. 3.11b) against mean volume.

tracing every 15° around reference poles centred on the middle of the placenta as best determined by the observer. Placental volume was recorded and the image discarded as only a fully licensed version of the tool allowed the volumetric results to be saved to disk. Random Walker was used upon the images using initialisations from ITK-SNAP and a protocol defined in Appendix A. The β value outlined in Equation 3.2 was set to 0.01. The initialisation images and VOCAL^{TM} tracing were performed using the same touch-screen tablet (Cintiq 20WSX, Wacom Co. Ltd, Otone, Saitama, Japan). Measurement difference was plotted using the method of Bland and Altman[152]. Differences between VOCAL^{TM} and RW against manual were compared with mean difference, μ and limits of agreement defined as $\pm 1.96.\sigma$ from μ. Evaluation of inter/intra observer variability was performed using intra class correlation co-efficient (ICC), having tested for normality of the data using the Lillefors and Kolmogorov-Smirnov test.

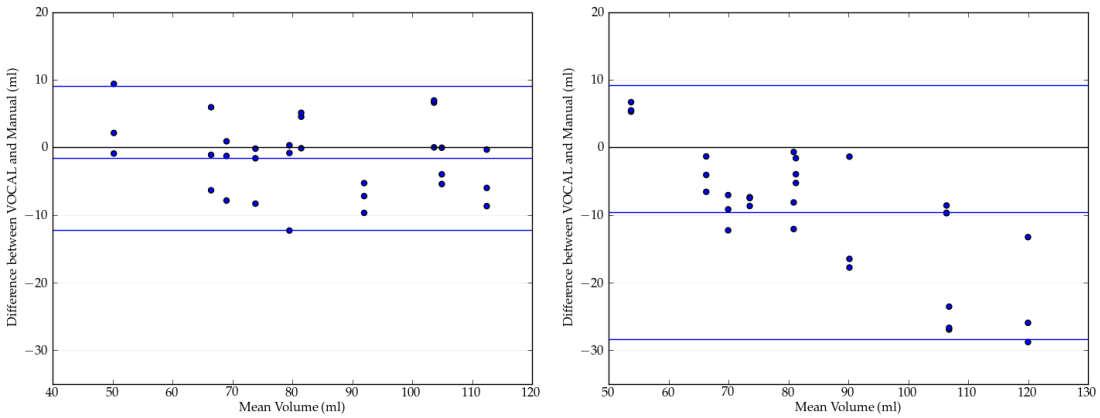

(a) (b)

Figure 3.12: Bland Altman plots illustrating measurement difference between VOCAL^{TM} and Manual segmentations for Observer 1 (Fig. 3.12a) and Observer 2 (Fig. 3.12b) against mean volume.

3.4.2 Results

Table 3.1 shows the mean differences and limits of agreement between the two automated methods and manual segmentation. Although we are measuring an object that intrinsically has an unknown volume we use manual segmentation as a reference in terms of repeatability and absolute value. Using the method proposed by Bland and Altman the differences between measurement type is plotted against mean volume which allows a better understanding if differences are related to volumetric size. Figures 3.11a and 3.11b show differences between volumetric values produced by the RW method against the manual for both observers, Figures 3.12a and 3.12b show the differences between VOCAL^{TM} and manual measures. Mean difference and limits of agreement (LOA) show that RW and VOCAL^{TM} seem to provide similar volumetric results when compared to manual segmentation with no significant differences between measurement. The Bland-Altman plots show that for observer 1 there seems to be no association between measurement and placental volume. However, observer 2

shows a negative bias as placental volume increases showing both the RW volume and VOCAL is smaller in comparison to the manual segmentation. Indeed, this disassociation increases with mean volume. The trend is shown greater in comparing manual segmentations between VOCAL (Fig 3.12b) compared to RW (Fig 3.11b).

Table 3.1: Mean Difference between manual and the two different segmentation methods with upper and lower limits of agreement (LOA $= \mu \pm 1.96\sigma$.)

	Mean Difference (ml)	
Observer	1	2
RW	-0.78 (-14.73,13.18)	-6.2 (-18.11,5.70)
VOCAL^{TM}	-1.53 (-12.20,9.14)	-9.59 (-28.40, 9.22)

Table 3.2: Inter/Intra-class correlation coefficents (ICC) with 95% confidence intervals of differences between observers using the three different segmentation methods.

	Intra Observer Variability (ICC : 95% CI)		Inter Observer Variability (ICC : 95% CI)
Observer	G.S	S.C	
Manual	0.98 (0.94,0.99)	0.90 (0.76,0.97)	0.94 (0.88,0.97)
Random Walker	0.97 (0.91,0.99)	0.957 (0.88,0.99)	0.906 (0.81,0.95)
VOCAL^{TM}	0.91 (0.77,0.98)	0.928 (0.81,0.98)	0.793 (0.61,0.90)

In absence of the raw segmentation volume from VOCAL^{TM} , only a comparison between global volumetric results can be performed statistically. Typically in the field of medical image analysis, a preferred method is a voxel-wise comparison of calculated volumes. In the absence of this information, the next best statistical testing is at the global level using conformity measurements such as the ICC. Intra and inter observer variability can be measured using this testing; Intra-observer meaning the

variability between a single judge or operator and inter-observer as the assessment of the agreement of many operators upon a single measure.

The ICC measures were calculated using R (version 2.12.2, The R Foundation for Statistical Computing[153]) and the 'irr'[154] package to provide the ICCs and confidence limits displayed in Table 3.2. From the table, all three methods produce ICC values that show no difference to a level of statistical significance. However, the new method outperforms VOCAL^{TM} in aspects of repeatability and demonstrates ICC values concordant to manual segmentation between observers and in repeated testing by an individual rater.

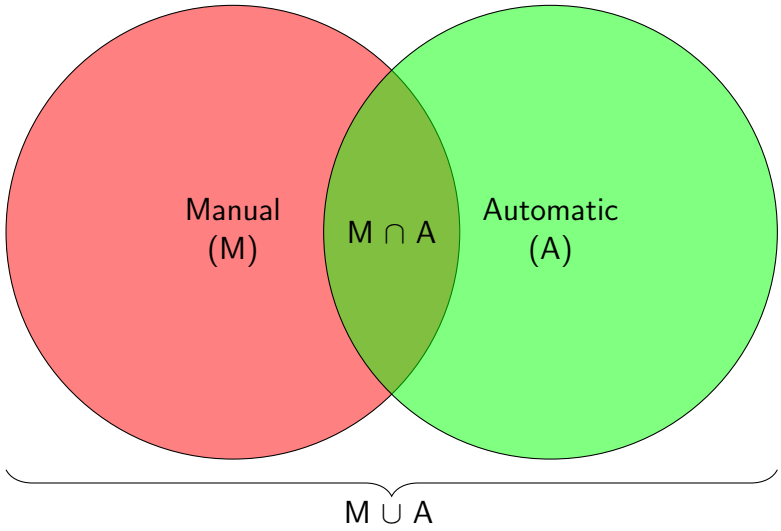

Figure 3.13: Venn Diagram illustrating different measures that can be taken to compute similarity between manual (M) and automatic (A) segmentations.

These global methods show good correspondence between the new method and the ground truth defined as the manual segmentations. With the voxel data available, more rigorous validation can be performed upon the manual segmentations versus the automatic technique. Although this is commonplace in the image processing field this

has not been performed upon any published data using 3D placental volumes. Four segmentation metrics are defined below as Equations 3.8 - 3.11. As VOCAL^{TM} does not allow access to the voxel values of the segmentation volumes, these volumes must be discarded for this portion of the validation.

$$\text{Precision} = \frac{|M \cap A|}{|A|} \tag{3.8}$$

$$\text{Recall} = \frac{|M \cap A|}{|M|} \tag{3.9}$$

From information retrieval, precision is defined as the fraction of information found that is relevant and recall the fraction of relevant information that is found.

$$\text{Dice's Coefficient} = \frac{2\,|M \cap A|}{|M| + |A|} \tag{3.10}$$

$$\text{Jaccard Similarity} = \frac{|M \cap A|}{|M \cup A|} \tag{3.11}$$

Equations 3.10 - 3.11 show two segmentation metrics that illustrate the correlation between the intersection of ground truth and automatic volume compared to the union of the two methods. All four metrics were measured for automatic volumes versus manual segmentations taken for all the observers the mean values over the 30 volumes

(10 volumes segmented three times) is shown in table 3.3.

Table 3.3: Similarity measures of automated versus manual segmentation for three observers

	Accuracy Measures ($\mu \pm 1.96\sigma$)			
Observer	Precision	Recall	Jaccard	Dice
GS	0.84 ± 0.12	0.88 ± 0.06	0.75 ± 0.09	0.86 ± 0.06
SC	0.93 ± 0.08	0.81 ± 0.10	0.76 ± 0.09	0.86 ± 0.06
JD	0.84 ± 0.11	0.91 ± 0.06	0.78 ± 0.11	0.87 ± 0.07
All	0.87 ± 0.13	0.87 ± 0.11	0.76 ± 0.10	0.86 ± 0.06

Mean values for precision, recall, Dice's coefficent and Jaccard similiarity were computed for each observer and summed to show values for all observers. Limits of agreement were calculated as plus or minus 1.96 of the standard deviation from the mean. Indices range between 0 and 1 where 1 indicates perfect similarity and 0 complete disassociation. The results show small differences between results from SC compared to the other two observers in terms of precision and recall. Whether this is due to her being more familiar with scanning as an experienced clinician is a hypothesis that has not been explored in more depth. The Dice and Jaccard similarity measures show very similar results irrespective of observer, which seems to be a very positive result in line with the ICC measurements showing good correlation at a global level.

3.4.3 Addition of Third Observer

Building from this work, a third observer then performed segmentation upon the same dataset three times manually and with the RW method using the same method as described in Section 3.4.1. The new observer JD was an clinical researcher untrained in

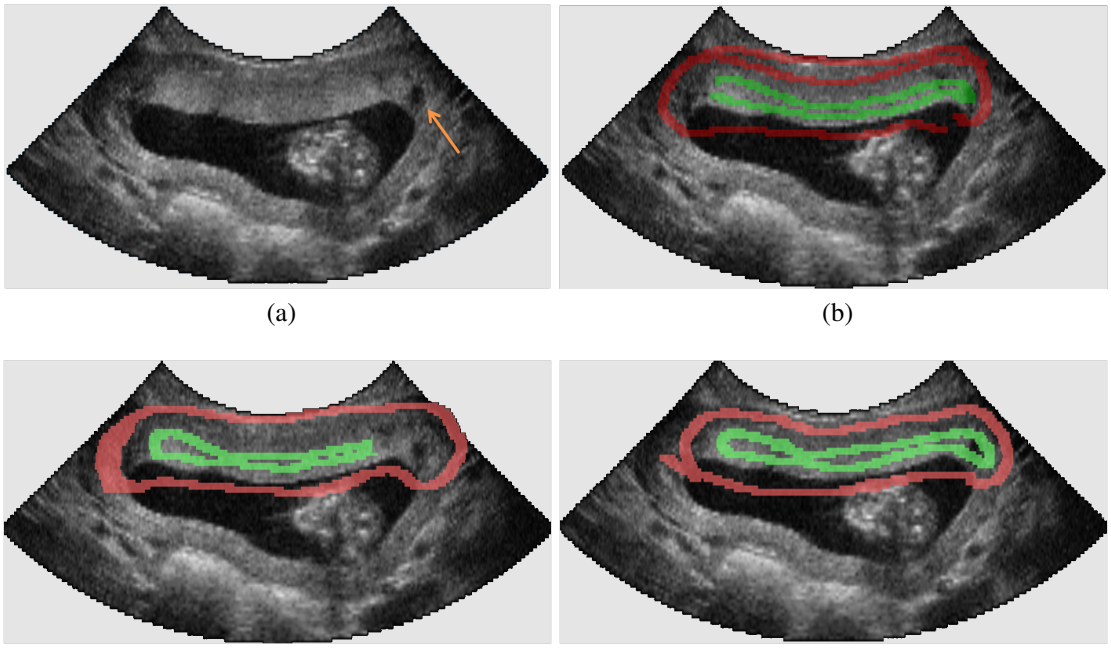

(a) (b)

(c) (d)

Figure 3.14: Seeding/Initialisation for a 3D volume containing cystic area of the placenta (Figure 3.14a); Figure 3.14b - initialisation by GS; Figure 3.14c - initialisation by JD and Figure 3.14d - initialisation by SC. Orange arrow indicates area of cystic tissue within the placenta in Fig. 3.14a. Differences in initialisation between the three observers in this area can be viewed in Figures 3.14b - 3.14d.

sonography and image segmentation. The researcher was first trained in the technique using data outside of those used in validation study to familiarise herself with the use of the touch-screen, the imaging applications used and the segmentation protocol. The protocol is described in Appendix A to illustrate how manual initialisation should be performed.

From initial training, it became apparent that a number of subjects were highly underestimated by JD compared to the other observers, GS and SC. Figure 3.14 illustrates the source of the problem where cystic areas at the periphery were not labelled as part of the placenta. This discrepancy resulted in an amendment in the segmenta-

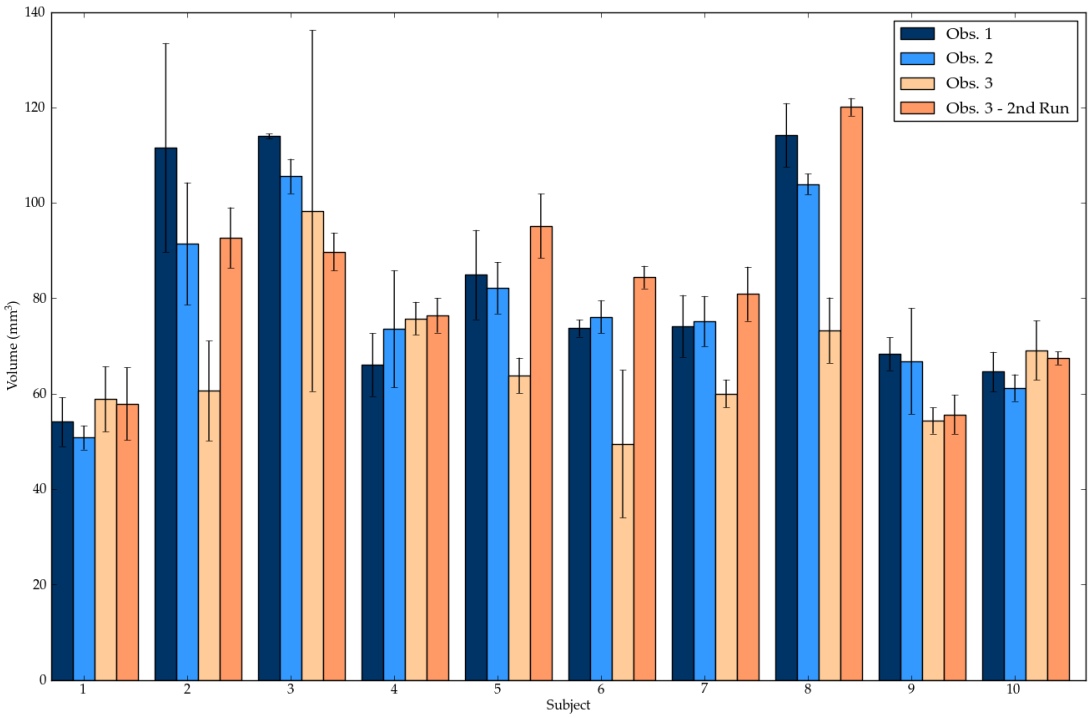

Figure 3.15: Volume estimation for each observer and the results of the retraining of observer 3 (JD).

tion protocol with a section on the annotation of slices containing cystic areas of the placenta as shown in Figure 3.14a. In the absence of the typical homogeneous texture pattern of the placental tissue, the observer decided against defining this portion as part of the organ based on the uncertainty of whether the tissue was placenta or not. By a combination of viewing this type of tissue in other volumes, and by moving back and forth between slices around the 2D imaging plane of interest weak edges showing the association of this tissue to the placenta were better perceived. The volumes were re-initialised by the observer using this new technique to view the slices in a dynamic setting and the results for mean volume between the three initialisations are displayed in Figure 3.15 with the mean volume results prior to re-training.

This result showed that without training in the proper initialisation of the placental

volumes, underestimation of the final result can occur. This shows a disadvantage to the algorithm that a degree of training is required to provide consistent results. However, training is not extensive and once performed results between the three different observers were concordant to manual segmentation.

3.5 Clinical Study [2]

Following the validation process, the algorithm was applied to a clinical population in early pregnancy with the objective of investigating if placental volume was an indicator of a small-for-gestational age (SGA) baby. The placental quotient (PQ) uses the volume (V) divided by the crown-rump length (l), a typical 2D clinical ultrasound measure of the length of the fetus from the top of the head to bottom of the buttocks ($PQ = \frac{V}{l}$). This association allows one to demonstrate if the placenta is too small or large in relation to the size of the fetus [142]. We chose to extend this work by making the index dimensionless so as to remove any measurement bias from the method. Namely, we define a new dimensionless index, ψ defined as $\psi = \frac{V^{\frac{1}{3}}}{l}$.

3.5.1 Method

The study was conducted with national health service (NHS) research ethics service (REC) ethical approval (REC ref: 08/H0604/163) with written consent obtained before enrolment. 143 women with a singleton pregnancy were scanned between 11 weeks

[2] This collaborative work was produced in partnership with clinical researchers at the John Radcliffe Hospital. In particular, the data acquisition, seeding of the algorithm, statistical analysis and discussion were contributed by Dr. Sally Collins. The author provided the calculation and validation of the volume results as well as contributed toward the experimental design, methodology and discussion.

6 days and 13 weeks. Any women under the age of 16 years, those with a BMI >35, or significant maternal chronic illness including diabetes, or treatment with medications such as beta-blockers[155] were excluded from the study. The study involved two ultrasound scans, the first at between 11 and 13+6 weeks and the second at 23 weeks. Gestational age was calculated from the crown-rump length (CRL)[156] at the first visit.

3D volumes were acquired using an RAB4-8-D 3D/4D curved array abdominal transducer (4-8.5 MHz) using a Voluson ® E8 scanner (GE Healthcare, Milwaukee, WI, USA) with the subject in a semi-recumbent position. Each volume was acquired and checked to ensure that the whole placenta had been included in the acquisition and the segmentation was initialised by the same observer off-line after the scan session.

Using an M6C curved array transducer the uterine arteries were measured at both the first and second scan with pulsatility index (PI) and resistance index (RI) calculated over at least three cardiac cycles. The mean of these values were calculated for the left and right vessels and recorded to provide values for mean uterine artery Doppler indices (mean Ut A PI/RI).

The customised birth weight centile was calculated for each baby using the Grow^{TM} software package (version 7.5.1, West Midlands Perinatal Institute, Birmingham, UK). small-for-gestational age (SGA) was defined as $<10^{th}$ centile on customised birth weight charts as calculated using the software. A normal pregnancy outcome was defined as an uncomplicated live-birth after 37 completed weeks of gestation, customised birth weight $\geq 10^{th}$ centile (i.e AGA babies), no admission to the special care baby unit (SCBU) and no evidence of maternal hypertensive disorders or gestational diabetes. The threshold value in determining SGA when performing ROC curve analysis was determined using the birth weight model proposed by Gardosi[42] as described in Section 2.2.1, as it represents the clinically most useful predictor of SGA at term.

Where birth weight was less than the 10^{th} centile of the population that subject was considered SGA and if not AGA.

Statistical analyses were performed by SC using SPSS (version 16.0, IBM ® Corporation, NY, USA) and Excel 2004 (Microsoft ® Corp., Washington, USA). The normality of the distributions was tested using the Kolmogorov-Smirnov test, histograms and Q-Q plots. The Mann-Whitney test was used to compare the placental indices PQ and ψ for SGA and AGA babies. The relationships between birth weight, PQ, ψ and the known predictors of SGA (including PAPP-A and 2^{nd} trimester uterine artery PI) were explored using univariate analysis. Multiple regression analysis was then performed to determine the independent risk factors and generate predictive models for SGA. To ensure normality of the models, the distribution of the residual error was examined using Kolmogorov-Smirnov test, histograms and Q-Q plots. The performance of each marker for predicting SGA in the total population, the term normotensive population and the population considered to be low risk at 11 to 13 weeks (midwifery-led care with no known risk factors for pregnancy complications and low risk combined screening test results) were then examined using ROC curve analysis to generate areas under the curve (AUCs). Results were considered to be statistically significant when $p<0.05$.

3.5.2 Results

Of the 143 women that were available to be analysed, 139 women delivered after 37 weeks gestation and 126 were normotensive throughout pregnancy. There were no significant differences in the baseline demographies between SGA and AGA pregnancies.

Table 3.4: Results of univariate linear regression against birth weight

Parameter	R^2 **value**	**ANOVA p value**
Maternal age	0.003	0.54
Maternal BMI	0.03	0.53
PAPP-A (MoMs [a])	0.089	0.001
NT (MoMs [a])	0.04	0.03
βhCG (MoMs [a])	0.01	0.28
1st trimester Ut A PI [b]	0.02	0.12
2nd trimester Ut A PI [b]	0.63	0.03
Booking MAP [c]	$<$0.001	0.95

[a] MoMs = multiple of the median
[b] Ut A PI = uterine artery Pulsatility Index
[c] MAP = mean arterial (blood) pressure

Table 3.5: Differences in placental volume and its derived indices between SGA and AGA pregnancies

Groups compared			**P value**
All SGA	All AGA	V	0.002**
(inc.all hypertensive disorders)	(inc.all hypertensive disorders)	PQ	0.003*
n=20	n=123	ψ	< 0.001*
Term SGA	Term AGA	V	0.006**
(inc.all hypertensive disorders)	(inc.all hypertensive disorders)	PQ	0.008*
n=18	n=121	ψ	0.001*
Term normotensive SGA	Term normotensive AGA	V	0.026**
n=13	n=113	PQ	0.056*
		ψ	0.002*
* Mann-Whitney test ** Regression analysis (controlling for gestation)			

Placental Volume, V, and indices based upon volume and the association to fetal size, Placental Quotient and ψ of the pregnancies resulting in SGA babies were significantly different at 11 to 13+6 weeks to those pregnancies resulting in AGA babies (p=0.002, 0.026 and 0.001 respectively). A significant difference was seen between

SGA and AGA for ψ and V for all term pregnancies and term, normotensive pregnancies but not for PQ (Table 3.5). The AUCs in the prediction of SGA across the whole population by the PQ, ψ and the uterine artery PI are shown in 3.16.

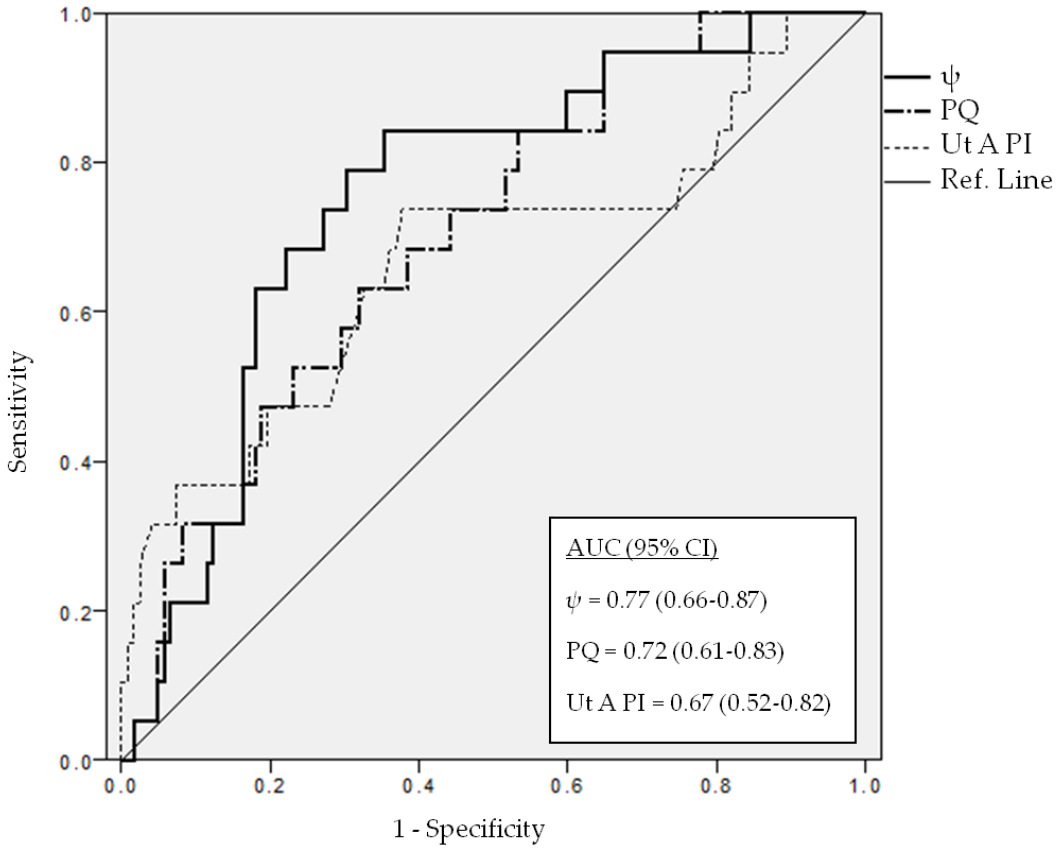

Figure 3.16: Receiver-operating characteristics (ROC) curves for prediction of all cases of SGA using different measures in the whole population

Univariate analysis demonstrated that, in our sample, customised birth weight significantly correlated with PAPP-A (MoMs), NT (MoMs), and 2nd trimester UAD PI. When multiple regression analysis was performed combining these measures with only ψ, PAPP-A (MoMs) and NT (MoMs) were shown to be independent predictors of customised birth weight (Table 3.4). These were then combined to generate a model for

the prediction of SGA.

The ROC curves for prediction of all SGA (including pre-term deliveries and women who developed hypertensive disorders) provide an AUC of 0.80 (0.69,0.92). The combination of these factors provides an improvement upon using ψ alone, demonstrated in Figure 3.17, achieving a sensitivity for predicting all SGA of 67% for a false positive rate of 20%. When the model was applied to predict normotensive, term SGA the ROC curves improved slightly with sensitivities of 83% for a 22% false positive rate. The test was then applied to just the population considered to be low risk at 11 to 13 weeks (n=106). For this population the AUCs remain very good (0.82 (0.69-0.94) and 0.84 (0.72-0.95) respectively) with sensitivity of 70% for 20% false positive rate as shown in Figure 3.18).

3.5.3 Discussion

This study has shown that placental volume and the dimensionless index ψ has the ability to predict term, normotensive fetal growth restriction. Clinically, this is an exciting proposition as we have shown that this can be performed at the first antenatal scan currently offered by the NHS at 11-13+6 weeks. To control for the normal change of placental volume over the 27 day period of the scan either sampling the population or calculating gestation specific multiples of the median (MoMs) needs to be performed or relating the volume measure to another measure considered to be consistent across the majority of pregnancies. The use of the CRL to provide a ratio suggest using ψ or PQ as a marker for the appropriateness of the placenta when compared to the size of the fetus[142]. This method requires no statistical manipulation of the data as gestational

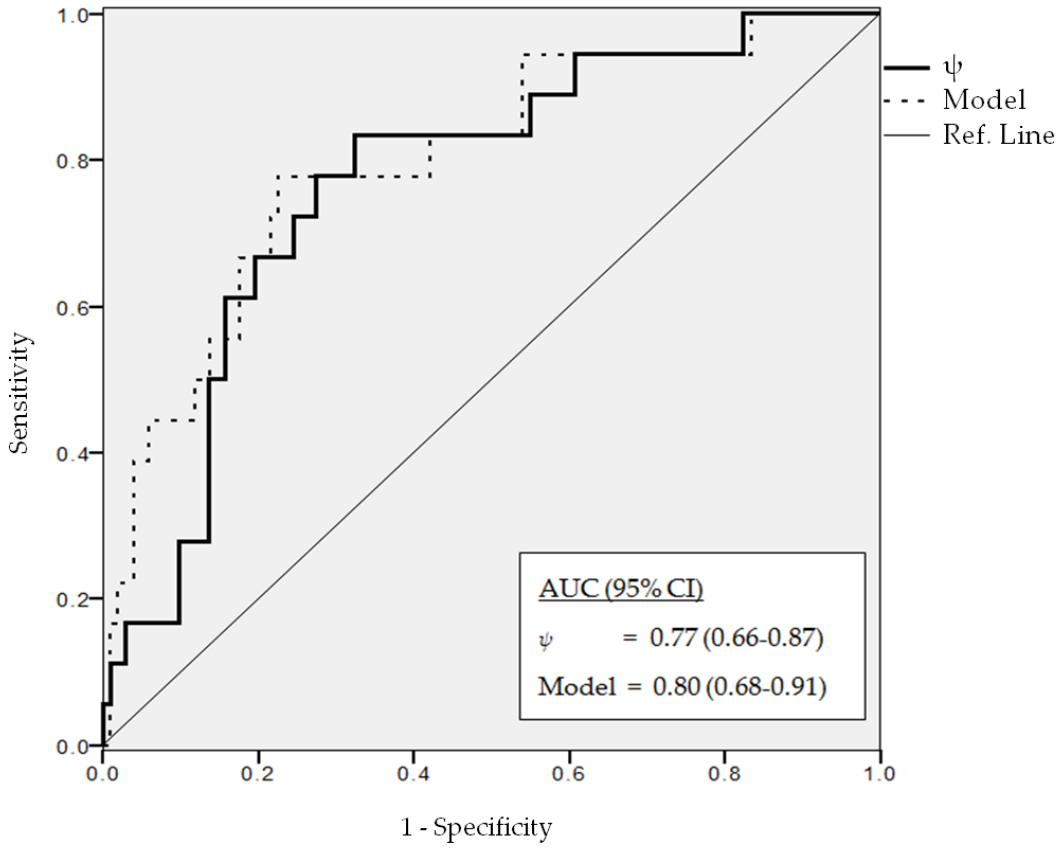

Figure 3.17: ROC curves of ψ and the combined model to predict all SGA in the whole population (including pre-term and gestational hypertensive disorders).

correction is accounted for by the use of the ratio. However, it must be pointed out that we assume that embryonic growth is uniform during the early stages of pregnancy, and how to relax this assumption is non-trivial and beyond the scope of this work.

3.6 Conclusion

This chapter has introduced prior work in clinical measurement of the placental using 3D ultrasound and our new method which underwent validation using different observers and was tested upon on a cohort of 143 woman at their first dating scan at

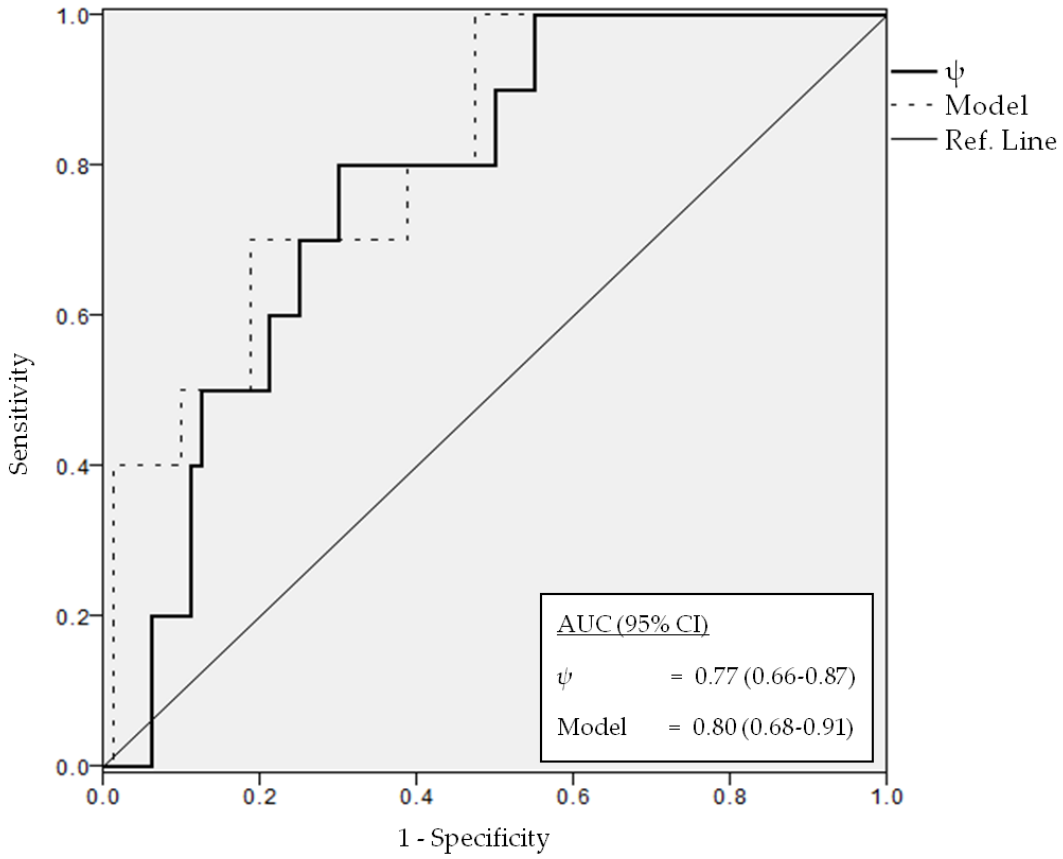

Figure 3.18: Screening ROC curves of ψ and the combined model to predict SGA in a population deemed to be "low risk" at booking

11-13+6 weeks. Placental volume was found to be a predictor of fetal outcome and when combined with other known predictors of fetal outcome such as the blood protein biomarker PAPP-A and 2D fetal measurement of the nape of the neck (nuchal translucency) produced a multivariate regression model that showed that good performance in terms of sensitivity and specificity.

This method shows that placental volume as an imaging biomarker has potential as a predictor of the SGA fetus. Importantly, this method also opens the door to focus on specific areas within and relative to the volume anatomically. Section 2.2 shows the

current thinking and mechanism of spiral artery transformation and the impact upon fetal health when the physiological change described does not occur. The boundary between the placenta and the maternal tissue and the surrounding area is the area in which clinician desire to be able to visualise effectively and measure as this would provide the ability to investigate the area of pathology rather than surrogate markers of upstream flow (uterine arteries) or measurements that require labourious manual intervention as described in section 2.2.3.1. The next chapter aims to introduce a new method to visualise the interface between placenta and mother using a combination of computer graphics and image processing.

Chapter 4

Visualisation of the Utero/Placental Interface

MODERN ultrasound technology provides joint 3D scans of tissue and blood flow in real time from which a complete acquisition of the site of utero-placental insufficient, the utero-placental interface, can be found. To increase our understanding of this anatomical area's role in fetal pathologies such as FGR, we wish to visualise and measure this surface. This is a challenging task as no convincing visualisation solutions for combined US and PD data exist[157]. Currently, no ultrasound imaging tool exists that can easily find and illustrate the interface between placenta and uterus for a clinician without intensive manual intervention. Manual adjustment and manipulation of the volume is time consuming and complicated because of the multi-component nature of the data acquired during a single scan.

We propose a new method to view a biological interface/surface such as the UPI of the placenta from which we can measure properties automatically without user intervention. The key ideas are outlined as follows and described in general terms before

going on to highlight its use in viewing the UPI. Two imaging volumes are acquired, one that describes the anatomy of the volume of interest (VOI) and the other volume that illustrates the movement of fluid or, in the biological case, blood flow. A surface that represents the interface between two layers of the 3D anatomical volume is identified and then "flattened" to provide a 2D morphological map.

The functional volume may have different geometric parameters to that of the anatomical volume, the vascularity at points that correlate to those shown in the B-mode map are parametrised and then overlaid to provide a functional map relative to the location provided by the B-mode information. This mapping process is repeated upon other surfaces that are arbitrary distances away from the original interface as calculated by use of a signed distance transform. From the distance transform, a "stack of surfaces" relative to the original interface can be created and provides a view of the estimated blood flow at the interface and at surfaces relative to it in a 2D domain.

In obstetrics, such a technique to investigate the interface between placenta and mother is desirable for a number of reasons. Prior work has investigated the vascularity either by sampling the placenta as a whole or using small regions of interest to represent the overall organ's vascularity [158,159]. These measures are aimed at producing measurements akin to the uterine artery waveform. That is, they are a surrogate marker of the underlying pathological haemodynamics within the spiral arterioles. Our technique attempts, for the first time, to visualise purely the area of pathology and produce quantifiable measurements.

To quantify this pathological site, we use the volumetric segmentations produced from the work of chapter 3 to provide a geometric base from which to extract the UPI in 3D. The surface is parametrised using the method described in the next section.

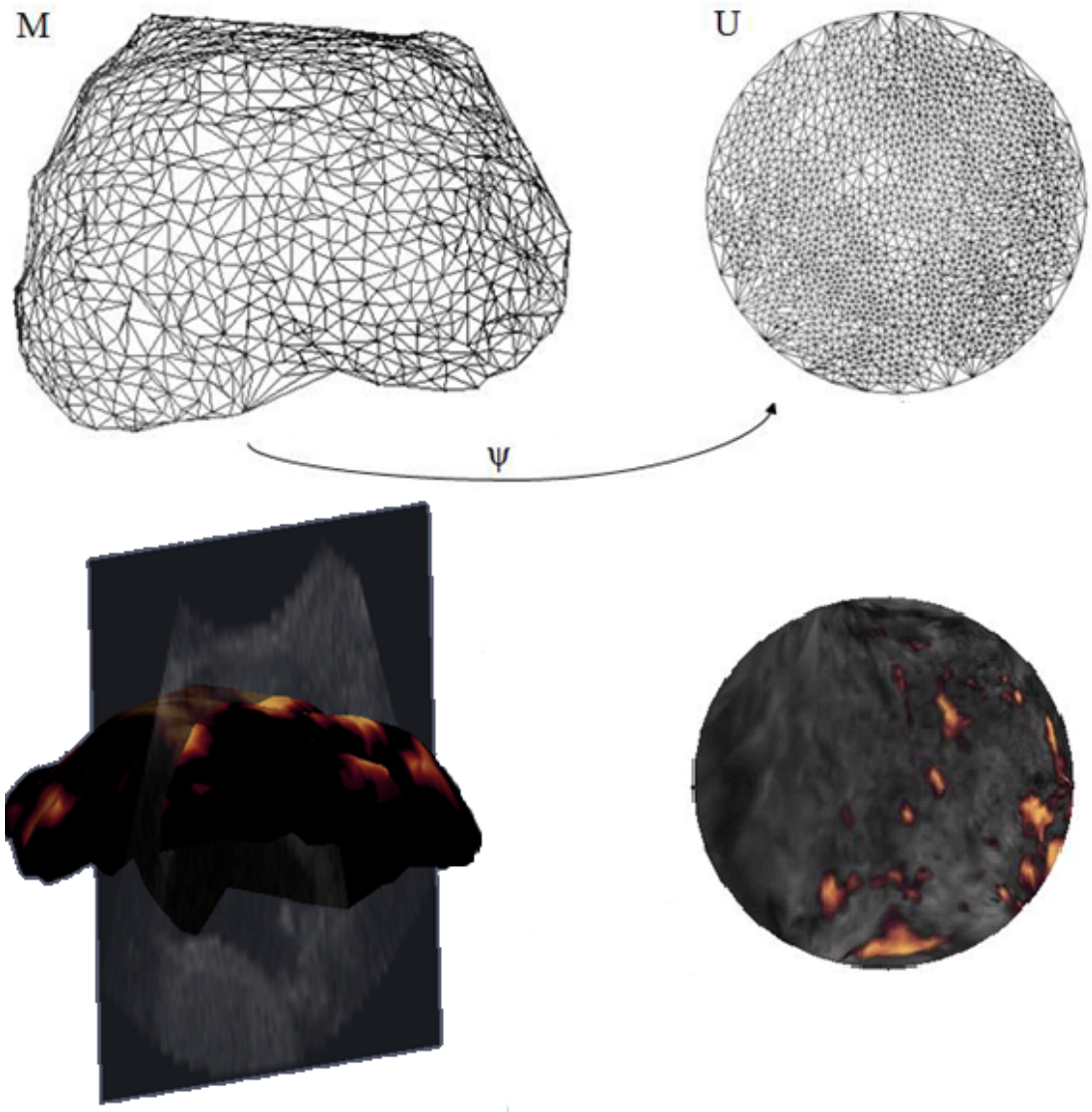

Figure 4.1: A piecewise linear mapping between a wireframe 3D mesh of the placental utero-placental interface $\mathscr{M}$ and an isomorphic flat mesh $\mathscr{U}$. Parameterisation is the calculation of a mapping ψ for each vertex i in the 3D mesh $x_i = (x_i, y_i, z_i)$ to the disc $\mathscr{U}$ where $u_i = (u_i, v_i)$ (top). 3D mesh $\mathscr{M}$ shown *in-situ* as the UPI and colourised based on power Doppler signal at that position in the scan. Result of parameterisation of $\mathscr{M}$ shown on right as disc $\mathscr{U}$.

4.1 Surface Parameterisation

Surface parameterisation allows an isomorphic mapping of a surface to a suitable domain[160]. Mesh parameterisation has been used in a number of scientific and engineering applications in particular in computer graphics for texture mapping[161,162], multiresolution analysis[163] and sparse mesh reconstruction[164]. Increasingly it is being used in medical imaging to aid diagnostic visualisation and determination of anatomy.

In medical imaging, the technique has been used to better understand neural connectivity hidden by cortical folding of the surface of the brain[165] and unfolding of the intestine for detection of polyps that are linked to colonic cancer[166,167]. By flattening the contorted surface of the brain one can reveal whether response recorded by functional magnetic resonance imaging (fMRI) at two points in the brain are truly proximal to one another or actually separated by the ridges and fissures of the cortex or reveal polyps that would otherwise be obscured by the undulating shape of intestinal tissue. These examples demonstrate the flexibility of the method depending on the input surface; as the brain is a closed surface it is visualised spherically[165] whereas open surfaces can be parametrised to a 2D object such as a disc, square or other regular polygon.

Parameterisation has been successfully applied to a number of different areas of medical imaging however the method is not perfect in translating 3D information to the 2D domain and care must be taken in its application. Away from medical imaging, cartography illustrates that parameterisation will produce distortions depending on the mapping used. In the case of the Mercator projection where the projection was used to project rhumb lines (lines that intersect every meridian of longitude at the same angle) used for nautical navigation as horizontal lines on the map at the expense of geometric

area. This is an example of the impact a choice of projection has upon the visualised result. A parameterisation with zero distortion or an *isometric* parameterisation is impossible except when applied on shapes with zero Gaussian curvature such as cylinders or conical sheets. In the real world, a mapping will produce distortion but can be minimised by choice of parameterisation method and weighting. Maps that minimise angular distortion are described as *conformal* whilst those that reduce deformation of area are called *authalic*. Mappings can also be *bijective* where each point on the domain corresponds to exactly one point of the mesh[168] as well as preserve other features described. Section 4.2.1 illustrates how we can adjust the parameterisation framework to provide these mappings and so adjust the appearance of the final visualisation.

We propose to project the 3D surface to a disc. This method provides a fixed disc representation to project so that it provides angle or area preserving characteristics as well being linearly complex to compute[168]. This is attractive for a clinical tool as linearity provides the ability to compute the visualisation in real time. The method is formally described in the next section.

4.2 Formulation

As the biological surfaces we are interested in are open surfaces, planar parameterisation is our focus. The method we use is based upon the two stage process of graph embedding proposed by Tutte[169]. This is based on first finding the boundary vertices of a 3D mesh and fitting them to the boundary of the 2D disc. Then for the remaining interior vertices a linear system is produced to calculate their positions in the 2D domain based on a mass-spring model that is described later. The following is formalised using the nomenclature described in Hormann et al.[164]. Let us denote points in $\mathbb{R}^3$ by

$\mathbf{p} = (x, y, z)$ and points in $\mathbb{R}^2$ by $\mathbf{u} = (u, v)$. It is typical to denote edges and triangles in $\mathbb{R}^3$ as upper case whilst those in $\mathbb{R}^2$ are described in lower case, for example edge $e = [u_1, u_2]$ and triangle $\mathscr{T} = [p_1, p_2, p_3]$.

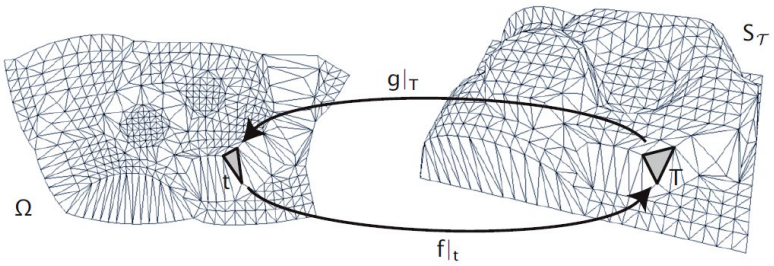

Figure 4.2: Diagram illustrating mesh parameterisation of the triangular mesh $\mathscr{S}_\mathscr{T}$ to the parameter domain Ω. Reproduced from Hormann et al.[164]. ©2008 ACM, Inc. Included here by permission."

A triangle mesh is the union of a set of *surface triangles* $\mathscr{T} = \{T_1, \ldots, T_m\}$ which intersect only at common edges $\mathscr{E} = \{E_1, \ldots, E_l\}$ and vertices $\mathscr{V} = \{p_1, \ldots, p_{n+b}\}$. The vertices can be divided into two groups, n *interior* vertices and b *boundary* vertices defined as $\mathscr{V}_I = \{p_1, \ldots, p_n\}$ and $\mathscr{V}_B = \{p_{n+1}, \ldots, p_{n+b}\}$,respectively. Two distinct vertices $p_i, p_j \in \mathscr{V}$ are *neighbours* if they are the end points of a particular edge and for any $p_i \in \mathscr{V}$ we let $\mathscr{N}_i = \{j : [p_i, p_j] \in \mathscr{E}\}$ be the set of indices of all the neighbours for vertex p_i.

A parameterisation f of S_T can be thought of in reverse by defining the inverse parameterisation $g = f^{-1}$. The mapping g is uniquely determined by specifying the *parameter points* $u_i = g(p_i)$ for each vertex $p_i \in \mathscr{V}$ so insuring that the mapping is bijective between each vertex and each parameter point. With this condition satisfied, each surface triangle $\mathscr{T} = [p_i, p_j, p_k]$ has a corresponding *parameter triangle* $t = [u_i, u_j, u_k]$. The parameter domain Ω is the union of all parameter triangles. Figure 4.2 illustrates a parameterisation of a triangle using the stated notation.

Consider each edge of a vertex in the triangular mesh as a spring that connects two vertices. By first fixing the boundary of this mesh in some static position in the parameter domain and then by relaxing the interior of the network in the most energetically efficient way we can produce the values of the parameter points.

Assume that each spring is ideal *i.e.* the rest length is zero and potential energy is $\frac{1}{2}Ds^2$ where D is the spring constant and s the length of the spring. Then the parameter points for the boundary vertices $\mathscr{V}_B$ are arranged as a boundary in Ω in the form of a planar shape such as a disc or square. For each of the interior vertices $\mathscr{V}_I$, the overall spring energy E is minimised where

$$E = \frac{1}{2}\sum_{i=1}^{n}\sum_{j\in\mathscr{N}_i}\frac{1}{2}D_{ij}\left\|u_i - u_j\right\|^2 \tag{4.1}$$

and $D_{ij} = D_{ji}$ is the spring constant corresponding to the edge connecting p_i and p_j. The partial derivative of E with respect to u_i is,

$$\frac{\delta E}{\delta u_i} = \sum_{j\in\mathscr{N}_i} D_{ij}(u_i - u_j). \tag{4.2}$$

The minimum of E is obtained if,

$$\sum_{j\in\mathscr{N}_i} D_{ij}u_i = \sum_{j\in\mathscr{N}_i} D_{ij}u_j, \tag{4.3}$$

is true for all $i = 1,\ldots,n$. This can be considered the equivalent to that u_i equates to the affine combination of its neighbours.

$$u_i = \sum_{j \in \mathcal{N}_i} \lambda_{ij} u_j \tag{4.4}$$

with normalised coefficients that will sum to 1.

$$\lambda_{ij} = D_{ij} / \sum_{k \in \mathcal{N}_i} D_{ik} \tag{4.5}$$

By separating out the boundary vertices from the interior ones, the interior vertices (u_i, v_i) are found by minimisation of the spring energy which is found by solving the linear systems,

$$A \cdot \mathrm{U} = \bar{\mathrm{U}}, \tag{4.6}$$

where A is a $n \times n$ sparse square matrix with elements,

$$A_{ij} = \begin{cases} 1 & \text{if } i = j, \\ -D_{ij} \Big/ \sum_{k \in \mathcal{N}_i} D_{ik} & \text{if } j \in \mathcal{N}_i, \\ 0 & \text{otherwise.} \end{cases} \tag{4.7}$$

Here $\mathrm{U} = (\mathrm{u}_i)_{i=1,\ldots,N} = (u_i, v_i)_{i=1,\ldots,N}$ is a $2 \times n$ matrix of unknown parameter values (the inner points) and $\bar{\mathrm{U}} = (\bar{\mathrm{u}}_i)_{i=1,\ldots,N} = (\bar{u}_i, \bar{v}_i)_{i=1,\ldots,N}$ is a $2 \times n$ matrix (the boundary points) with coefficients,

$$(\bar{u}_i, \bar{v}_i) = \sum_{j \in \mathscr{N}_i,\ j \in \mathscr{B}} -\frac{D_{ij}}{\sum\limits_{k \in \mathscr{N}_i} D_{ik}} (u_j, v_j). \tag{4.8}$$

Here $\mathscr{N}$ is the group of neighbouring vertices for a particular vertex and $\mathscr{B}$ is a the group of boundary vertices. The linear system described in Equation 4.6 can solved using the same iterative solver techniques that are described in the previous chapter to solve the sparse linear system used in the random walker segmentation. The only remaining issue is the selection of an appropriate spring constant to manipulate the distortion caused by the parameterisation process.

Table 4.1: Formulation and features of spring constants used in barycentric mapping of triangular meshes

Formulation	Name	Bijective	Conformal	Authalic
1	Tutte [169]	✓	✗	✗
$\frac{\cot \alpha_{ji} + \cot \beta_{ij}}{\|x_i - x_j\|^2}$	Wachpress [170]	✗	✓	✗
$\cot \gamma_{ij} + \cot \gamma_{ji}$	Discrete Harmonic [171]	✗	✓	✗
$\frac{\tan \frac{\alpha_{ij}}{2} + \tan \frac{\beta_{ij}}{2}}{\|x_i - x_j\|}$	Mean Value [172]	✓	✓	✗
$\frac{\cot \beta_{ij} + \cot \alpha_{ji}}{\|x_i - x_j\|^2}$	Discrete Authalic [173]	✗	✗	✓

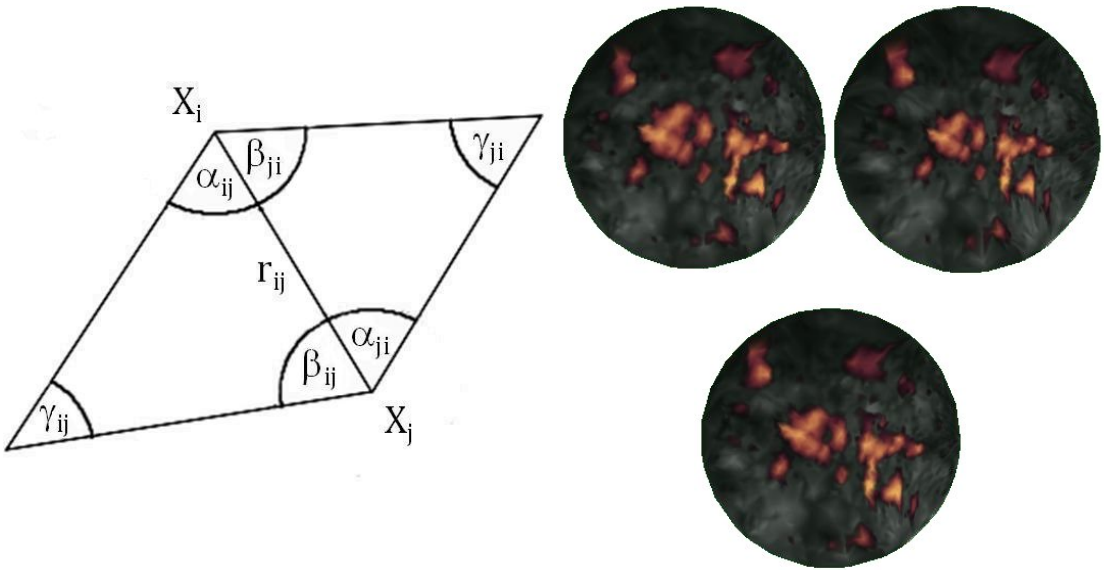

Figure 4.3: Notation of angles and vertices used for spring constants, $D_{i,j}$, in Table 4.1 (left). Resultant parameterisations upon the utero-placental interface using different $D_{i,j}$. Clockwise from top left: Unary, Authalic and Harmonic.

4.2.1 Spring Constant Choice

From a survey of the mesh parameterisation literature, the most popular spring constants that are used and their attributes are summarised in Table 4.1. The simplest spring constant is simply defined as a scalar constant[169] and so provides no minimisation of any distortion but requires no computation and is provably bijective. Other formulations have been proposed and that provide minimisation of angular distortion or shear[171,174]. The most used in the texture mapping community is the harmonic weighting[168] described in[171] however it does lead to drawbacks due to the impact of obtuse angles within the mesh. In this case, negative weightings are produced that lead to a non-bijective parameterisation. A newer weighting method by Floater builds on this work and provides attractive features such as bijectivity and angular preservation[172] . Authalic weightings have been proposed that may be desirable in our application due

to clinical importance of size upon any visualised blood flow. It has been shown that authalic parameterisations although achievable tend to introduce extreme angular and linear distortion [172] so any method must consider angle preservation to some degree [173] such as the discrete authalic formulation shown in Table 4.1

With the parameterisation process explained, we now describe the production of the 3D planar meshes which will be parameterised to generate our visualisation approach. Firstly, given a segmentation of the placenta the function surface where uterine tissue meets the organ, the utero-placental interface (UPI) must be extracted.

4.3 Utero-Placental Interface Extraction

Before parameterisation of the UPI surface itself the anatomical site needs to be accurately identified. Using a 3D segmentation of the placenta as provided by the method described in chapter 3“ a binary volume, V, is produced where a voxel at position (x,y,z) is labelled as described

$$V(x,y,z) = \begin{cases} 1 & \text{if voxel is part of object,} \\ 0 & \text{if background voxel,} \end{cases} \tag{4.9}$$

Extracting the utero-placental interface (UPI) as a discrete manifold is problematic as no general solution exists to perform this step. Extraction by image features and/or geometry is problematic for a number of reasons. The location of the placenta is determined by which uterine wall the embryo initially attaches itself to, the differences in appearance and geometry are described in section 3.2. As extraction of the interface

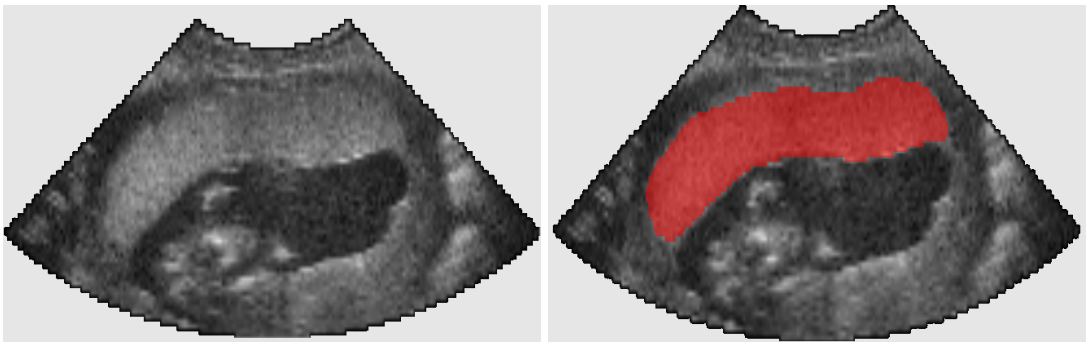

(a) V_{B-MODE} (b) V_{SEG}

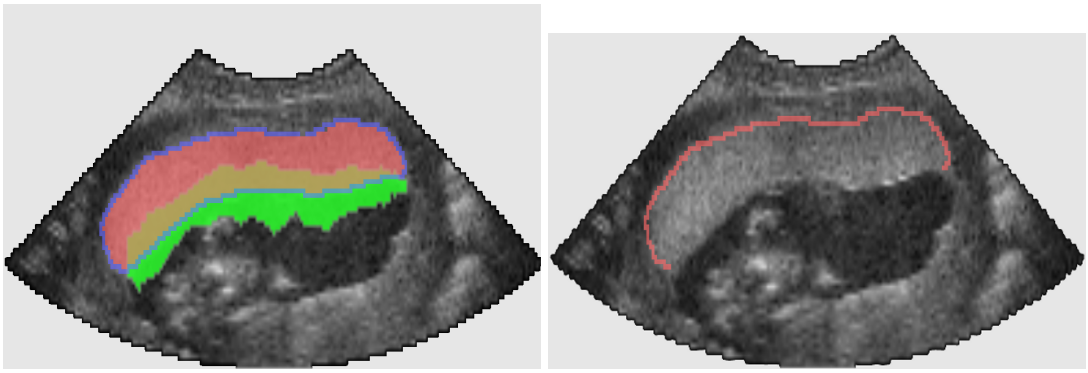

(c) $V_{SEG} \wedge V_{MASK}$ (d) V_{UPI}

Figure 4.4: Process of Utero-Placental Interface (UPI) extraction. The original 2D B-mode image is shown in Figure 4.4a with the segmentation overlaid in Figure 4.4b. The manual masking is displayed in Figure 4.4c and the utero-placental interface extracted by logical operation shown in Figure 4.4d.

is not the primary aim of this thesis, a simple masking technique was used to extract the functional surface of interest. Figure 4.4 illustrates the process. The segmentation volume, V_{SEG}, is cleaned using a simple mathematical morphology technique[175]. It is dilated using a simple spherical structuring element of a radii of 2 voxels and then eroded by the same structuring element in order to remove any small holes within the volume, and any unconnected voxels are removed prior to the plate extraction. This reduces any chance or error in calculation of surfaces using the distance transform should holes within the segmentation volume or unconnected labelled voxels be present. The

outline of the segmentation, $V_{OUTLINE}$, is calculated using a simple zero-crossing filter upon the refined segmentation V_{SEG} (Fig. 4.4b) which is displayed in blue in Figure 4.4c.

By performing logical operations upon the voxels in the image the UPI can be extracted by using an AND filter upon the negative of the volume mask, V_{MASK} ($V_{UPI} = V_{OUTLINE} \wedge \neg V_{MASK}$). By repetition of this operation using the volume mask without negation ($V_{FET} = V_{OUTLINE} \wedge V_{MASK}$) the outline of the placenta that belongs to the fetal side of the organ, V_{FET} can also be produced for later analysis.

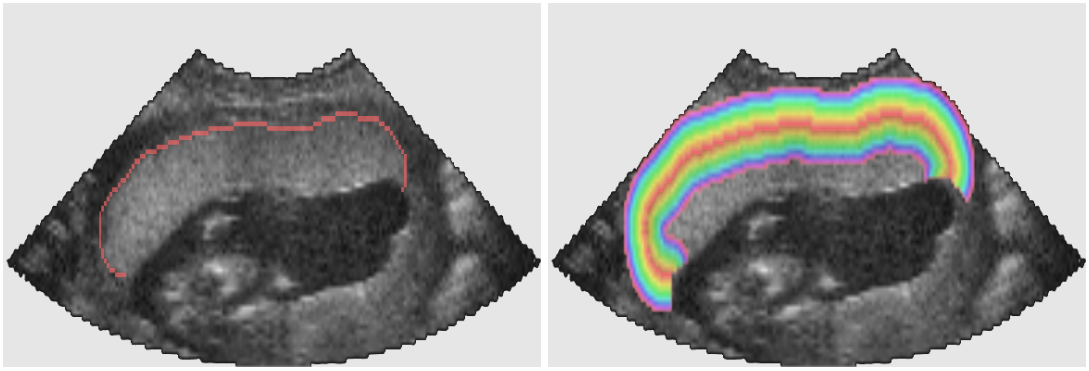

(a) V_{UPI} (b) V_{UPI_EDT}

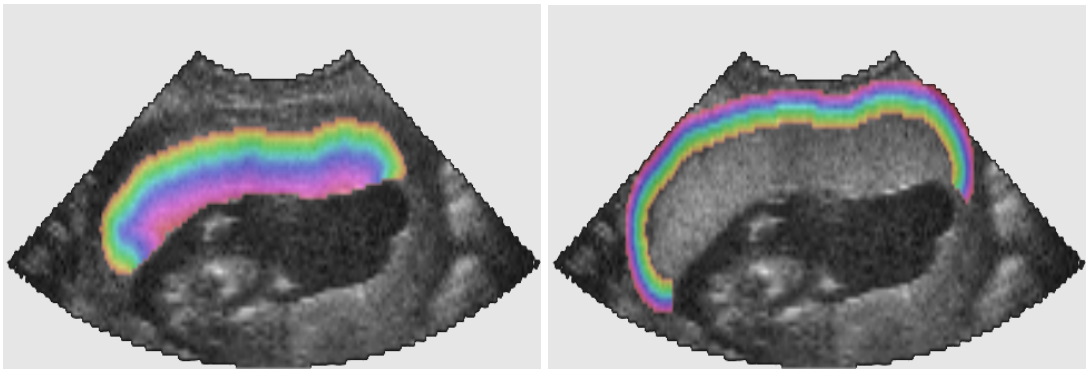

(c) $V_{UPI\_EDT\_PLA}$ (d) $V_{UPI\_EDT\_MAT}$

Figure 4.5: Calculation of Euclidean distance transform (EDT) for the fetal, placental and maternal outlines. Colour mapping indication geometric distances from UPI.

With the UPI delineated in 3D we wish to then determine for all other voxels within the volume the distance to the UPI and its position either inside or out the placenta. A 3D Euclidean distance transform (EDT) is performed upon V_{UPI} (Fig. 4.5a) to provide an initial starting point for this labelling which will finally become the volume V_{UPI_EDT} (Fig 4.5b).

This provides the distances for each position, from the utero-placental interface (UPI) but as the EDT is only a distance measurement, voxels that are part of the amnotic fluid will be labelled as maternal tissue when the aim of the extraction process is to isolate only placental and uterine tissues. Further logical operations are performed upon the EDT in order to isolate only the voxels that represent those of the placenta or those part of the maternal tissue. By removal of the voxels which are closer to the fetal side of the placenta as calculated by the EDT of the V_{FET} we can provide a final distance transform that contains our positions of interest.

Firstly, all the voxels within the placenta as defined by the segmentation volume V_{SEG} have the respective distance calculated and saved into the volume $V_{UPI\_EDT\_PLA}$ which equates to $V_{UPI\_EDT\_PLA} \wedge V_{UPI\_EDT\_MAT}$. Finding the correct maternal labelling is more complex and requires the computation of the EDT of the fetal outline, V_{FET}. The key with this step is the labelling of voxels whose position is outside of the segmentation labelling and has a distance to V_{FET} that is smaller than that of V_{UPI} are labelled with an arbitrary large scalar value out with the bounds of the volume so that are not combined in any visualisation or measurement. This operation is described as $>$ in calculation of the volume, $V_{UPI\_EDT\_MAT}$ which is produced by the following logical operations, $V_{UPI\_EDT\_MAT} = (\neg V_{SEG} \wedge EDT(V_{UPI})) > (\neg V_{SEG} \wedge EDT(V_{FET}))$. Without this step voxels that are part of the fetal anatomy and uterine cavity are labelled as belonging to the uterine vasculature at a set distance. This simple technique allows

consistent masking of the only the uterine tissue for any measurement of the maternal vasculature. A final union operation, $V_{UPI\_EDT\_PLA} \wedge V_{UPI\_EDT\_MAT}$ is performed to produce the final distance transform, V_{UPI_EDT}, which can then be appropriately used in the visualisation process.

4.4 Visualisation of Anatomy Relative to the Utero-Placental Interface

With the determination of the location of the utero-placental interface from the segmentation volume and calculation of the EDT for both the maternal and placental voxels 3D surfaces at discrete distances with respect to the UPI we wish to view a surface within a 3D PD volume. This is accomplished using the Marching Cubes[176] algorithm to compute a polygonal mesh from the scalar field presented as the volume, V_{UPI_EDT}. For our work with ultrasound data, the B-mode data is resampled to the size and spacing of the PD data in this way the accuracy and measurement of any functional data is minimised as we consider the appearance of the PD values to be more important than the B-mode. Figure 4.6 shows the application of the Marching Cubes algorithm upon the scalar field and the extraction of a 3D mesh which is illustrated intersecting a 2D slice of the 3D B-mode volume.

With our mesh of interest found, before we perform our flattening step using the surface parameterisation method described in section 4.1. In order for the parameterisation to be successful we need to ensure that the mesh is well-formed before the parameterisation process is performed. The Euler characteristic, $\chi = V + E - F$ where V is the number of vertices, E the number of edges and F the number of triangles or

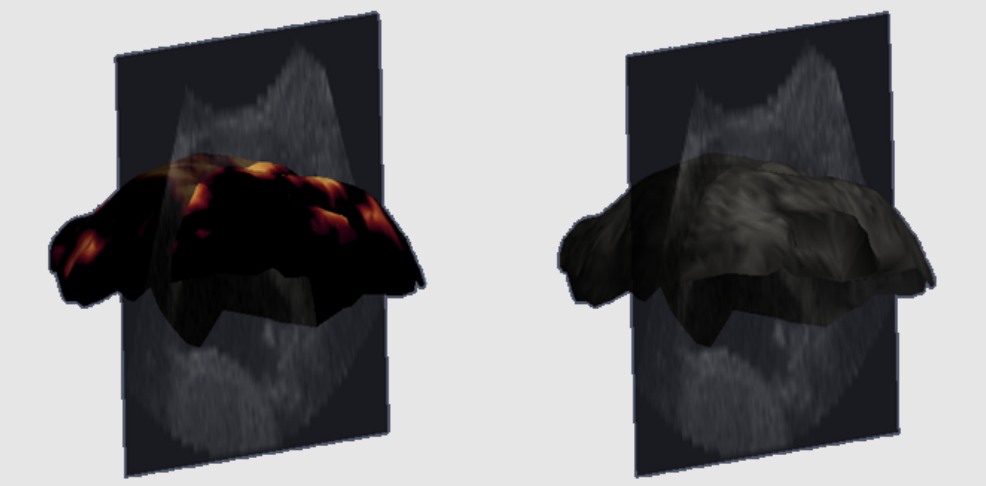

Figure 4.6: Output of Marching Cubes algorithm upon 3D PD (left) and B-mode (right) data at the location of the UPI (i.e. $V_{UPI\_EDT} = 0.0$).

faces that form the mesh provides a simple check that the input mesh has the appropriate characteristics for parameterisation. From this calculation, the shape's genus, or number of holes within the surface, g can also be calculated ($\chi = 2 - 2g$). For parameterisation to be successful, the 3D planar surface mesh must be topologically equivalent to the 2D disc to which it is being parametrised to. This requires it to have a Euler characteristic χ equal to 1 which would lead to a genus, g of 0. These measures provide an understanding of any holes or deformations in the input mesh, a further factor that must be considered is the connectivity of the the triangular mesh produced by the Marching Cubes algorithm. In particular, care must be taken to ensure that the outer faces of the 3D mesh are triangulated *i.e.* have three edges connected to a boundary vertex.

For all our data, there can be no guarantee that an extracted, contoured mesh will meet these criteria in order to be parametrised. To solve this, the mesh is cleaned and amended to fit the appropriate Euler characteristic. Figure 4.7 shows a simple demonstration of the mesh processing required to allow the mesh to be parameterised.

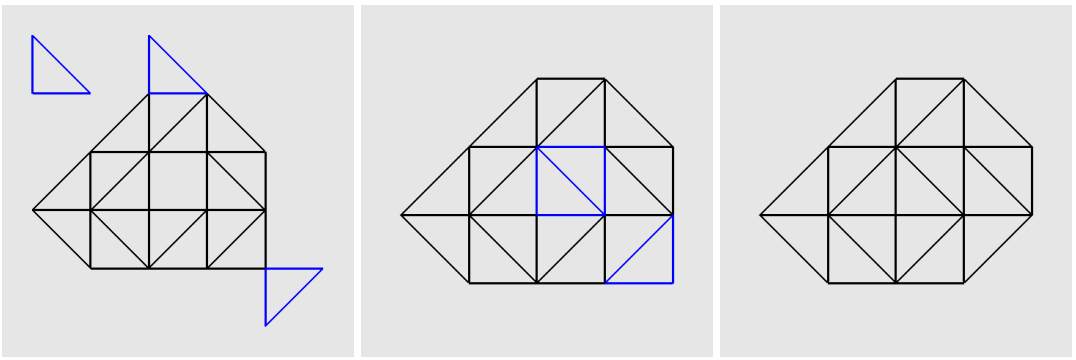

(a) (b) (c)

Figure 4.7: Mesh sanitisation operations on an example mesh, $\mathscr{M}$. Removal of non-manifold triangles and triangles containing "floating" vertices (a). Recursive removal of triangles with "floating" vertices (b). Final sanitised mesh (c).

A toy example mesh $\mathscr{M}$ is shown in Figure 4.7a that illustrates the mesh processing steps performed to sanitise the mesh to make it compatible with the parameterisation method as described in section 4.2.

Firstly, non-manifold triangles (Fig. 4.7a) are removed from the mesh along with boundary triangles which have vertices that are not connected by 3 edges. The non-manifold triangles are highlighted in blue (Figure 4.7a). The connected triangles that violate the vertex connectivity rule are removed recursively until no such triangles are part of the mesh as shown in Figure 4.7b. Finally, as the Marching Cubes contouring algorithm gives no guarantee to the quality or condition of the output mesh[177] any non-triangular polygons that exist within the mesh are appropriately converted into constituent triangular parts as shown in the centre of mesh $\mathscr{M}$ in Figures 4.7b and 4.7c. Following these cleaning or sanitisation steps, the mesh should satisfy the criteria to then perform the parameterisation process.

Given that, we can extract any number of input meshes from our Euclidean distance

Algorithm 1 Produce "stack" of parameterised surfaces from a 3D PD US volume

procedure CREATEVISUALISATION
  $x_{min} \Leftarrow -5.0$ ▷ value set to -5.0 mm inside of the placenta relative to UPI.
  $x_{max} \Leftarrow 6.0$ ▷ value set to 6.0 mm outside of the placenta relative to UPI.
  for $i = x_{min} \rightarrow x_{max}$ step 1.0 **do**
    Contour surface by isosurface i to create mesh $\mathscr{M}_i$
    Append scalar values from PD and B-mode volumes onto $\mathscr{M}_i$
    Sanitise $\mathscr{M}_i$
    Parameterise surface $\mathscr{M}_i$ to $\mathscr{P}_{\mathscr{M}_i}$
  end for
end procedure

transform volume $V_{UPI\_EDT\_MAT}$. To investigate the areas in and around the placenta we propose a technique as described in the pseudocode of Algorithm 1. We wish to view discrete slices relative to the UPI of the placenta. We can then view a "stack" of discrete surfaces which are in a range of distance with respect to the UPI. These can then be arranged in a grid-like fashion similar to that produced in a CT of the abdomen or head to demonstrate discrete slicing through the body. A 6×3 grid of parameterised discs is displayed in order of distance from furthest into the maternal uterus in the top left to furthest into the placenta in the bottom right. This allows the user to track the PD signal found at these locations relative to the UPI from the area where large amounts of vascularisation should be present in the maternal tissues to where it enters and diffuses into the intervillous space.

Figures 4.8 and 4.9 show experimental results for a placenta for whom surfaces were extracted at two separate scanning acquisitions, at 12+5 weeks and 14+1 weeks, respectively. They both show discrete slices at 1.0mm intervals starting from 6.0mm "outside" the placenta *i.e.* in the maternal uterus and moving toward the utero-placental interface (highlighted with a green background in the figures) before moving into the placenta away from the UPI up to -5.0mm into the organ. These bounds were de-

termined based on anatomic evidence that the vessels that supply the placenta are up to 10mm away from the UPI[10] and from observation using 2D colour Doppler ultrasound of blood flow entering into the placenta[90]. Using these bounds should adequately capture both arterial blood supplying the placenta, and the ingress of blood travelling into the organ. Both figures show individual spurts of blood flow present in the IVS that can be tracked as we investigate slices relatively toward or away from the UPI. We also show that we are producing a method that reflects the underlying vasculature as described by anatomists and placental histopathologists; a highly vascular network or plexus of vessels is viewed outside the UPI which reduces in degree of vascularisation as we move closer to the UPI and once within the IVS individual "jets" of vasculature are viewed in cordancy with 2D studies of these movements of blood[178]. As introduced in Section 2.3.3.1, the jets as described are defined as 2D spurts of Doppler signal seen in a 2D slice of placenta from the UPI entering into the placenta, when investigated by 2D trans-abdominal ultrasound. Figure 2.9d shows an example of such a jet. These long streams of Doppler signal when viewed in the new method should be presented as circular points of signal that can be tracked between discs.

4.5 Conclusion

By isolation and parameterisation of the utero-placental interface (UPI), we have provided a technique that eloquently visualises the interface between mother and placenta. By measurement of discrete surfaces surrounding the border, we have then shown the differences in blood flow in the maternal tissues compared to that inside the placenta. This technique provides a framework from which better understood and reliable meas-

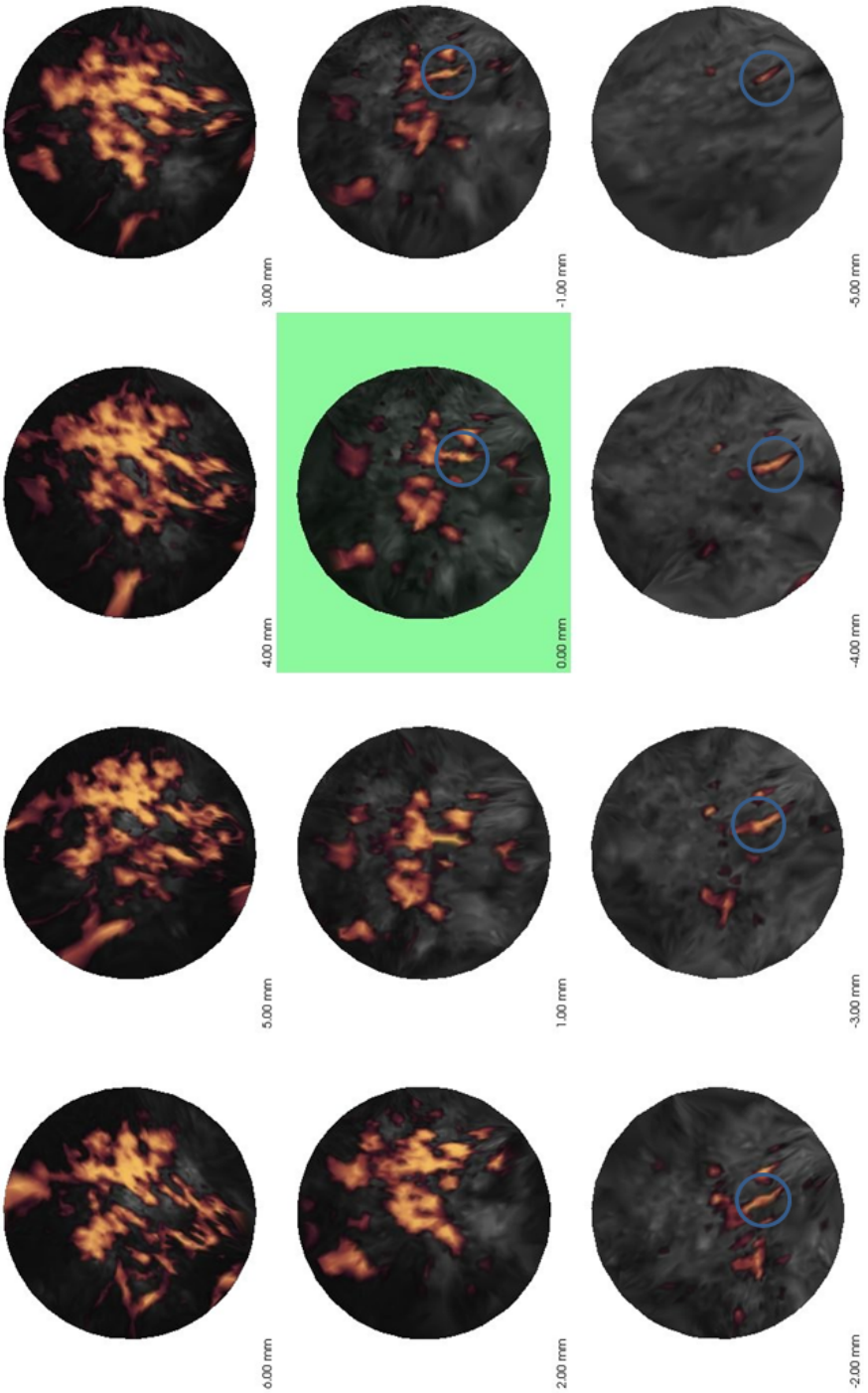

Figure 4.8: Surface parameterisation of the utero-placental interface (UPI) and discrete surfaces away from and within the placenta at 12+5 weeks gestation, Figure 4.9 shows the same placenta several weeks later using the same method.

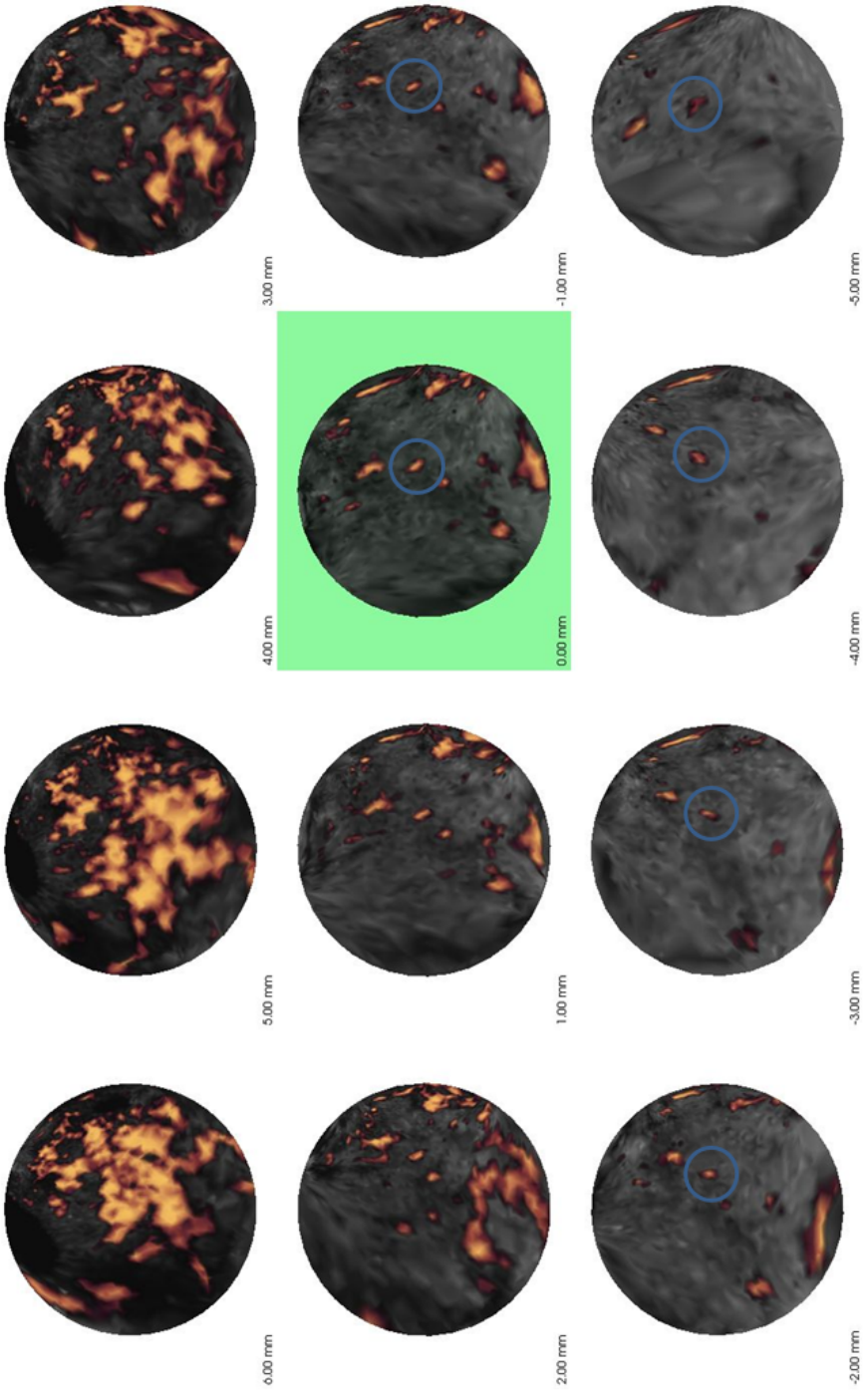

Figure 4.9: Surface parameterisation of the utero-placental interface (UPI) and discrete surfaces away from and within the placenta. 14+1 week gestation.

urements of the Doppler signal within and around the placenta can be carried out. The next chapter will show the current research clinically that has been performed using Doppler ultrasound and how the application of the new technique should provide more robust and reliable measures of blood flow.

Chapter 5

Review of Functional Measurement of the Placenta using 3D power Doppler Ultrasound

QUANTITATIVE evaluation of placental vasculature using 3D PD ultrasound may identify the underlying difference in vasculature that leads to placental insufficiency or abruption before the onset of fetal distress [179] which in turn may lead to better pregnancy management strategies. This is a major clinical need as the underlying dynamics of blood flow and their effect on fetal and placental development are still not completely understood but have been shown to differ in pathological cases [37]. Different techniques, as outlined in section 2.3.3.3, have estimated blood flow using ultrasound. However, there is no single method that overcomes or compensates for the many sources of error that can effect quantification of blood flow using the inherently sensitive technique of PD. By understanding these obstacles to repeatable blood flow measurement and using our placental segmentation method

and new visualisation technique discussed in the previous chapter we propose a better founded solution for placental blood flow measurement in this chapter.

Chapter 4 presented a new visualisation method to identify and evaluate the presence of moving blood flow in and around the basal plate of the placenta, in particular "jets" of maternal blood entering the intervillous space. Measurement of these spurts although of interest to placental pathologists or obstetricians is limited to that specific domain and lacks a degree of generality to other organs, modalities or conditions. A more general technique that marries aspects of this new visualisation method to pre-existing power Doppler measurement techniques which have been validated would show the potential for power Doppler (PD) imaging to provide a robust estimation of blood flow in organs.

In this chapter, we review the typical methods to quantify the power Doppler as currently used in clinical research for measurement of tumour angiogenesis and placental function, and then go on to describe the main experimental sources of error in power Doppler measurement and consider their impact upon a 3D functional measurement.

5.1 Quantification of power Doppler imaging

The estimation of blood movement using power Doppler ultrasound in a specific region of interest has been measured using simple pixel/voxel counting to generate mean pixel intensity (MPI) and colour pixel density (CPD) values that have shown good correlation to underlying blood flow in animal models[180–182]. MPI is simply defined as the mean intensity values of PD pixels in a region of interest and CPD is a ratio of the number of color pixels to the total number of pixels in a region of interest. However, any presence of substantial power Doppler artifact will not provide accurate estimates

of the true vascular volume fraction[183]. More reliable estimates of vascular volume fraction are possible by compensating for depth and attenuation by normalising CPD with a value obtained from the "knee" of the power Doppler cumulative probability density function (cPDF), known as fractional moving blood volume (FMBV)[184]. With the advent of commercial 3D Doppler acquisition inferences about the blood flow using vascular indices in a certain VOI but without the depth normalisation of the FMBV technique[184] which as yet has yet to be measured in 3D. In the next section we introduce the 2D FMBV technique and how it provides compensation for depth and attenuation in the quantification of power Doppler.

5.1.1 Fractional Moving Blood Volume (FMBV)

Any measurement of Doppler signal needs to compensate for a number of factors to provide any kind of consistent measurement of blood flow. In particular, the effect of attenuation will influence any metric taken between different subjects or over time. The varying implantation site of the placenta provides a particularly elegant example of the issue of depth dependency. For example, if a measurement is taken between two identical placentas at different uterine locations, from an anterior placenta to a posterior placenta the extra distance that the beam requires to travel will affect the Doppler values returned. Despite the two placentas being anatomically and functionally similar, the attenuative effect will provide a discrepancy between the Doppler values even before considering other variables.

In[185], Rubin et al. proposed to solve this problem with their technique of fractional moving blood volume (FMBV) estimation. FMBV estimation is a procedure that employs an internal reference vessel in which known consistent flow occurs. From this

reference vessel a maximum value of flow is calculated by a normalisation technique. A different region of interest can then be selected and the values are normalised by the maximal value found in the reference vessel. In this way, FMBV estimation provides a compensatory effect for temporal and subject variability which has been shown to provide less variance than MPI in studies of the human fetal lung[186] and in animal studies[187].

FMBV requires the sampling of a reference vessel or region of interest wherein it is assumed that values representative of a consistent high level of blood flow are present. Such an example of a typical reference areas would be the fetal aorta or adult renal artery. At this location, a region of interest (ROI) is sampled and the PD scalar values stored. The integral of the histogram of the ROI is calculated as the cPDF which discretely is defined as;

$$N(p) = \sum_{i=0}^{i=p} n(i) \tag{5.1}$$

where n(i) is the frequency of pixels with the i^{th} power value and N(p) is the total number of pixels with $i \leq p$. Rubin et al. argue that the use of the cPDF suppresses noise found locally between power values. The power value observed at the "knee" of the distribution has been shown to provide a good normalisation factor[184]. They automatically extract the power value at this position in the distribution using following method described here in a stepwise outline;

1. Using Equation 5.1, calculate cPDF.
2. Perform linear least-squares regression on cPDF.
3. Find the normalisation point by the minimum of;
   (a) The intersection of the tangential lines found where the regression line intersects the cPDF.
   (b) The maximum value of the distribution when the linear fit is rotated onto the abscissa.
4. Repeat steps 1 to 3, using scalars from the first normalisation point found in the previous step to the maximum of the scalar range to find the final normalisation value.

The final step in the method described accounts for the influence of rouleaux formation on the result. This is discussed in further detail in section 5.2.2. With a standardisation point found, the region of interest is then investigated, either being part of the original reference vessel or being a different object in the scene proximal to the reference. An estimation of FMBV is then found by calculating a percent range between the minimum Doppler values found (0%) and the standardisation point (100%). Values above that point are given a value of 100% to provide a fractional estimate of moving blood volume.

A simple phantom study has shown a strong linear relationship between scatterer concentration and received power using FMBV[185] and this depth compensation method has been applied in clinical studies of fetal lung[186], brain[188] and kidney[189]. Importantly, FMBV has been compared to the "gold standard" of blood flow evaluation[88] which is radioactive microspheres (RMS). In animal study using fetal sheep,

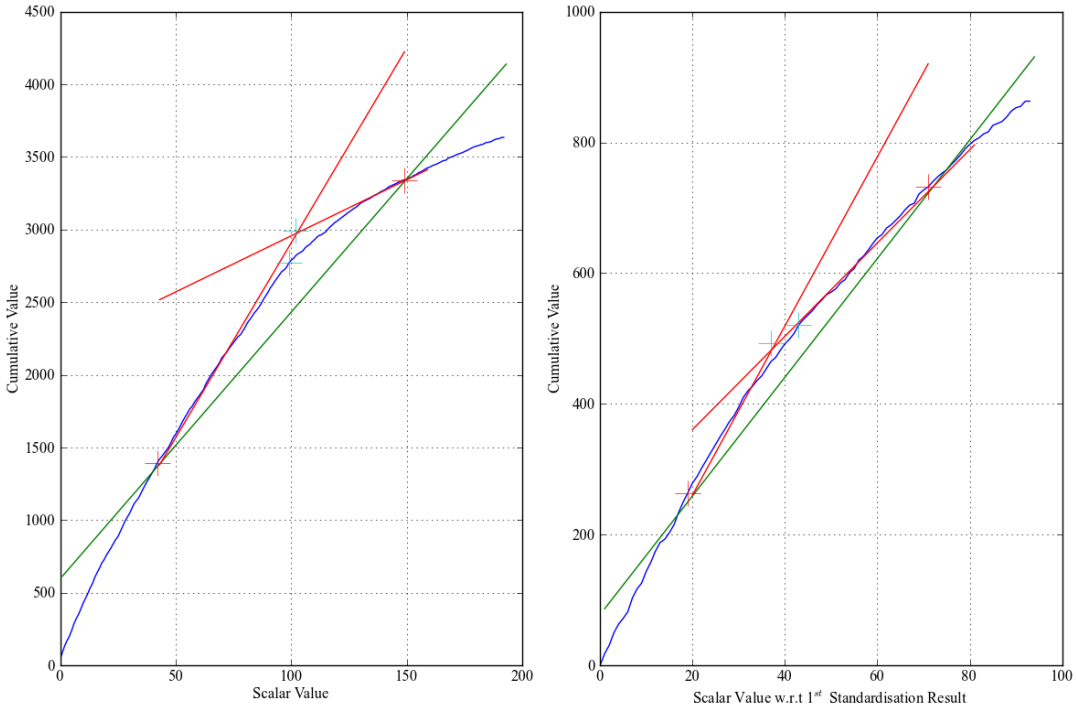

Figure 5.1: FMBV calculation performed upon VOI from 3D PD ultrasound volume. First pass of the algorithm is shown left and then the computation repeat on values from the first standardisation value to the maximum values. Blue line - PD scalar values, green line - linear regression line, red line - tangential lines from intersection between scalars and regression.

asphyxia was induced by occlusion of the umbilical cord what was compared to an observable control group. RMS injections with different labelled isotopes were given before occlusion, 5 minutes afterwards and when mean arterial blood pressure decrease below 25mmHg. Following sacrifice, the nuclear activity of each isotope was calculated and adrenal blood flow was calculated by comparing the number of RMS in reference samples with the number in the adrenal gland, allowing a calculation of adrenal flow in ml/min/Kg. FMBV was correlated to RMS with a median individual correlation coefficient of 0.90 (range; 0.43-0.99). This indicates that FMBV is not a direct measure of blood flow but can be used as a good approximation of it[187]. As described these methods have been performed only within a 2D image and no 3D FMBV

estimation has been attempted using the procedure described in[185]. This method offers currently the only standardisation methodology in the literature that importantly has been successfully validated in animal studies.

3D measurement of power Doppler has been performed without depth-normalisation and the use of the vascular indices which are used to indicate the amount and intensity of vascularisation are the most popular method to estimate vascularity in the clinical literature.

5.1.2 VOCAL^{TM} Indices of Vascularity

The VOCAL^{TM} tool (4D View 10.4, GE Healthcare, Milwaukee, WI,USA) can generate indices based upon the scalar values present in a VOI of a 3D PD volume. This VOI can be created by manual segmentation, the VOCAL^{TM} rotational segmentation technique (Figure 3.3) or using a geometric shape such as a sphere. The B-mode and PD voxels in this VOI are then used to calculate dimensionless indices of vascularity. These voxel values are stored by the ultrasound machine as 8-bit values between 0 and 255. VOCAL^{TM} normalises these to provide indices as percentage values. The indices are defined as the vascularisation index (VI), flow index (FI) and vascularity flow index (VFI) respectively (taken from[190]);

$$VI = \frac{\sum_{c=1}^{100} \mathrm{fc(c)}}{\sum_{g=1}^{100} \mathrm{fg(g)} + \sum_{c=1}^{100} \mathrm{fc(c)}} \qquad FI = \frac{\sum_{c=1}^{100} \mathrm{c.fc(c)}}{\sum_{c=1}^{100} \mathrm{fc(c)}}$$

$$VFI = \mathrm{VI} \times FI = \frac{\sum_{c=1}^{100} \mathrm{c.fc(c)}}{\sum_{g=1}^{100} \mathrm{fg(g)} + \sum_{c=1}^{100} \mathrm{fc(c)}}$$

where g and c indicate the greyscale and power Doppler values and their frequencies at each step are fg and fc representing the respective greyscale and power Doppler modalities. Like colour pixel density the VI is a ratio of presence of PD voxels compared to B-mode voxels, the FI provides a weighted mean of flow "intensity" and VFI is a multiplication of the two to provide a weighting of the two indices. The Doppler value range from 0 to 255 reflecting their value as stored on the machine is scaled by the manufacturer to a range from 1 to 100 when calculating the VOCAL indices.

The reasoning behind this transformation is not discussed in any paper that states the above formulae but consideration of the differences between the B-mode and power Doppler colour maps, one can be appreciate the need for this scaling. The palettes used to visualise the scalar values using the GE VOCAL^{TM} 4D View application are shown in Figure 5.2. The portion of "black" power Doppler values are indicative of those considered too low to be displayed and so are rendered with no opacity over the B-mode data. The choice of cut-off value is unknown but can be adjusted in the commercial viewer as demonstrated in Figures 5.2a and 5.2b, which in turn will alter the value of any measurement indices. The adjustment in 5.2b shows an increased amount of PD values displayed but a proportion of which could be considered noise. We conclude that the linear transformation and normalisation is a requirement in order to make measurements between volumes acquired with five different settings but this is speculative.

There have been over 100 clinical research publications in obstetrics alone using VOCAL^{TM} vascular indices[191] investigating the amount of blood flow present in a variety of organs and in the presence or absence of disease. Despite the number of publications using the method, there remains debate as to the true meaning of the in-

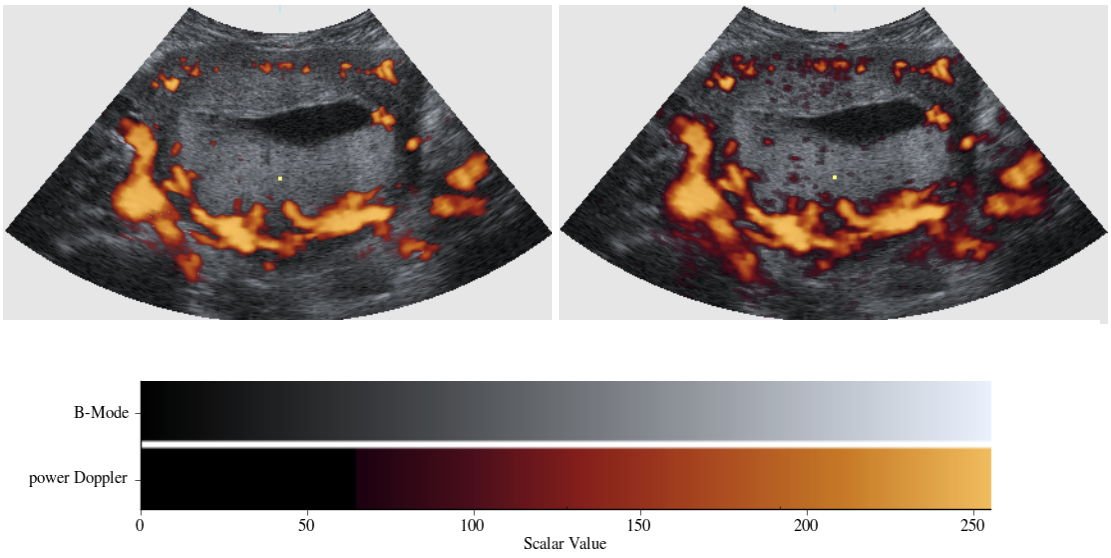

(c)

Figure 5.2: Slices of placenta showing differences in opacity values of the PD colour map. Adjustment of lower bound of palette shows additional Doppler information visualised when comparing 5.2a with 5.2b. Figure 5.2c shows typical colour maps for B-mode and PD modalities with scalar values indicating the minimum, maximum and value at which PD appears.

dices and their correlation to vascular flow[158,192–194]. They have not undergone the careful evaluation as for FMBV on animals and indeed this would be hard to perform due to the blackbox nature of VOCAL^{TM} 's solution. It has been shown that the indices are related to blood flow in *ex vivo* and *in vitro* environments[195–197]. However, their estimation has been shown to be affected by machine settings[198–200], attenuation[195,201] and the size of the sampling volume[159,200]. As VOCAL^{TM} is a commercial product, the underlying processing and calculation is considered proprietorial and so the underlying workings of the method are still not well understood. The manufacturer of the equipment themselves have stated in personal communication to researchers in the field that the technique "cannot be used to assess perfusion within a voxel"[202] despite claims in papers using the method to the contrary. Estimation of flow using

VOCAL^{TM} is uncertain despite its popularity and as a result any measure of the placenta must be performed using an experimental design that tries to dampen the errors using a combination of standardisation and rigorous machine settings.

Table 5.1: Results from comparing similar VOI in three different machines, with the PD quantification application included in their software. Reproduced with permission from Bello-Muñoz[203].

Fetus	GE Voluson E8			Philips iU22			Medison Accuvix V20		
	VI	FI	VFI	VI	FI	VFI	VI	FI	VFI
1	44.9	46.1	20.7	32.3	25.1	33.5	48.6	16.9	5.5
2	14.1	39.8	5.6	16.6	28.3	9.5	39.4	21.1	8.3
3	23.6	51.1	17.3	36.2	17.3	19.5	42.5	28.1	4.7
4	36.3	38.9	21.3	27.3	32.8	11.1	25.8	40.3	19.2
5	37.3	44	9.5	48.1	27.3	13.1	35.8	39.9	6.9

Vascularity indices have been adopted by other ultrasound machine manufacturers allowing comparison between different machines. A small study was performed by Bello-Muñoz[203] by acquiring power Doppler images and sampling the Circle of Willis in different five fetuses all at 20 weeks gestation using GE, Philips and Medison equipment. Where possible, settings were kept as consistent as possible between machines and the VI, FI and VFI calculated for each subject on the three different systems in order to investigate inter-equipment variation and its impact the value of VOCAL^{TM} indices. As the Circle of Willis is an obvious functional landmark, given its shape the varition by VOI choice should be minimal.

The results, summarized in table 5.1, show how different the recorded vascular indices are depending on the system used. Variance between these measurements will be influenced not only by the scanner used by small deviations in setting, the operator error in outlining the same anatomical landmark despite the same gestational age and similar maternal characteristics. The lack of homogeneity in the results of these indices

that are considered to be representative of the same measurement of vascularity shows that currently these indices do not represent a reliable quantification method for 3D PD.

For these reasons, when measuring the placental function of the cohort of women recruited as part of the Spiral 3D study we considered extending the existing FMBV method to 3D which is an original contribution of this thesis. We hypothesis that this method should provide a more reliable measurement of fractional vascularity than the VOCAL^{TM} method. However, in order to provide as robust a measurement as possible we need to minimise the contribution of other sources of variance to the measurement of vascularity in a placenta. The next section illustrates these potential error sources and considers how best to reduce their influence.

5.2 Sources of Variance

Different factors have impact upon the estimated value of blood flow when using power Doppler ultrasound. Machine settings, tissue attenuation, maternal/fetal movement, angle of insonation and flow velocity all contribute to possible error/variation in measurement of Doppler signal[204]. Minimising the impact of these influences is therefore key to producing a reliable measure of function of the placenta. The placenta presents its own particular challenges to measurement. Firstly, it is a site of nutritional exchange between two blood systems which have different rheological properties. Secondly, the position of the organ upon the uterine wall and so its respective position to the transducer varies between different mothers and varies over pregnancy. Doppler ultrasound is inherently angle dependent and a time averaged estimate of flow. Using 3D measurement acquisition times is increased further contributing to error. This leads to a long

list of sources of variance. We consider the impact of machine settings and present in particular ways to manage the setting of gain and highlight the necessity to separate placental measurement so that only a single circulatory system is investigated at a time.

5.2.1 Ultrasound Machine Settings

Parameters such as gain, pulse repetition frequency[196] and wall motion filter are determined by operator-dependent setting[183] in order to avoid the introduction of PD artifacts that are not representative of true vascularity. For clinical research studies, machine settings are kept as consistent as possible to provide an as equal as possible comparison between scans taken of different patients or time-points as possible.

However, there are some settings that require customisation at scan-time, in particular Doppler gain. Early researchers in the field advocated using a gain setting adjusted for the individual patient to compensate for the variation in the distance from a given ROI and the transducer head. Variability between patients will result in the different distances and attenuative effect effecting the vascular values at a particular ROI. Resultantly, not adjusting the level of gain will lead to an introduction of noise or dampening of the signal returned. In a number of recent studies, uniformity of machine settings were adopted including power Doppler gain where in all were set to a fixed value[91,205–207]. Worryingly, a number of studies did not state any of their settings beyond a handful as recommended in the manufacturers' manual which would make reproduction of their results very difficult[89,208–211]. In[199] to illustrate the impact of gain, a simple flow-free study was used to investigate the relationship between gain and VOCAL^{TM} vascular indices as shown in figure 5.3. The logistic function illustrated shows the impact even a minor alteration in gain can have upon these indices.

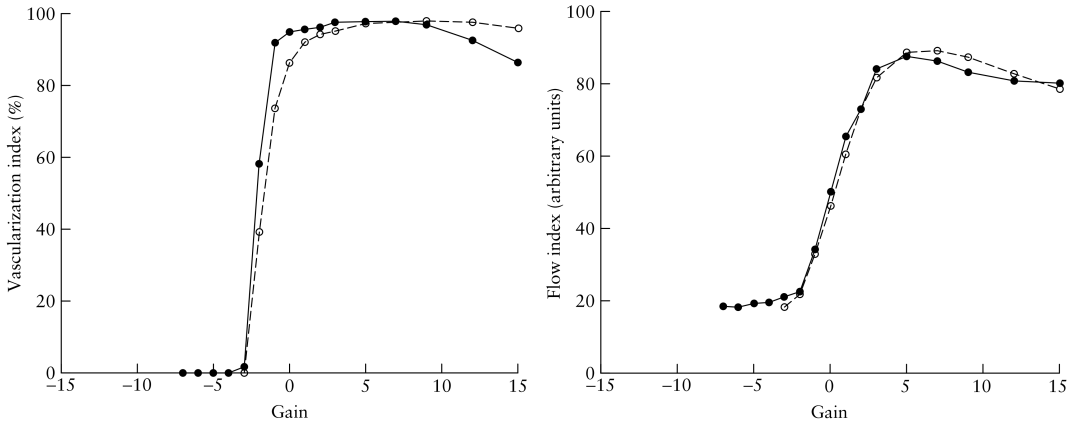

Figure 5.3: Comparison of VOCAL^{TM} indices to changes in gain in a flow-free phantom. Figure 5.3a shows the vascularisation index (VI) compared to changes in gain, figure 5.3b shows the change with respect to the flow index (FI). Pulse repetition frequencies of 0.1 kHz (•) and 7.5kHz (○) are shown. Reproduced with permission from Schulten-Wijman et al. [199]

Whilst phantom modelling has shown the impact of different machine settings upon the appearance of the PD signal [199,200] the exact nature of this influence *in vivo* is still unknown. Given the impact of gain upon any Doppler appearance the estimation of the best gain setting we investigated in collaboration with clinicians using data from the Spiral 3D study to investigate the impact of gain in an *in vivo* environment [1]. We proposed the use of a subject as her own control by keeping all other factors constant and only altering the gain level so that the influence of the gain upon VOCAL^{TM} indices could be studied for that participant.

Data was acquired using a variety of gain settings at arbitrary levels and another customised method of gain setting based upon early studies using power Doppler [87,213]. Customised gain setting was obtained by a simple procedure described in Rubin et

[1] This work was produced collaboratively. Data acquisition, measurement and statistical analysis was performed by Sally Collins and Alec Welsh. The author contributed to the experiment design and methodology. See the accepted journal article [212] for more details.

al.[87] as follows. The gain level was increased in real-time acquisition until obvious artefactual noise became present at the insonation target. By then slowly reducing it to a level just below this threshold (i.e. to where the noise artefact just disappears) an individual, customised "sub-noise gain (SNG)" level was found.

To avoid introduction of any other confounding factors due to pathology, only women with a normal pregnancy outcome were included in this study. Normal pregnancy outcome was defined as: uncomplicated live birth after 37 completed weeks gestation; customised birth weight $\geq 10^{\text{th}}$ centile; no admission to the neonatal intensive care unit (NICU); no evidence of maternal hypertensive disorders, gestational diabetes or other significant pregnancy related maternal morbidity. Fifty-two women matched these criteria and of these, two were found to have at least one suboptimal image in their set of five and were excluded. Therefore, data from 50 women were included in the final analysis.

Five anatomically identical static 3D power Doppler volumes of the placenta were acquired using a set machine configuration (described fully in Appendix C). With placenta position acquired and viablity confirmed, without moving transduction position, five sweeps were performed in serial altering only the PD gain setting. The gains recorded were -9.0dB, -7.0dB, -5.0bB, -3.0dB and the SNG. The data was then stored using Sonoview (GE Medical Systems, Kretztechnik, Austria) and analysed off-line using 4D View$^{\text{TM}}$ (GE Healthcare, Milwaukee, WI, USA) and the VOCAL$^{\text{TM}}$ tool. Each static volume was opened and analysed without any image manipulation. The maximum sized sphere allowed by VOCAL$^{\text{TM}}$ was used using 6° rotational steps centred upon the reference image (as shown in Figure 5.4). The observer checked that there was no movement between volume acquisitions, in which case they were rejected.

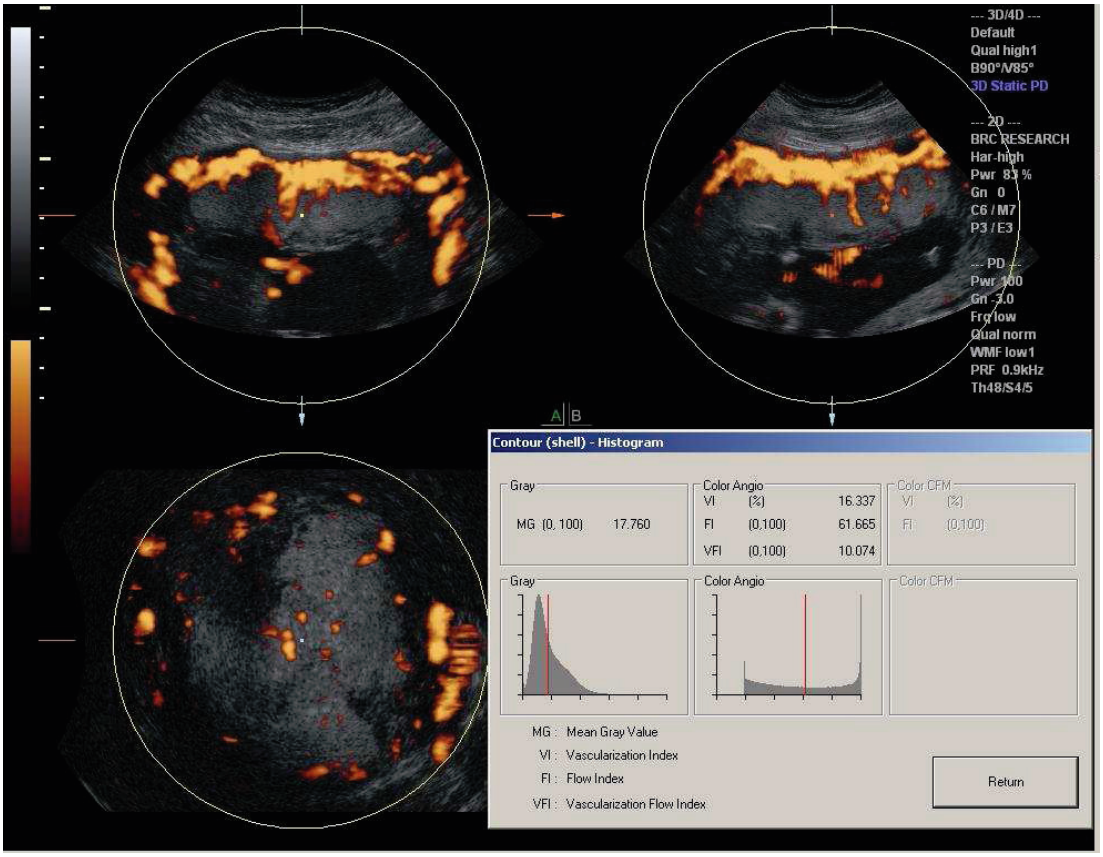

Figure 5.4: Illustration of sphere used to capture identical regions of interest at varying gain settings. The figure shows the capture of the maximum sphere radius encompassing the whole placenta.

This step was performed to minimise the introduction of any potential sampling errors introduced by sampling different sized vessels. Values for VI, FI and VFI were then recorded.

Absolute values of the indices recorded should be different for each participant due to biological variation, adequacy of placentation and the maturity of the placental vasculature. We therefore proposed to investigate the difference between the individualised SNG compared to the arbitrary gain levels recorded in the four other scans. The percentage difference from this absolute value was calculated for all the other gain settings and then plotted against the absolute difference in gain value (e.g. if SNG setting

Table 5.2: Results of simple linear regression analysis comparing difference in vascularization index, flow index and vascularization flow index with difference in gain setting below and above the sub-noise gain (SNG) value.

	R^2 value	P
Gain settings below SNG value		
Vascularization index	0.68	< 0.0001
Flow index	0.01	0.31
Vascularization flow index	0.72	< 0.0001
Gain settings above SNG value *		
Vascularization index	0.79	< 0.0001
Flow index	0.02	0.39
Vascularization flow index	0.79	< 0.0001

* Including noise artifact.

was -2 and the VI at the SNG=100 and VI at a gain of -5=75, the percentage difference was -25% and the absolute difference in gain value was -3). Figures 5.5 show the absolute difference in gain compared to percentage change in each of the the three indices.

The relationship between the percentage value and the absolute difference in the gain value from the SNG value was explored using linear regression analysis. To test the difference in the gradients between the lines above and below the SNG we proposed a null hypothesis that the gradient of the line above was equal to the gradient of the line below. It can be shown that this hypothesis follows a t-distribution and therefore it was appropriate to test with the Student t-test. Statistical analyses were performed using SPSS (version 16.0, IBM Corporation, NY, USA) & Excel 2004 (Microsoft Corp., Washington, USA). Results were considered to be statistically significant when $p<0.05$.

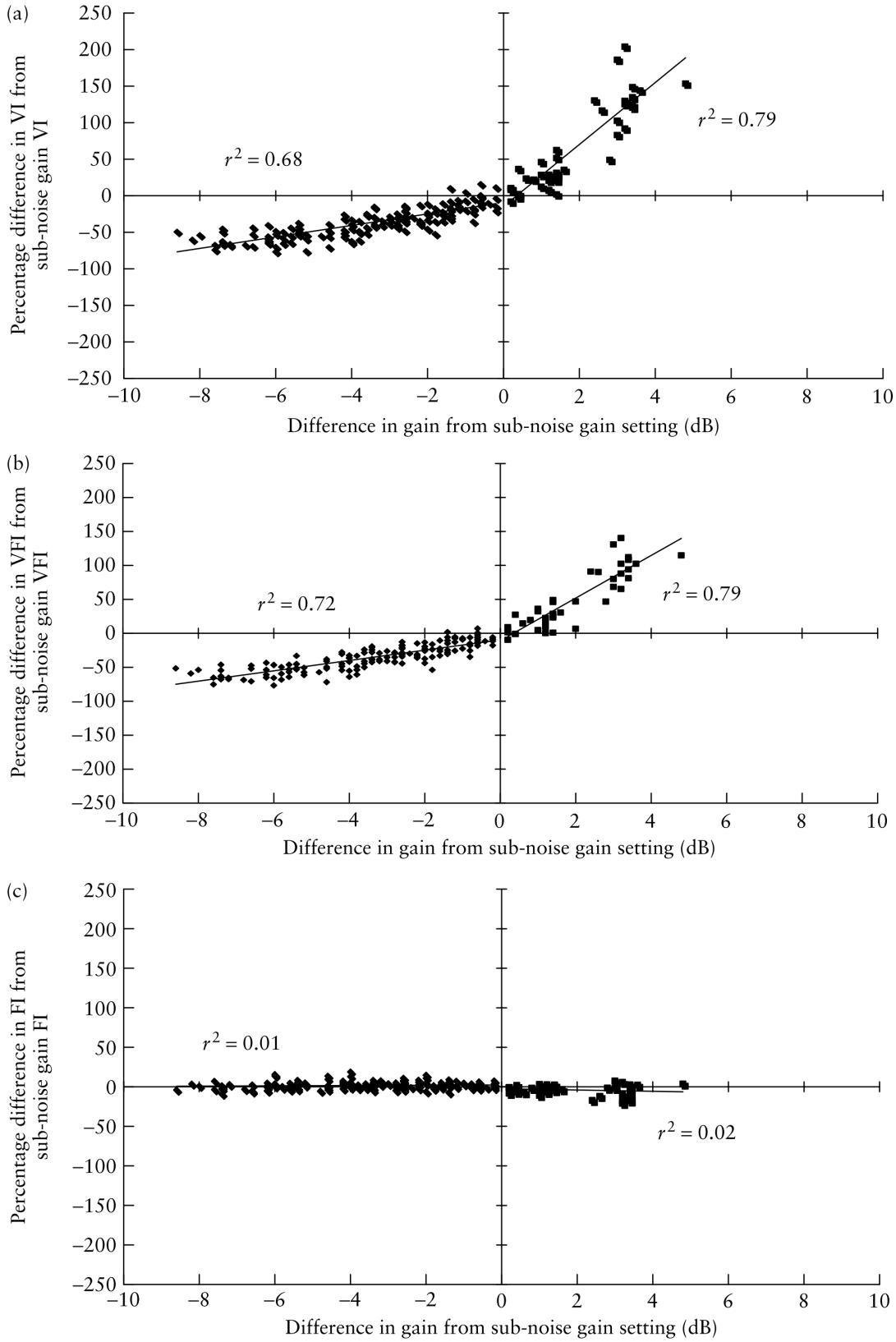

Figure 5.5: The effect of changing the PD gain on VOCAL™ indices. The zero mark indicates the individualised sub-noise gain setting. The percentage difference between SNG setting and respective VOCAL™ index, VI (top), VFI (middle) and FI (bottom) are shown against difference in gain measured in decibels (dB).

Linear regression analysis showed that the percentage difference in VI, and consequently VFI, were significantly linearly related to the difference in gain setting from the SNG value (Figure 5.5). Whilst the relationships above and below the SNG point are both linear their gradients are significantly different ($p<0.001$). Above the SNG point the slope is steeper as the noise artefact appears. No such relationship was demonstrated for FI when the gain was changed (Figure 5.5).

The linear relationship of the PD gain to the VI value indicates that gain directly affects the calculated value of the VI, so this has to raise further questions about the interpretation of these indices which are based upon Doppler appearance. As the gain setting is dropped below the SNG point, the value calculated for VI decreases proportionately as Doppler information is lost. Above the SNG point a significantly different linear relationship is seen, with a steeper slope as the image (rapidly) becomes disrupted by noise artefact. This study suggests that the use of a SNG optimises the information gained for each subject.

The previously documented suggestion that the gain should be set "somewhere in the middle of the range"[200] and kept constant for all subjects may actually result in information being lost for some subjects with artefacts being introduced in others due to differences in signal attenuation from the beam path. Possibly, this could result in the introduction of errors into the calculated VI & VFI values. This protocol was initially developed to collect 3D volumes with gain settings between -3 and -9dB. These values were arbitrary and selected as this was anticipated to be the most likely range for the study population.

This PD gain evaluation has several limitations. It is relatively small in size but as the effective size was unknown in advance a power calculation could not be performed. However, as all the statistical tests have demonstrated a very high level of

significance ($p<0.001$), n = 50 was sufficient. The fixed gain levels of -3.0, -5.0, -7.0, and -9.0 dB were arbitrarily selected. It may have been better if more gains had been evaluated (possibly including 0 and +3, a Voluson® E8 has a gain range of -15dB to 15dB). However, taking a sequence of five volumes in exactly the same place on the abdomen without the operator or participant moving at all was difficult. Therefore, pragmatically, a series of five was selected.

In conclusion, this work demonstrates that use of SNG is an important step in optimising 3D PD imaging and one that has be used in order to provide the best minimisation of error due to gain control. As such it should be adopted for any quantification of the placental vasculature.

5.2.2 Differences in Feto/Maternal Circulation

In investigating placental blood flow any researcher must be aware of the impact of measurement of the different circulatory systems for a number of reasons. The oxygen carrying protein within any red blood cell (RBC) is haemoglobin which differs in type between fetus and mother[214,215]. The proportion of RBCs carried as a proportion of the circulating volume (haematocrit) within the fetus is also different compared to the mother[215]. Recent studies have shown in the premature neonate, from 22 weeks to 40 weeks gestation that haematocrit[216] and haemoglobin[217] concentration increases over gestational age whilst the mean corpuscle (RBC) volume decreases[217].

The importance of this is down to the influence of haematocrit percentage upon the power of backscattered ultrasound signal[218,219] which will effect Doppler appearance. These three different observations (haematocritic proportion and haemoglobin concentration increase with mean RBC volume decrease) in the pre-term neonate introduce a

further source of variation in the underlying Doppler scatters in the fetal circulation. There also remains another issue of the aggregation of red blood cells. Rheologically active blood proteins on the eythrocytes causes aggregation of the blood cells, forming rouleaux (columnar stacks of cells) when travelling at low velocity. This has the effect of increasing the effective size of some of the scatterers thereby altering the reflective properties and the back-scattered PD signal[185]. Compared to maternal blood, fetal blood has relatively less fibrinogen making it less likely to develop rouleaux[220,221]. Previous PD studies have demonstrated that this produces a homogeneity of scatterers not seen in adult blood flow[189]. Evaluation of the placenta will introduce variance from two different circulations with their individual biases. It is therefore advisable to investigate a single system in isolation.

5.3 Conclusion

Quantitative measurement of 3D PD ultrasound has been shown to require rigourous experimental design to avoid the impact of any different sources of error when acquiring ultrasound data. We have reviewed current methods of measurement and have suggested that extending the FMBV method into 3D in order to provide a depth-compensatory effect to improve estimation of vascularity. Hurdles to robust estimation of flow remain. Appropriate use of machine settings and in the case of the placenta isolation of one of the circulatory systems is required. We have shown experimentally that with the use of the sub-noise gain, a method to customise gain for each subject optimises the information gained for each subject. In the next chapter, we will develop a framework from which to provide, for the first time, 3D FMBV measurement of the utero-placental interface.

Chapter 6

Three Dimensional Fractional Moving Blood Volume (FMBV) Estimation of Placental Blood Flow

In order to overcome the obstacles to reliable Doppler estimation of placental vascularity outlined in chapter 5 we now propose a new 3D approach using fractional moving blood volume (FMBV) estimation. This chapter will describe this contribution, outlining the methodology of our image processing driven technique and demonstrating its application on placental volume data acquired as part of the Spiral 3D study described in Chapter 3. By coupling the volumetric results with aspects of the visualisation work of Chapter 4 we propose a simple methodology to provide quantifiable samples of the utero-placental interface (UPI). With these samples identified and extracted, measurement of them can be performed using the metrics outlined in chapter 5. This allows us for the first time, to measure both the UPI disassociated from other areas of anatomy and investigate the impact of different quantification methods.

The impact of organ position, haemodynamic differences between mother and baby, machine settings and other variances require an innovative design of experiment to capture a 3D sample of the placenta not hindered by these variances. Our main contribution of this chapter is to use FMBV estimation upon a subsample of the 3D volume that represents the maternal vessels proximal to the placenta and a portion of the placenta on the maternal side. This allows us to measure a tissue sample either within the placenta or in the maternal vasculature that contains only maternal blood and using a depth compensatory method to maximise the information investigated.

We measure discrete volumes of interest whose dimensions are selected based upon observations of Doppler flow in 2D. We also extract measures of vascularity such as MPI, FMBV and the VOCAL^{TM} indices described in section 5.1.2 and investigate potential agreement or variance between these estimators of vascularity. Other factors such as placental position are also investigated along with maternal BMI to establish if there are any correlations between these other potential factors of influence.

6.1 Methods

3D ultrasound scans were acquired from 143 women between 11-13+6 weeks gestation using a GE Voluson E8 (GE Healthcare, Milwaukee,WI,USA) as part of the 'Spiral 3D' study (REC reference number: 08/H0604/163). 3D PD scans were acquired using the settings as described in appendix C including the sub-noise gain as discussed in Chapter 5. For each subject, the placenta was segmented off-line using the Random Walker algorithm as described in Chapter 3 and the utero-placental interface (UPI) extracted using the technique outlined in the Chapter 4. With the UPI segmented, the

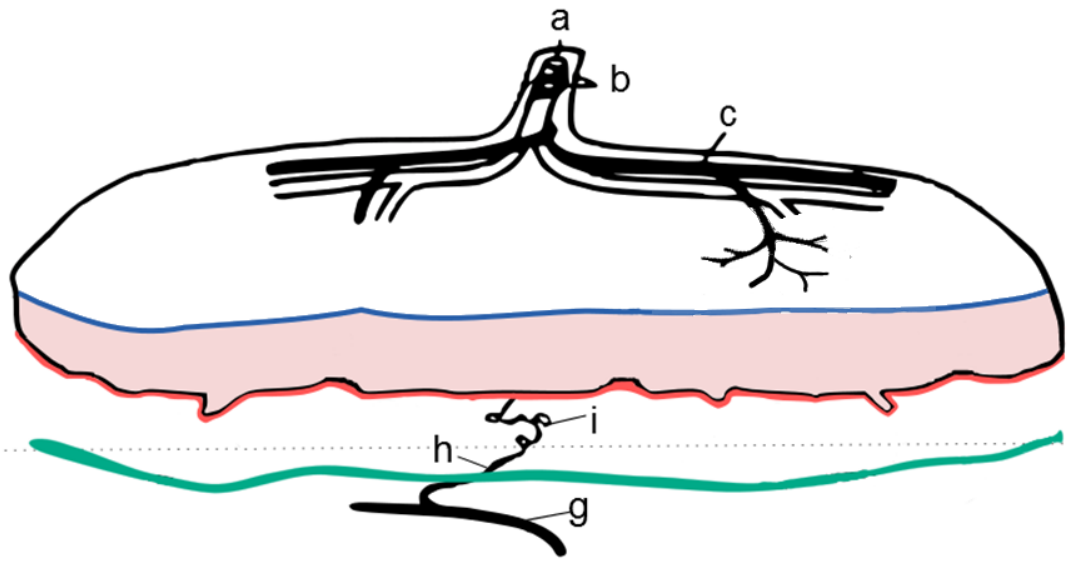

Figure 6.1: Placental schematic diagram and sampling areas for FMBV estimation. Pink area = target ROI; red contour = UPI; green contour = reference VOI. Anatomical parts - a, umbilical arteries; b, umbilical vein; c, surface vessel; g, radial artery; h, arcuate artery. Dotted line represents division between decidua and myometrium. Adapted with permission from Pretorius et al.[179]

technique we use to produce our "stack of surfaces" that are viewed as serial discs is adapted to provide vascular samples at discrete areas within and outside of the placenta, without parameterisation. Resultantly, measurements of vascularity can be performed within, outside and on the border of the placenta with the knowledge of the geometric distance from the UPI.

2D colour Doppler measurements of spurts of blood entering the intervillous space were measured by Dr Sally Collins as part of her DPhil studies as an estimation of the level of ingress of blood flow from the distal end of the spiral arteriole into the intervillous space[212]. 52 subjects had at least one spurt measured (an illustration of the method is shown in Figure 2.9d) with a maximum of three measurements made upon those "jets" of blood flow considered qualitatively the largest. 141 lengths were measured providing a mean spurt length of 2.76mm (min. 0.9mm, max. 7.3mm, σ 1.21mm).

Assuming that the presence of blood flow appears relatively similiar between a 2D colour Doppler acquisition and a 3D power Doppler sweep which provides a sample of most of blood flow into the placenta.

Given these distances as a basis to sample target and reference VOIs respectively the masking process and distance transform performed in section 4.3 defined a simple method to extract the VOIs automatically and return scalar values for FMBV calculation. Figure 6.3b shows discrete surfaces at regular intervals from the UPI to the reference VOI as described in the schematic in Figure 6.1. The areas of interest that were measured were as follows:

1. The 0.0 values of the EDT - the utero-placental interface.
2. 3.0mm to -3.0mm - a sample of 6mm across the UPI.
3. 6.0mm to -6.0mm - a sample of 10mm across the UPI.
4. 0.0mm to -5.0mm - a sample from the UPI to 5mm into the placenta.
5. 0.0mm to 5.0mm - a sample from the UPI out into the uterus.

As explained in Chapter 5, use of the FMBV technique requires a reference vessel such as a fetal aorta[189] or hepatic artery where regular, high amounts of blood flow can be sampled consistantly. In the placenta, a reference vessel is a challenging problem to find as consistent, automatic detection of such a vessel is a hard problem. Typical vessels in the area would be the uterine arteries or the cord insertion of the umbilical artery. However, both of these prove problematic. Position, of the uterine arteries relative to the placenta is variable from subject to subject whilst the umbilical cord is part of the fetal circulation. Regions of interest within the placenta must also be

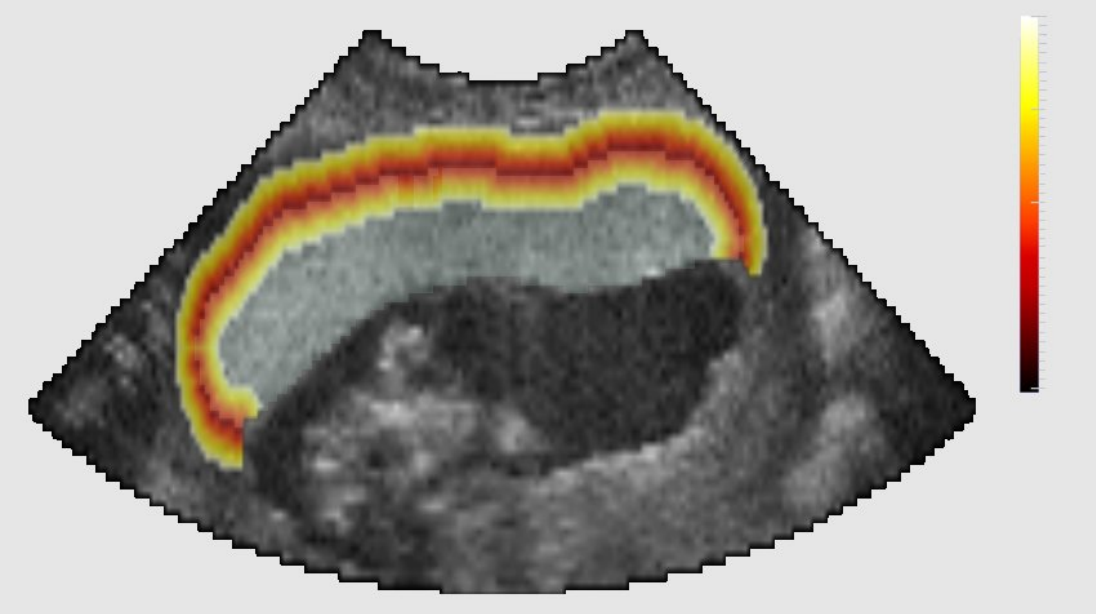

Figure 6.2: Illustration of discrete surfaces measured on uterine and placental side of the utero-placental interface (UPI). Colour map corresponds to distances from 0mm to 5mm away from UPI.

discounted as a point of reference reflective of 100% blood flow can only be found within the maternal vessels of the uterus.

We propose using the plexus of arcuate and radial arterioles shown in Figure 6.1 that provide a conduit of supply from the uterine arteries to the spiral arterioles as a reference point from which to perform standardisation. They should provide a more consistent position than the iliac or uterine arteries due to their closer proximity to the basal plate. This makes them a more attractive anatomical reference point than other vessels whose position is more ambiguous. Although they are intermediary vessels, radiographic studies have shown that these arterioles although not invaded by trophoblasts expand in bore throughout pregnancy and are twice in diameter than the upstream uterine vessels by mid pregnancy[222].

6.1.1 Reference Vessel Determination

By comparing the standardisation values between the proposed reference VOI and a VOI outlining an area of known maximal vascularity we can compare the calculated standardisation values and investigate if they are consistent. Either of the maternal uterine arteries represents such a vessel, and by manually extracting a VOI of the vessel the normalisation value from that can be compared to that obtained from the plexus in the same subject and volume.

19 subjects with anterior placentas and a uterine artery that apparent at the same level as the reference VOI were used. The uterine artery was extracted using a $10 \times 10 \times 10$ voxel size VOI. Normality of the two distributions of standardisation values was investigated using the Shapiro-Wilks test and the non-parametric Wilcoxon signed-rank test was used to measure if the paired differences between the two groups of standardisation values were different.

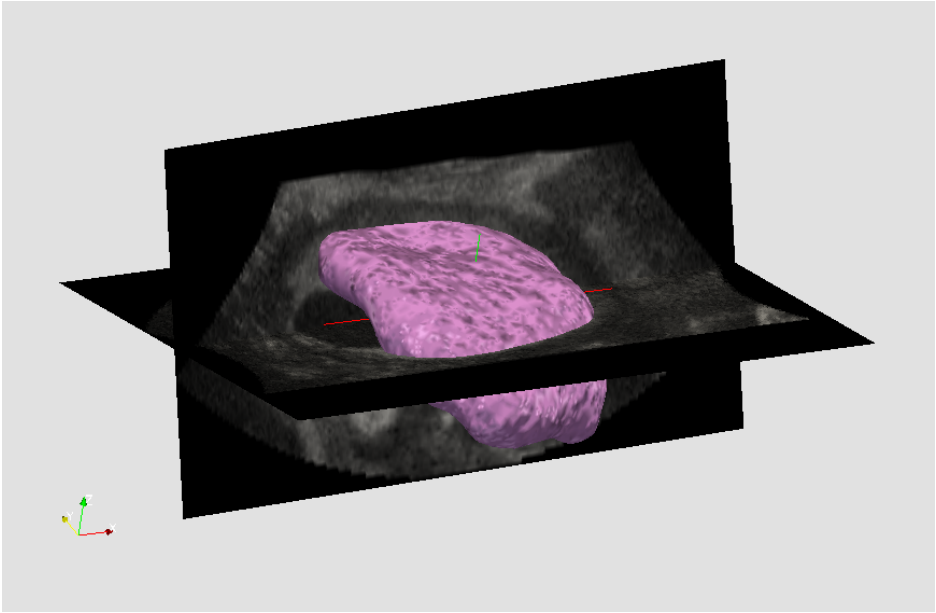

(a)

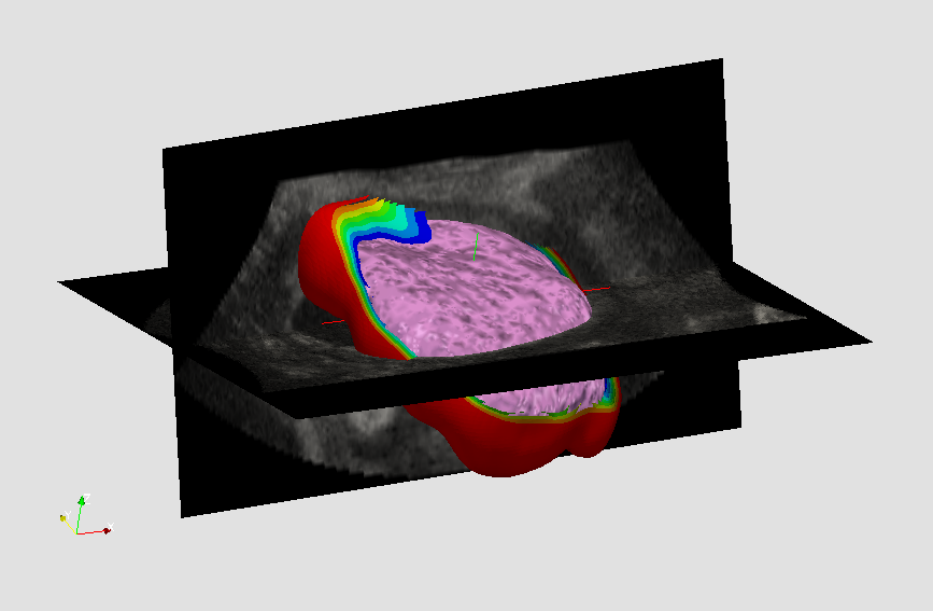

(b)

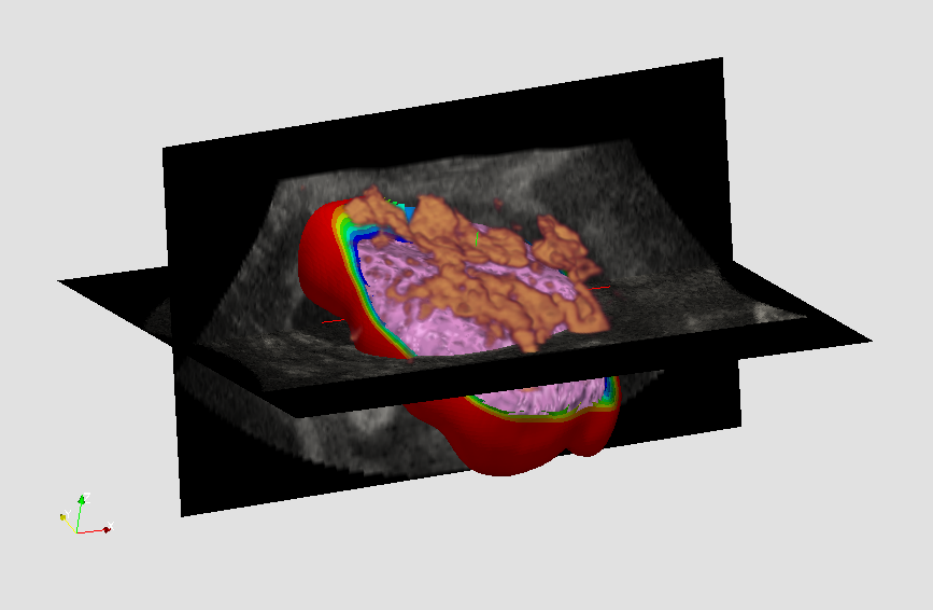

(c)

Figure 6.3: Illustration of discrete VOIs in maternal tissue colour mapped by distance away from placental surface. Utero-placental interface is shown in (pink).Figure 6.3a shows UPI alone, Figure 6.3b shows the discrete surfaces of interest and Figure 6.3c shows the Doppler signal (overlaid as orange) illustrating the plexus of blood flow supplying the placenta.

By extraction of the respective Doppler values at these surfaces either we can then investigate specific anatomical areas or compare the metrics recorded that represent their vascularisation. The values are passed into the FMBV calculation algorithm as described in Rubin et al.[184] which was implemented in Python™ (version 2.7.2) using the `matplotlib`[223] and `numpy`[224] libraries distributed as part of the Python(x,y) project[225]. Along with this measure, the VOCAL™ indices of vascularity and mean pixel intensity (MPI) were estimated. For comparision between FI and MPI, the mean pixel intensity was calculated as the percentage average of the voxel intensities. Differences in vascularisation between VOIs was compared using the student t-test or Mann-Whitney U test where appropriate. Normality of the distributions was tested using the Shapiro-Wilks test. With all four measures calculated and data collected at time of acquisition - such as maternal BMI, placental position and pregnancy outcome - we can investigate relationships between these measures and their variance on different subsets of the study population. Firstly, measurement comparison will investigate the differences between using existing 3D indice measures and the new implemented measurements. Secondly, by investigation of our measurement results relative to placental position and maternal BMI we wish to investigate if any measurement is influenced by factors that can be considered to be indicative of potential attenutative differences. Finally, we will examine if 3D Doppler measurement of the placenta in early pregnancy can provide a correlative link to pregnancy outcome.

Table 6.1: Results for 3D PD measurements taken for all Spiral 3D subjects at different volumes of interest (VOIs)

	Subjects and measurements taken ($\mu \pm \sigma$) All subjects (n = 143)			
Volume Of Interest (VOI)	FMBV	VI	FI	MPI
6mm $\leftrightarrow$ UPI	20.60 ± 11.03	20.11 ± 6.72	59.53 ± 8.34	60.61 ± 9.21
10mm $\leftrightarrow$ UPI	17.94 ± 9.91	17.18 ± 5.94	58.85 ± 8.10	59.85 ± 8.86
UPI	24.81 ± 13.10	22.64 ± 8.36	58.82 ± 13.23	59.96 ± 14.03
5mm UPI $\rightarrow$ Placenta	11.74 ± 9.28	3.97 ± 1.61	56.42 ± 3.14	56.89 ± 3.77
5mm UPI $\rightarrow$ Uterine	19.02 ± 10.94	14.85 ± 5.31	58.41 ± 8.05	59.35 ± 8.79
	AGA subjects (n = 123)			
	FMBV	VI	FI	MPI
6mm $\leftrightarrow$ UPI	21.39 ± 10.68	20.97 ± 5.77	60.77 ± 4.16	61.91 ± 5.38
10mm $\leftrightarrow$ UPI	17.94 ± 9.91	17.18 ± 5.94	58.85 ± 8.10	59.85 ± 8.86
UPI	25.71 ± 12.56	24.30 ± 6.33	61.99 ± 4.42	63.21 ± 5.73
5mm UPI $\rightarrow$ Placenta	12.28 ± 9.08	4.09 ± 1.58	56.73 ± 2.95	57.22 ± 3.57
5mm UPI $\rightarrow$ Uterine	19.77 ± 11.03	15.52 ± 4.67	59.60 ± 3.82	60.59 ± 4.92
	SGA subjects (n =20)			
	FMBV	VI	FI	MPI
6mm $\leftrightarrow$ UPI	15.72 ± 12.16	16.91 ± 8.35	57.94 ± 5.03	58.81 ± 7.10
10mm $\leftrightarrow$ UPI	13.54 ± 10.23	14.28 ± 7.26	57.53 ± 4.81	58.34 ± 6.57
UPI	19.27 ± 15.22	19.76 ± 9.50	61.99 ± 5.88	63.21 ± 8.36
5mm UPI $\rightarrow$ Placenta	8.43 ± 10.00	3.24 ± 1.61	54.53 ± 3.65	54.85 ± 4.38
5mm UPI $\rightarrow$ Uterine	14.43 ± 9.41	12.32 ± 6.37	57.06 ± 4.73	57.80 ± 6.43

* $\leftrightarrow$ - indicates VOI spans across the UPI. $\rightarrow$ - VOI between UPI and uterus or placenta

6.2 Results

Table 6.1 displays the measurements taken from the volumes of interest listed in the previous section. Measurements of FMBV, VI, FI and VFI are tabulated for each volume of interest. The FMBV and VI as outlined previously estimate total vascularity whilst the FI and MPI are representative of the mean intensity values of coloured voxels. Results for all 143 subjects are presented as well as cohorts whose pregnancy outcome was determined as appropriate for gestational age (AGA) (n = 123) and small-for-gestational age (SGA) (n = 20). Acquistion methodology and the definitions of AGA and SGA are as stated in section 3.4.1 as used in the clinical work on 3D placental volume in chapter 3.

6.2.1 Reference Vessel Determination

There were no significant differences between standardisation values calculated from the subset of 19 subjects whose uterine artery was used to calculated FMBV and compared to the FMBV calculation used for the reference VOI. As a result, we can consider that the plexus of vessels at this geometric distance contains the appropriate maximal intensity signal equivalent to a uterine artery.

6.2.2 Measurement Comparison

Comparison between measures estimating the proportion of vascularity (FMBV and VI) and the intensity of signal (FI and MPI) in different anatomical VOIs were investigated. Figures 6.4 - 6.8 show Bland-Altman plots for visualising the differences between two measures. For each volume of interest the differences in measures for proportion of vascularity and mean intensity of vascularity are shown. Each figure

shows a consistent trend across all VOIs. Where the average of the measurements lies below the mean of both measures the difference is negative or near zero, indicating that FMBV and MPI return lower measurements compared to the respective measurements based on VOCAL^{TM} indices. In Figures 6.7 and 6.8 the same pattern of differences versus mean measurement is observed despite the range of values being double the size for the uterine measurements as compared to the placental. For larger mean values, a trend is observed where the VOCAL^{TM} indices produced increasingly larger results when compared to the FMBV or MPI values. For all VOIs these trends follow in a similar pattern. As the vascularity and average intensity increase in value, the pattern reverses but the deviation in measurement as shown in all the plots is much larger. It should be noted that the bias between the FMBV and VI is much larger than the average intensity measures, as shown by the much tighter limits of agreement. Additionally, the difference between the measurements taken on the uterine and placental side of the UPI where compared using both FMBV and VI. By Mann-Whitney U test, significantly less blood flow was found on the uterine side of the placenta when compared to the interior of the placenta.($p < 0.05$) using both VI and FMBV to estimate vascularity.

6.2.3 Placental Position

At scan time, the position of the placenta relative to which uterine wall the placenta was attached was recorded. Positions were recorded as anterior, posterior lateral, fundal or previal; where a placenta adhered to two walls the wall in which the majority of the placenta was attached was used to describe its position. Fundal and previa placenta were excluded from measurement as their position could not be considered as consistent

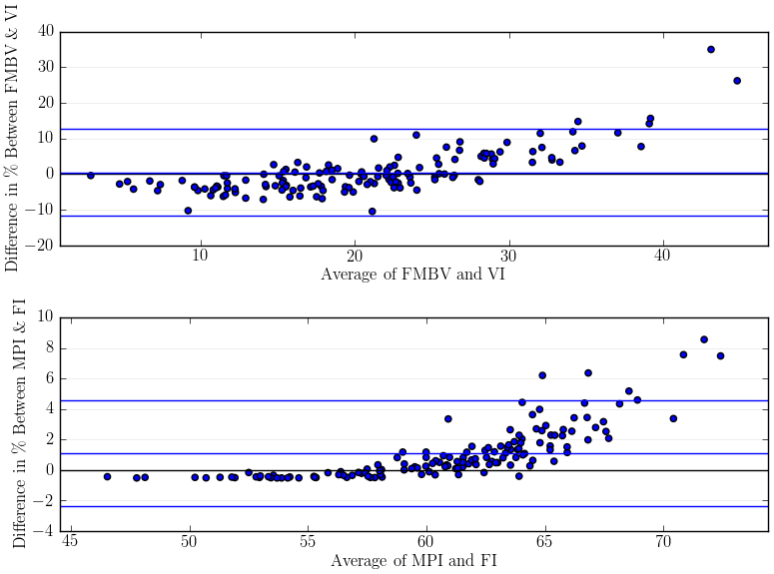

Figure 6.4: Bland Altman plots comparing estimates of vascularity, FMBV and VI, (top) and mean intensity, MPI and FI, (bottom) taken from VOI 10mm across the UPI. Top - Mean difference 0.46, limits of agreement (LOA) (12.62,-11.70). Bottom - Mean difference 1.10, LOA (4.59,-2.39).

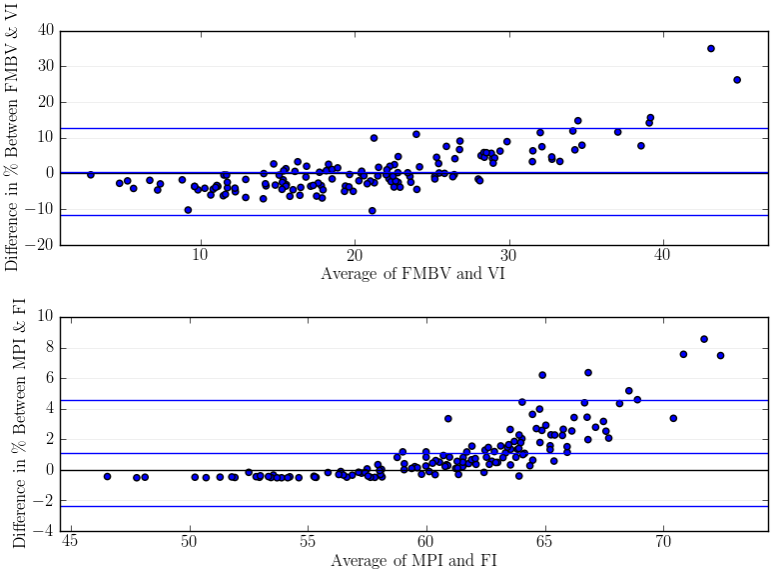

Figure 6.5: Bland Altman plots comparing estimates of vascularity, FMBV and VI, (top) and mean intensity, MPI and FI, (bottom) taken from VOI 6mm across the UPI. Top - Mean difference 0.74, limits of agreement (LOA) (11.84,-10.36). Bottom - Mean difference 1.02, LOA (4.17,-2.14).

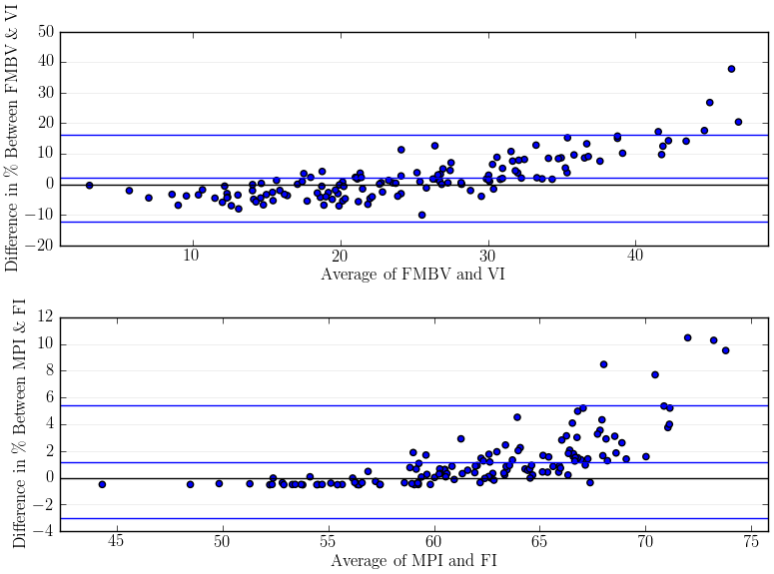

Figure 6.6: Bland Altman plots comparing estimates of vascularity, FMBV and VI, (top) and mean intensity, MPI and FI, (bottom) taken from the UPI. Top - Mean difference 2.02, limits of agreement (LOA) (-12.19,16.23). Bottom - Mean difference 1.20, LOA (-3.00,5.39).

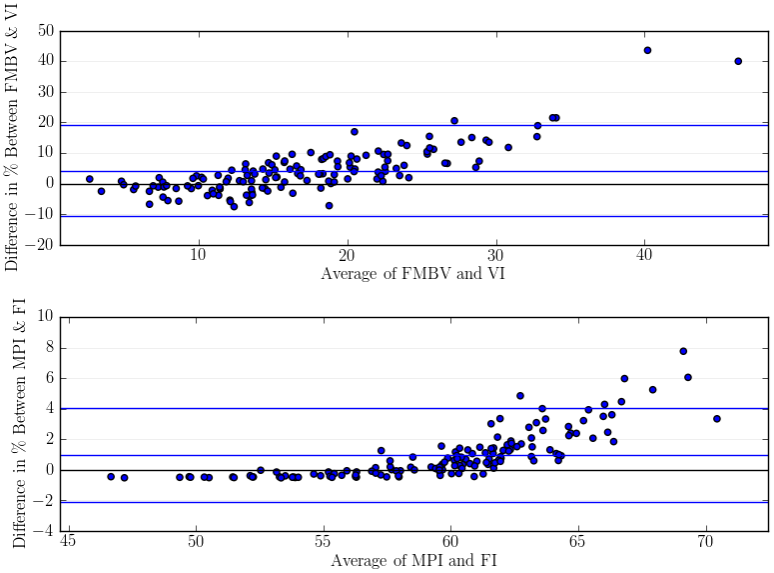

Figure 6.7: Bland Altman plots comparing estimates of vascularity, FMBV and VI, (top) and mean intensity, MPI and FI, (bottom) taken from the UPI 5mm into the uterus. Top - Mean difference 7.88, limits of agreement (LOA) (-9.28,25.03). Bottom - Mean difference 0.47, LOA (-1.20,2.14).

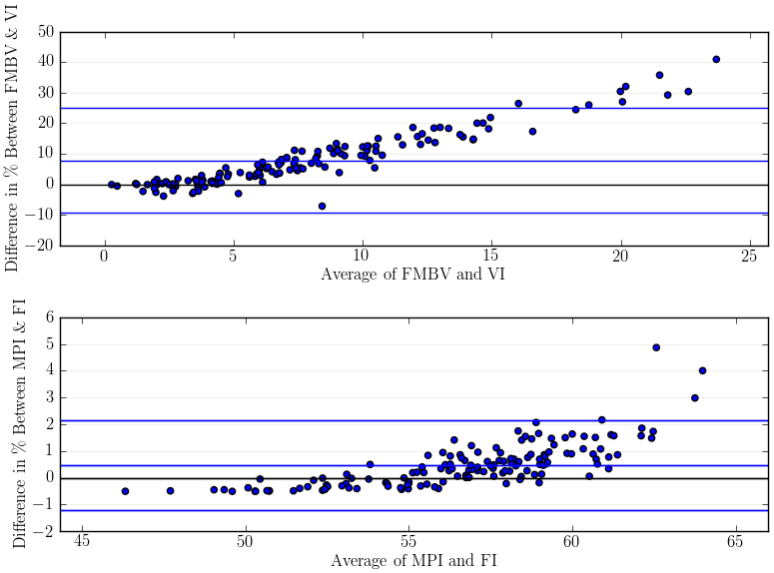

Figure 6.8: Bland Altman plots comparing estimates of vascularity, FMBV and VI, (top) and mean intensity, MPI and FI, (bottom) taken from the UPI 5mm into the placenta. Top - Mean difference 4.17, limits of agreement (LOA) (-10.67,19.02). Bottom - Mean difference 0.95, LOA (-2.11,4.02).

when compared to the other three groups. Of the 120 subjects that made up the remaining three groups 63 had a posterior placenta, 50 anterior and 17 lateral. Figure 6.9 shows the difference in measurement values for the VOI defined as from the UPI 5mm into the placenta across these placental groups. The measures were then tested statistically to determine if their distributions differ. The non-parametric Kruskal-Wallis one-way analysis of variance was used as no set of group were determined as having all being normally distributed under testing using the Shapiro-Wilks test. No significant differences between distributions was observered between any measurements, in any of the five VOIs ($p > 0.05$).

6.2.4 Predictive Power [1]

With pregnancy outcome recorded as either AGA or SGA as defined by customised birth-weight centile, the 3D vascularity and intensity measures were compared against this measure. As when investigating the impact of placental position upon the measures of vascularity all VOIs were used to investigate if significant differences between all the vascular measures could be found in the two populations of pregnancies (AGA/SGA). For the four different vascular measures each one produced statistically significantly smaller measures from the SGA group compared to the AGA group ($p<0.05$).

6.3 Conclusion

The results shown allow us to consider the impact of different sources of error and their effect upon blood flow estimation. By considering the difference in measurement of the amount of blood flow appearance and then the mean intensity as determined by two different measurements for each respectively, we have shown trends between the two irrespective of VOI investigated. In the case of low measurements of flow amount and intensity, both FMBV and MPI correlate well with VI and MPI respectively, with the FMBV and MPI underestimating when compared to the other measures. As values increase, so a positive bias is observed where VI and FI increasingly overestimate when compared to the other measurement. The similiar trend between different measures we hypothesis may be due to the weightings of voxel values based on their respective VI and FI indices as shown in equations 5.1.2 and 5.1.2, respectively.

[1] The statistical testing against the clinical population was performed by Dr. Sally Collins.

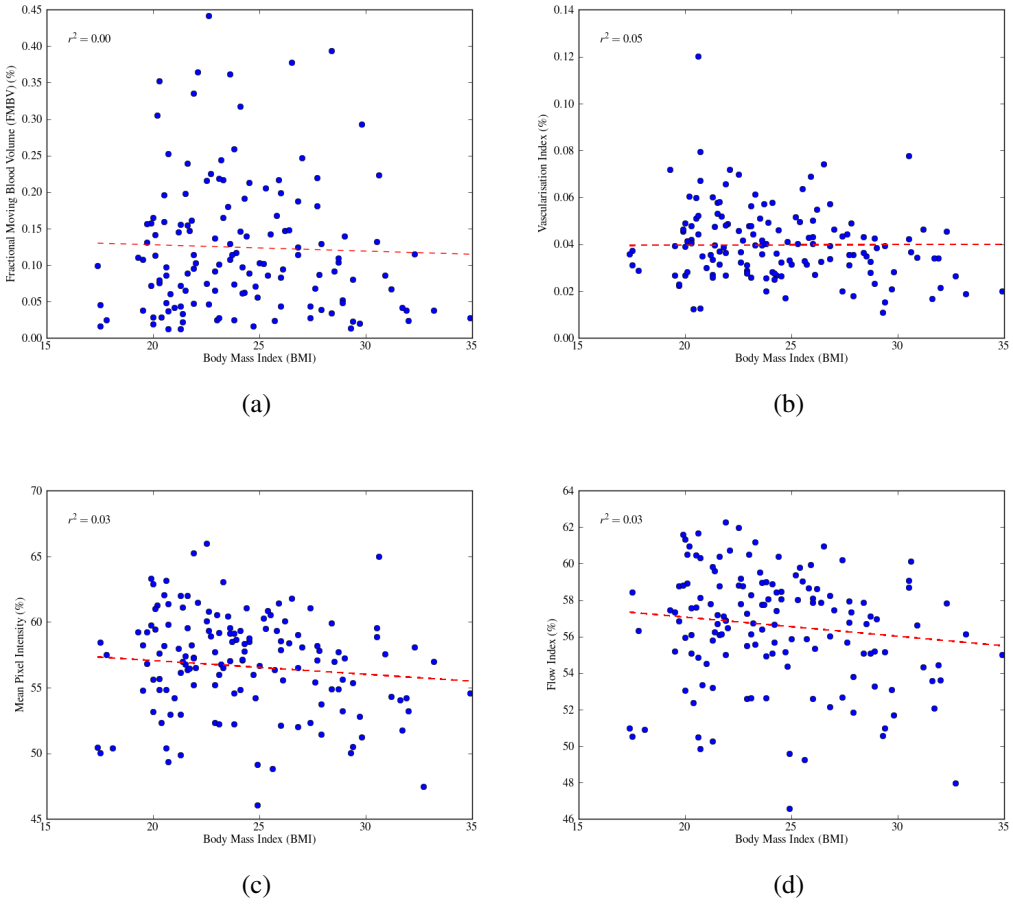

Figure 6.10: Scatter plots showing FMBV, VI, MPI and FI measurements compared to maternal BMI.

Having investigated that the same trends occur irrespective of the VOI investigated, the impact of the placenta's position relative to the transducer was considered. By subdividing the study groups based upon the uterine wall to which the placenta was attached, we showed no significant differences the distribution of any of the measurements across all the VOIs. This result shows that irrespective of standardisation by FMBV or not, there is no difference between groupings. One would consider the attenuative effect of measuring Doppler signal between an anterior and posterior placenta

to be different, for example. However, by the performance of customised adjustment of gain for each patient there would seem to be a reason behind the lack of variance in appearance between subjects. Given that all the scans were performed during early pregnancy, the variance in depth between placenta will be also be at its least, by longitudinal study of placental Doppler measures we could investigate if the distribution of groups by placental position holds or deviates over time. The results shown are further reinforced by plotting measurement values to patient body mass index (BMI) at the first scan, Figures 6.10a - 6.10d. This shows a lack of correlation between measurements and maternal BMI for all measures. Given maternal BMI is not necessarly the most accurate marker for the physical disposition of a given subject (an abdominal circumference is probably a more accurate measure in our case) then caution must be given in the interpretation of these results. They do however reinforce the results from investigating different placental positions.

Finally, estimation of blood flow intensity and proportion at and around the uteroplacental interface has shown to correlate with pregnancy outcome. This positive result reinforces the results of chapter 3 that showed placental volume was a positive imaging biomarker in the detection of poor pregnancy outcome. This chapter has shown that by moving a step further and by the use of 3D PD to investigate the specific area of the placenta known to be implicated in pathological cases we have shown significant results in both of degree and average mean intensity of vascularity. These results present an exciting development that the estimated vascularity can also provide an imaging biomarker for the SGA baby.

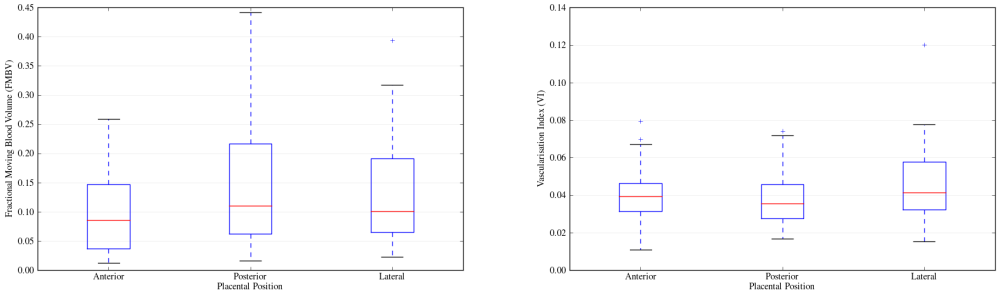

(a) FMBV

(b) VI

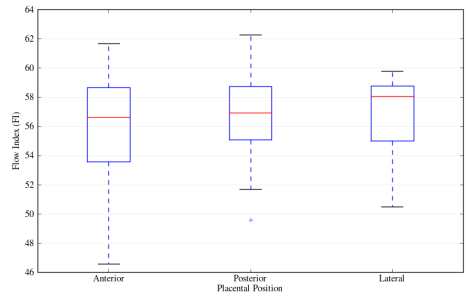

(c) FI

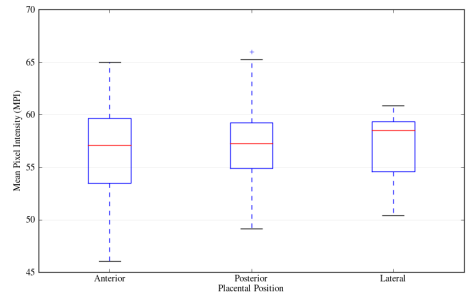

(d) MPI

Figure 6.9: Boxplots showing variances of vascularisation measures across placenta of difference positions (anterior, lateral and posterior). FMBV, VI, FI and MPI.

Chapter 7

Conclusions and Future Work

UNDERSTANDING of the relationship between the placenta and poor pregnancy outcome is still unresolved. Poor remodelling of the spiral arterioles in the first trimester leads to a failure of the utero/placental unit to supply sufficient nutritional support to the developing fetus in later pregnancy. Clinicians have considered that imaging biomarkers such as volume, and by using power Doppler ultrasound the vascularity of the placenta may reflect this pathology. However, measurement of these features requires careful acquisition and, by manual segmentation, tedious outlining of the volume of interest. The process is time consuming and is unrealistic as an approach to detect or measure potential pathology. By using an image processing framework, placental measurement of volume and estimated blood flow have shown to provide potential indicators for pregnancy outcome at term in the first trimester of pregnancy. This chapter will summarise the key points of this thesis and consider directions for further development in the field.

7.1 Summary

The literature review of chapters 2 and 5 introduce the importance of the placenta through pregnancy and the underlying haemodynamic changes that occur to provide an environment for the predisposed genetic growth potential of a fetus to be achieved. The review highlights that the utero-placental interface (UPI) is considered by histo-pathological and clinical study to be the area in which pathology occurs.

In order to provide a fast, reliable method to measure the site of pathology as well as the placenta itself, we show in Chapter 3 the use of a semi-automated segmentation technique applied to 3D ultrasound of the placenta. The method was compared to manual segmentation and another semi-automated segmentation tool, VOCAL^{TM} . Three observers measured 10 subjects thrice using each measurement method and the volumetric results were compared. It was shown that both VOCAL^{TM} and the Random Walker method provided comparative performance in terms of repeatability and reproducibility. This was then used applied upon a pilot study of 143 women and showed that placenta volume in women with small-for-gestational age (SGA) babies as defined by customised birth-weight centile was significantly smaller than those defined as appropriate for gestational age (AGA).

In order to provide a fast and reliable method to measure the site of pathology as well as the placenta itself we show in Chapter 3 the use of a semi-automated segmentation technique applied to 3D ultrasound of the placenta. The method was compared to manual segmentation and another semi-automated segmentation tool, VOCAL^{TM} . Three observers measured 10 subjects thrice using each measurement method and the volumetric results were compared. It was shown that both VOCAL^{TM} and the Random Walker method provided comparative performance in terms of repeatability

and reproducibility. This was then used applied upon a pilot study of 143 women and showed that placenta volume in women with small-for-gestational age (SGA) babies as defined by customised birth-weight centile was significantly smaller than those defined as appropriate for gestational age (AGA).

Beyond the global measurement of placental volume, we then focused upon the interface between the placenta and mother, the utero-placental interface (UPI). To investigate discrete surfaces within a 3D PD sweep, manual manipulation is required within a qualitative framework meaning one cannot with precision investigate areas of interest or interrogate for example, a VOI either belonging to the UPI or at a certain distance with respect to it. We therefore came up with a method to present the information in the scan in a geometry with respect to the utero/placental border rather than in the x-y-z Cartesian geometry that is typically presented.

Our new method provides a novel way to visualise a given tissue layer relative to the utero-placental interface in a simple, understandable manner. Using this method, our clinical interest is to augment current understanding of the presence and pattern of blood flow as it enters the placenta in the first trimester. Using mesh parameterisation we showed the ability to convert a visualisation of the convoluted, curved utero-placental interface (UPI).

Finally, we attempted to estimate the vascularity of the placenta at this area of pathology by adapting our visualisation technique and applying a previously used 2D PD standardisation method, fractional moving blood volume (FMBV). In the review chapter that outlined the current clinical state-of-art in estimation of vascularity using power Doppler it was shown that many techniques suffer from poor reproducibility and lack any standardisation to perform inter-patient comparison. By first investigating the importance of machine settings and the appropriate use of gain we investigated

placental function by estimation of FMBV using a 3D implementation of the existing FMBV method using the plexus of arterioles 10mm away from the placental bed to provide a standardisation value from which it then measures discrete volumes of interest in the utero-placental arteries or within the placenta itself. We showed that estimations of vascularity decreased from the outside to the inside of the placenta. In the SGA subjects measured, we showed significantly smaller amounts of blood-flow when compared to the cohort of AGA babies.

7.2 Future Work

Building upon the work described in the previous chapters there are clear areas where continued work could provide a reduction in manual intervention and additional accuracy and reduction of sources of error. In considering these areas we first approach the improvements that could be made in acquisition of the reliable and consistent volume data clinically. With this data collected, the imaging framework that has been outlined in this thesis and the technical improvements that can be made can be considered. Finally, the application of some of the ideas of this work into other areas of healthcare and imaging can be discussed.

7.2.1 3D Doppler Acquisition

Our work has shown the impact of good acquisition methodology upon reducing the impact of machine settings upon the appearance of Doppler blood flow in the placenta. We have illustrated the appropriate use of gain and its impact upon image appearance and estimation. Gain represents one setting that has be customised to allow the best appearance of Doppler vascularity. There remain a number of different Doppler settings

such as pulse repetition frequency (PRF), wall-filter and clutter which are typically set to a fixed level at the start of any Doppler study to a level considered by the observer to present the "best" vascular appearance. Such an approach requires an objective method for selecting scanner settings to avoid the risk of introducing investigator bias when the settings are adjusted an example of which has already been shown to provide improved images by adjustment of the wall motion filter setting[183].

7.2.2 Volumetric Segmentation

The Random Walker algorithm used to segment placental volume requires an initialisation as described in Chapter 3. When investigating the training and initialisation aspect of the algorithm, it was shown in section 3.4.3 that a clear protocol and training run was required to produce adequate reproducability when compared to the other two observers. This could be achieved by either automating the initial seeding process or using a different automated segmentation strategy. A further consideration is that the small study of 143 patients we have used has produced segmentation data that could itself fold into training data for a machine-learning technique or drive a shape based approach to automated segmentation.

7.2.3 Local Placental Blood Flow Measurement

Measurement of blood patterns shows clear potential for exploitation by an automated method. Previous clinical work has used transvaginal ultrasound imaging of the placenta using a 2D colour/power Doppler probe to measure regional differences in placental blood flow. A number of papers have been published that investigate blood flow in the placenta in the first trimester[33,36,94,226,227] and report changes in the pattern of

flow in the IVS at the end of the first trimester. In these studies, the division between central and peripheral areas of the placenta was performed by manual outlining as determined by the observer. Figure 7.1 illustrates this delination process used in one particular study.

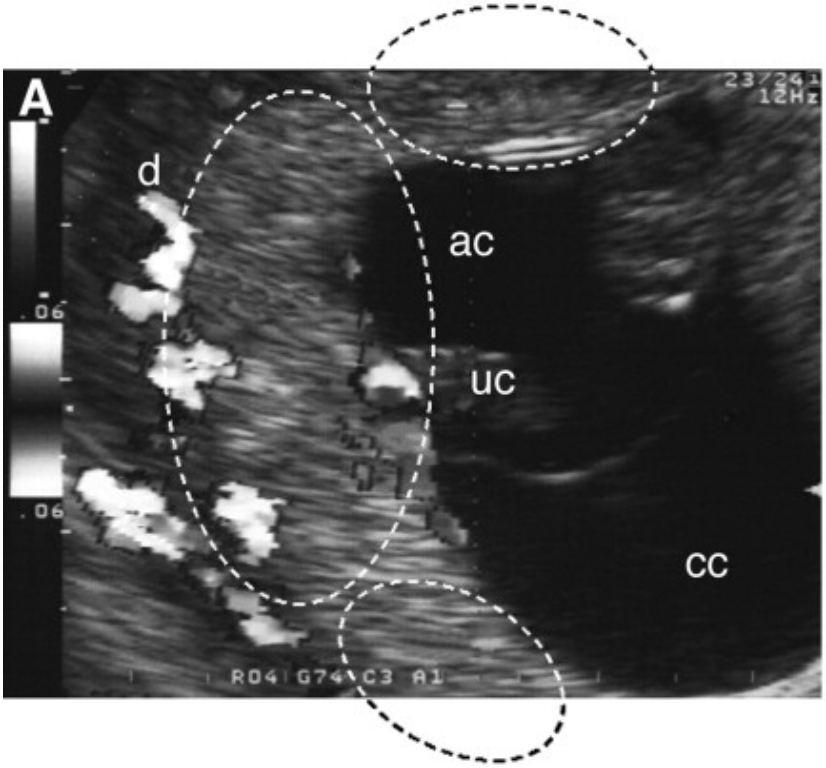

Figure 7.1: Mapping of the placental circulation at 8 weeks of gestation with colour Doppler showing the fetal circulation in the umbilical cord (uc) and the maternal circulation within the decidua (d). The dashed lines indicate the boundaries of the regions considered central and peripheral in this example (cc - chorionic cavity; ac - amniotic cavity). Reproduced with permission from Jauniaux et al.[35]

This has been investigated using ultrasound in 2D showing the appearance of blood flow first at the periphery and then centrally with respect to the placental bed. Intervillous blood flow was observed in abnormal pregnancies earlier in gestation and in a different pattern of appearance than in normal pregnancies[35]. From a 1997 review by Jaffe et al discussing these Doppler studies[29], they state that;

> *"Interestingly, when describing their methods of Doppler investigation of intervillous space circulation, the precise site of sampling is rarely indicated by the authors. [...] Even with the current sophisticated techniques there are still differences in interpretation of findings. Some of these differences are related to the scanning technique and are undoubtedly influenced by the sensitivity of the equipment used. [...] It is of paramount importance that investigators specify clearly from which part of the gestational sac signals have been observed."*

The review author's later paper illustrating the typical sampling and recording of blood flow within the paper in Figure 7.1 shows the typical 2D measurement of blood flow in the first trimester. What is clear is that the sampling is defined in approximate terms, roughly outlining peripheral and central zones. The definition of these zones it not explicitly defined and raises questions about the robustness of these measures between observers. The centrality for example of the placenta could be defined as centroid of the overall shape of the organ or from where the umbilical cord arises from the fetal side of the placenta. These locations are not necessarily the same although it could be proposed that both represent the "centre" of the placenta for geometric and anatomical reasons. A second important point they raise is the impact of machine settings upon the appearance and measurement of the placenta.

The 3D visualisation method shown in chapter 4 is capable of providing quantifiable measures of blood flow which could provide deeper insight in the patterns and changes of bloodflow between normal and abnormal pregnancies.

In our 143 subjects, the data was visualised as shown in Figures 4.8 and 4.9. Each polygonal mesh produced was stored for later analysis. As sweep angle and acquisition depth changes, the resolution of the captured volume will alter. Therefore the discrete

interval between displayed discs was calculated as the maximal distance across a single voxel ($\sqrt{(x^2+y^2+z^2)}$). Figures 7.2 show the typical output of the method, in particular we focused upon a distance into the placenta from the UPI of up to 5 voxels in depth. This equates to approximately the same number of millimetres and is in accordance with 2D studies produced clinically which indicate that the mean lengths of jets of blood flow as observed by Doppler ultrasound are 2.76mm (min. 0.9mm, max. 7.3mm, σ 1.21mm)[43] (Figure 2.9d illustrates this 2D measure).

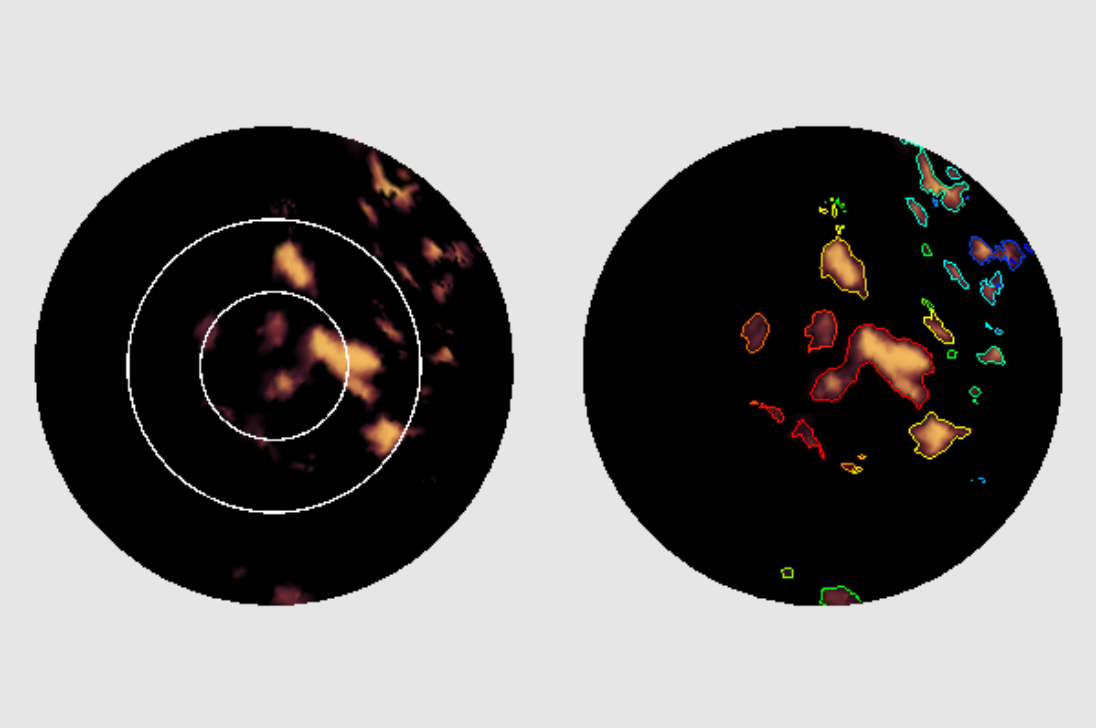

Figure 7.2: Parameterised 3D PD disc of surface 5 voxels into placenta from utero-placental interface (UPI), white discs indicate central and peripheral zones on the disc (left). Overlaid outlines of spurts automatically obtained using iso-contouring algorithm (right).

Given the scalar range of the power Doppler signal, an arbitrary threshold is used and from which polygons representing individual jets can be found. Figure 7.2 shows the use of Meandering Triangles (a triangular mesh variant of the Marching Cubes

algorithm) upon a disc of parameterised 3D PD data at a level of 5 voxels deep into the placenta. By contouring, the number of 'jets' of blood flow that were present was calculated. From this, individual jets can be measured in size relative to the total area of the disc and their position also recorded. As discussed previously, we defined the central part of the disc as any part within a circle one third the total radius of the disc. The was then reproduced for the periphery, defined as any part of the disc from two thirds of the total radius to the edge of the disc. This partitioning is shown in the left hand disc displayed in Figure 7.2. These numbers were then recorded and divided into two classes, where the fetal outcome was described as AGA or SGA the criteria for which was determined as described in section 2.2.1. Figure 7.3 illustrates the differences between the two groups.

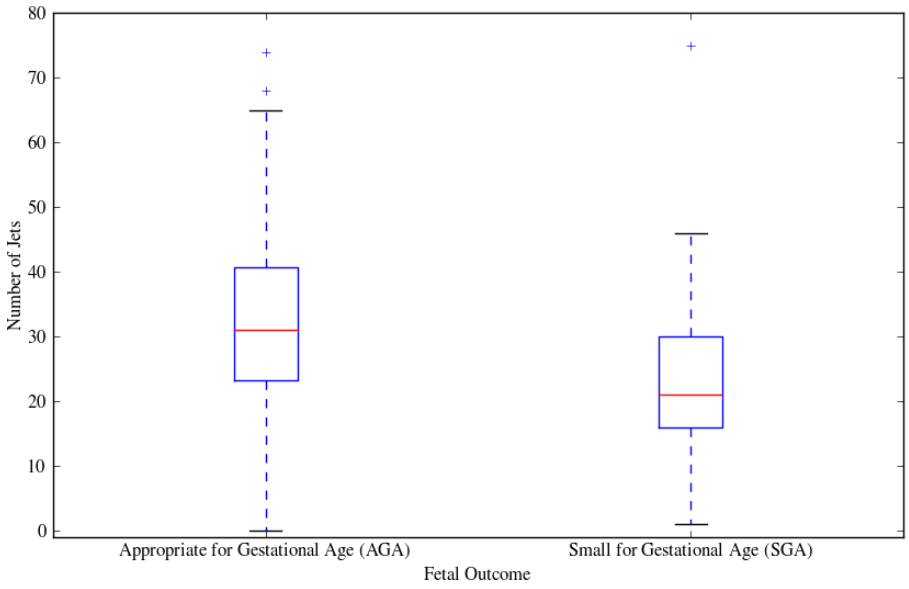

Figure 7.3: Boxplot showing AGA and SGA in 143 patients (122 AGA; 21 SGA)

Normality of the two groups was confirmed by Kolmogorov-Smirnoff test ($P >$

0.05) and the homogeneity of variances confirmed by Bartlett's test ($P > 0.05$). In all cases, presence of blood flow was detected in the periphery of the placenta regardless of outcome and in the central region, absence of flow was observed in 9 cases (1 - SGA; 8 - IUGR). Position would seem to lack the sensitivity to detect differences between the two outcomes in pregnancy. However, a significant difference was found between the number of jets found in the different populations ($P < 0.05$; Student t-test). This is ongoing work but shows the potential value of local analysis of the blood-flow in the inter-villous space using our technique.

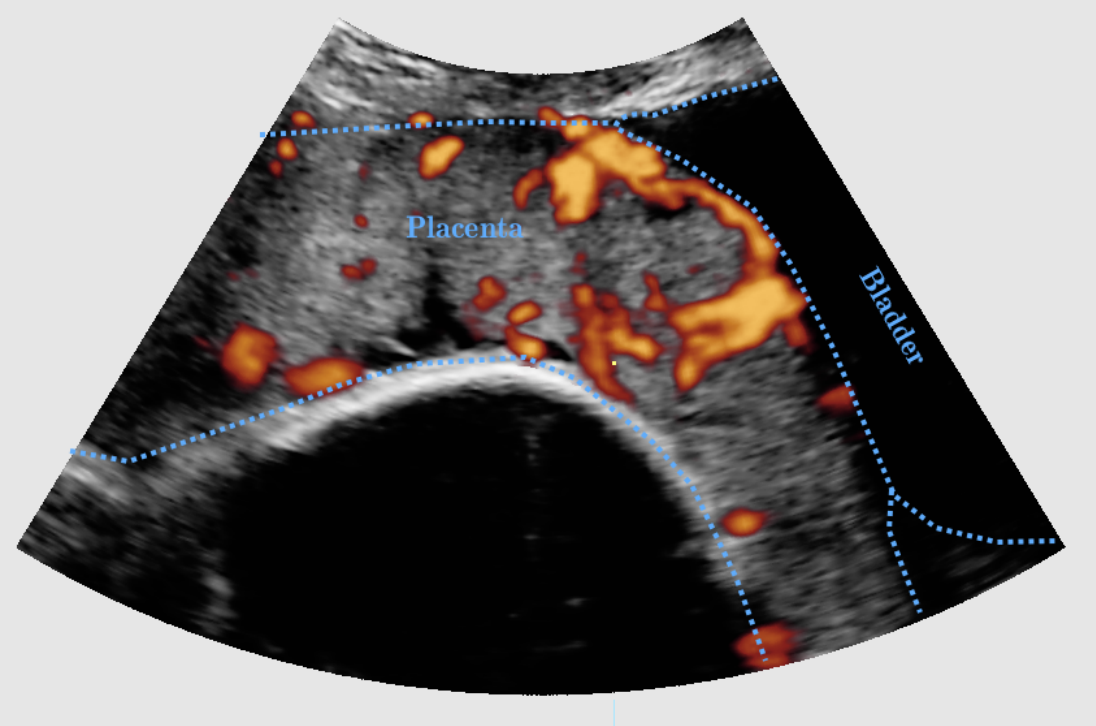

Figure 7.4: 2D PD slice of 3D volume of placenta accreta. Invasive vascularisation of surface between placental and bladder is shown. The proximity of the vascularisation to the hypo-echoic bladder wall indicate the potential risk of rupture or haemorrhage at birth. Placenta and bladder borders annotated and labelled in blue.

7.2.4 Placenta Accreta

The framework of tools that we have provided have the potential to be adapted to other areas of obstetrical pathology. In the case of placenta accreta, where the placenta invades too deeply in the uterine tissue, this complication can lead to severe haemorrhage, hysterectomy or be fatal. Over the last few decades, the incidence of accreta has grown sharply due to the increased caesarian section rate which is known to be an associative factor[228,229]. A recent clinical study using off-the-shelf imaging tools as described in chapter 2 visualised 'numerous coherent vessels' using 3D power Doppler in the semi-opaque rendered view of the utero-placental interface. This qualitative imaging biomarker provided the best single criterion for the diagnosis of placenta accreta against other ultrasound modalities and features. 3D power Doppler provided a sensitivity of 97% and a specificity of 92% when detecting a group of 39 patients with placenta accreta out of a total study of 170[230].

Of particular interest is the visualisation of the interface between the placenta and when blood-flow is observed invading right into the cavity of the bladder. With the visualisation of distinct surfaces that we have constructed and combined with the ease to segment the hyper-echoic bladder a visualisation showing the interface between bladder and bloodflow may add quantification of the degree of blood flow invasion.

7.2.5 Screening Test

The contributions of this thesis have shown that placental volume and 3D power Doppler measurement of the placenta can be used to predict SGA separately. By combination of these imaging biomarkers into a single predictive test in the style of the clinical study performed in Chapter 3 we may boost the discrimination of normal from SGA

babies.

Appendix A

Segmentation Protocol[1]

A.1 Procedural Outline

THE segmentation technique, Random Walker, requires an initialisation that is performed by a user. This comprises of outlining areas of background and foreground or in our particular clinical case, the placenta and the area surrounding it (uterine tissue & cavity). Our protocol is for 3D volumetric segmentation, as a result multiple slices in the B-mode plane are manually segmented/outlined and then fed as an initialisation into the algorithm which then produces a probabilistic result. This is then thresholded at a given probability value, to give a result from which a volume can be calculated.

The steps in order to perform an initialisation of the algorithm as a user are as follows. The assumption is that ITK-SNAP is used to view and segment the images.

1. Load greyscale volume into an appropriate viewer, such as ITK-SNAP.

[1]Work was produced in collaboration with Dr. Sally Collins, Nuffield Department of Obstetrics and Gynaecology.

2. Select the acquired plane, not either of the reconstructed planes, and maximise.

3. Settings:

   (a) Linear interpolation must be set to 'On'.

   (b) Paintbrush should be set to 6-8 pixels in size, square and isotropic.

   (c) Different colours should be used to represent background and placental tissue. Figures show a typical colour scheme.

4. Scroll backwards and forwards through the individual 2D images until the user feels confident that they can identify the boundaries of the placenta.

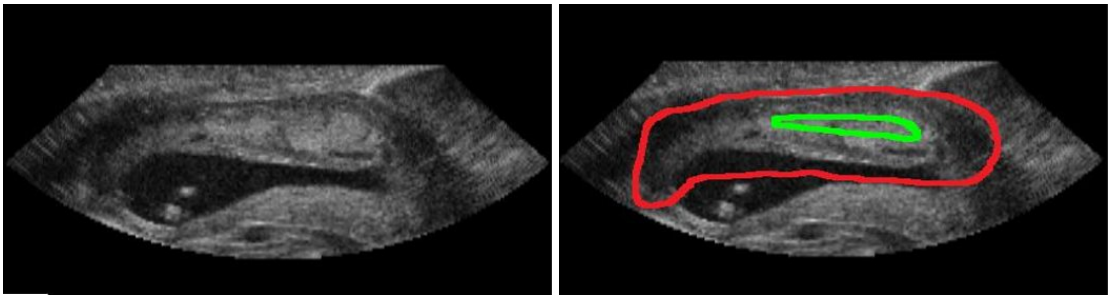

(a) (b)

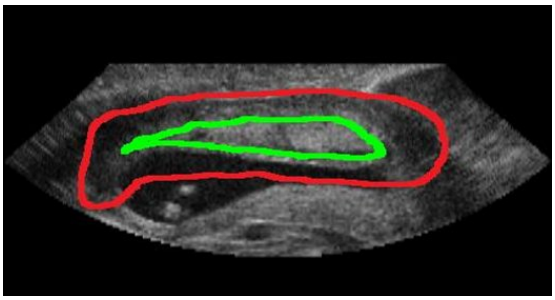

(c)

Figure A.1: Two different seedings of the same 2D slice, Figure A.1a , illustrating the requirement to indicate to fully seed placenta where non-heterogenous tissue appears. Figure A.1b - cystic areas have not been identified as placental tissue. Figure A.1c - seeding that encorporates all of the different greyscale textures within this placenta and encompasses the complete shape of the organ.

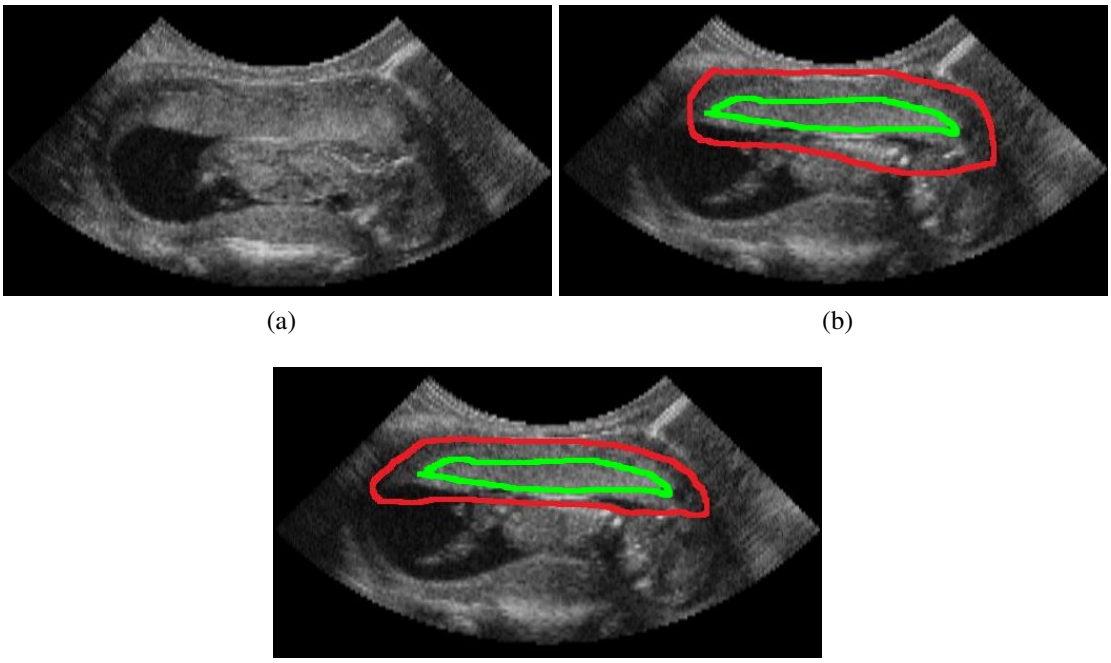

(a) (b)

(c)

Figure A.2: Two different seedings of the same 2D image, Figure A.2a. Figure A.2b - Fetal spine has not been indicated as background which gives potential for leaking into fetal tissue which has similiar image statistics to placenta. Figure A.2c - background tighter bounded than Fig. A.2b which leads to less ambiguity and potential leakage into fetal anatomy.

5. Starting from one end of the placenta, seed the first 3 images. Then continue seeding every ten slices until reaching the other end. At this point, seed the last three slices of the placenta.

6. Seeding of a slice should be done using the steps as outlined below.

   (a) The lines defining the placenta and the background should be placed close to, but not over, the placental boundary. A closed loop is usually employed for both but where the placenta is very thin the placental label may have to be just a single line. The 'placenta defining' loop is indicating that everything within the loop is placental tissue and the algorithm will recog-

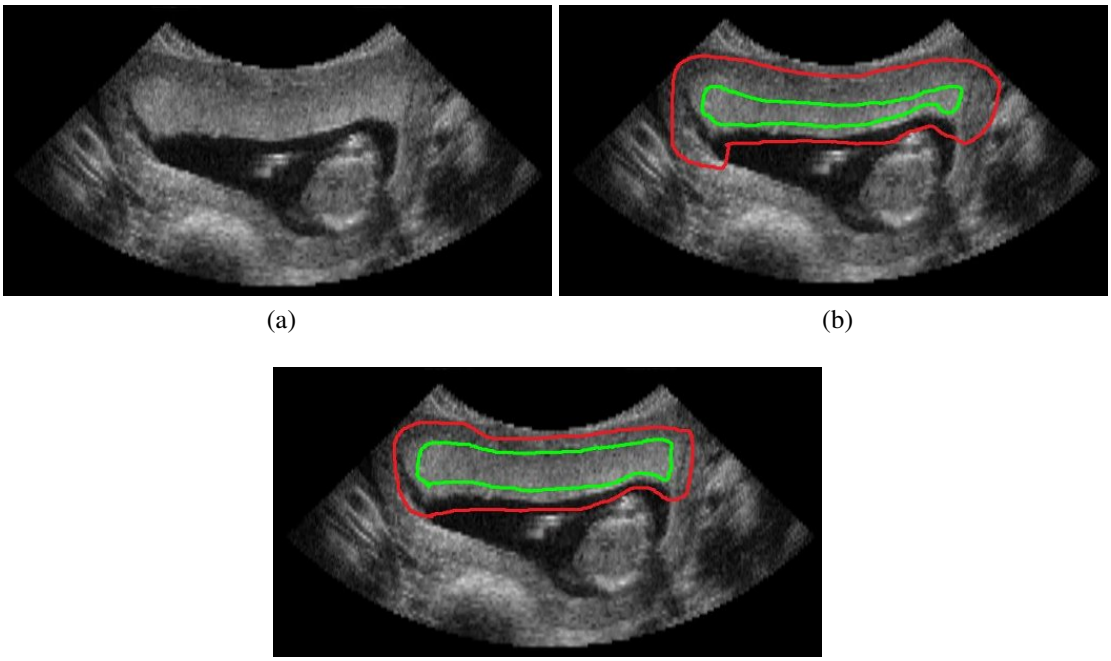

(a) (b)

(c)

Figure A.3: Two different seedings of the same 2D image, Figure A.3a where the utero/placental interface is poorly defined. Figure A.3b shows foreground seeding encroaching upon the uterine tissue. Figure A.3c shows a better outline of the foreground leaving the algorithm to define the most likely site of the boundary.

nise it as such. The 'background defining' loop is indicating that everything outside the loop is not placental tissue.

(b) Where the placental tissue is hetrogeneous (e.g cystic) care must be taken to encompass all the different textures within the 'placenta defining' loop. See Figure A.1 (a).

(c) Care must also be taken when the fetus is in close proximity to the placental/amniotic fluid boundary, see Figure A.2. In these situations the gap between the loops may be very small so that the user is nearly delineating the interface.

(d) In contrast, when the boundary is unclear, scrolling back and forth through the adjacent images should provide extra information as to the perceived location. The gap between the two loops should then be left large enough to allow the algorithm to define the most likely position of the boundary. See Figure A.3.

7. Save the image.

Appendix B

Spiral 3D - Study Ethics

Patient Information Leaflet provided to participants enrolled as part of the Spiral 3D Study (overleaf).

Oxford Fetal Medicine Unit

Oxford Radcliffe Hospitals NHS
NHS Trust

Patient information Leaflet

An investigation of potential new markers for impaired placentation in early pregnancy (REC Ref: 08/H0604/163)

We would like to invite you to take part in a research study. Before you decide, you need to understand why the research is being done and what it will involve for you. Please take the time to read the following information. Talk to others about the study if you wish, perhaps your GP or midwife. Ask us if there is anything that is not clear, or if you would like more information.

Why have I been invited?
You have been invited because you are pregnant and living in the Oxford area. We intend to study between 150 and 200 women, the vast majority of who will be 'low risk' and have entirely normal pregnancies.

What is the purpose of the study?
Every baby is believed to have an inherent growth potential which under ideal conditions should produce a healthy baby the appropriate size. In a few pregnancies the placenta does not work as well as it should and as a result the baby may not grow as well as it should. This problem is called intrauterine growth restriction (IUGR). The consequences of IUGR include an increased risk of still-birth (the baby dying before it is born), problems occurring around the time of birth and the child developing cerebral palsy. Early recognition of babies developing IUGR, leading to appropriate monitoring and timely delivery may potentially improve the outcome for the baby.

With the advent of three dimensional (3-D) ultrasound scanning it has become possible to safely look at the placenta early in pregnancy. This should be able to give an indication of whether the placenta is functioning properly long before the baby starts showing signs that the placenta is not working well.

We want to assess the effectiveness of 3-D ultrasound in identifying those babies at risk of IUGR in early pregnancy. This will hopefully lead to development of a simple, non-invasive screening test which could be offered to all women to identify those babies at risk of IUGR. This will allow us to start monitoring these babies earlier and improve the outcome of that pregnancy. We also hope that it would prevent the medicalisation of other pregnancies which were always destined to have a normal outcome.

Do I have to take part?
It is up to you to decide whether or not to take part. Your decision will not affect the standard of care you receive. This information sheet describes the study. If you have further questions Dr Sally Collins or Mr Lawrence Impey will be happy to answer them for you. If you do decide to help us with the study, we will ask you to sign a consent form to show you have agreed to take part. You are free to withdraw from the study at any time, without giving a reason.

What will happen to me if I take part?
You will be offered an initial appointment about 12 weeks into the pregnancy. If you have decided to have the screening test for Down syndrome, the 'Nuchal' scan, we will do our best to see you the same day to avoid extra visits to the hospital. Don't worry if you have decided not to have that scan as you can still be included in our study.

At that first meeting we will ask you a few questions about your health and the pregnancy, explain the study in detail and answer any questions which you may have. If you chose to continue we will ask you to read and sign a consent form then we will proceed with the ultrasound scan which will look at your baby in the traditional two-dimensions and the placenta in three-dimensions. We will also generate a growth chart which is specific to your baby which we will use to monitor your baby's growth at future visits.

The next 4 visits will take place when you are around 14, 16, 18 and 23 weeks pregnant. These will involve 2-D ultrasound measurement of your baby's growth and 3-D ultrasound measurement of the placenta.

The last two visits will be at 28 and 33 weeks and will just involve 2-D ultrasound measurement of your baby's growth.

During no part of your pregnancy will any type of treatment or care be withheld from you because you are taking part in the study. You may find it helpful to look at the flow chart at the end of this leaflet which shows when we would do each scan. The whole study is expected to take three years to complete although your inclusion will be for the duration of your pregnancy. If you take part in the study you will be asked to make four to five additional visits to the hospital during your pregnancy.

Is it safe and what are the possible disadvantages of taking part?
We recognise that we are asking you to attend for more ultrasound scans than you would normally have during routine antenatal care. However, ultrasound has no known risks in pregnancy and all our scans will be performed after the most sensitive period of pregnancy is completed. Furthermore, all our 3-D and Doppler studies will be of the placenta, and maternal blood vessels and therefore will not involve your baby. Attending for the scans may be inconvenient, however every effort will be made to minimise this by being as flexible as possible to your timetable.

What are the possible benefits of taking part?
Participating in the study will enable you to see your baby more closely and more often than you normally would. Extra growth scans later on in pregnancy as well as identifying IUGR could potentially identify other problems such as breech presentation which, very occasionally, can be missed during routine care. In these circumstances, Dr Sally Collins or Mr Lawrence Impey will discuss the implications with you and appropriate management will be

initiated with your consent. Unfortunately we are unable to offer any expenses to you for taking part in this study but we hope that the extra scans may compensate you for the inconvenience of the extra visits.

What if there is a problem?
Compensation for harm arising from an accidental injury and occurring as a consequence of your participation in the study would be covered by the NHS.

If you wish to make a complaint about any aspect of the trial this should be directed to: Mr Lawrence Impey
The Fetal Medicine Unit
Level 6, The Women's Centre
John Radcliffe Hospital
Oxford, OX3 9DU
Tel: 01865 221710

Will my taking part in the study be kept confidential?
If you consent to take part in the research, some parts of your medical records and the results of the study will be looked at by members of the research team, authorised persons from the Oxford Radcliffe NHS trust. Regulatory authorities may also look at the results to check that the study is being carried out correctly. All will have a duty of confidentiality to you as a research participant and we will do our best to meet this duty. With your consent, we will inform your GP that you are taking part in the study. The results of your baby's growth scans will be placed in your hand-held notes

Any information about you which leaves the Fetal Medicine Unit would have your name and address removed so that you cannot be recognised from it. Data will be stored on a computer database in the Fetal Medicine Unit. You will be identified in our computers by a number and not by name and all information will be strictly confidential.

What will happen if I don't want to carry on with the study?
You may withdraw from the study at any time during your pregnancy. This will not affect the care you get in any way. Information collected before your withdrawal may still be used.

What will happen to the results of the research study?
We will tell you the results of your individual scans at the time they are done. Furthermore, results will be written up as manuscripts for submission to scientific journals. If you were interested, we could provide you with a copy of the article after publication. You are not going to be identifiable in any report or publication.

Who is organising and funding the research?
The research is being carried out by the Fetal Medicine Unit and the Nuffield Department of Obstetrics and Gynaecology, University of Oxford. The study is

sponsored by the Oxford Radcliffe Hospitals NHS trust and is funded by the Oxford Comprehensive Biomedical Research Centre (which is in turn funded by the National Institute for Health Research). The study will contribute towards the D.Phil thesis (University of Oxford) for Dr Sally Collins.

Who has reviewed the study?
Research is reviewed by an independent group of people called a Research Ethics Committee to protect your safety, rights, well being and dignity. This study has been reviewed and given favourable opinion by Oxfordshire Clinical Research Ethics Committee.

What do I do if I want to take part in the study?
Please call Dr Sally Collins on **01865 220129** to arrange an appointment at a time to suit. This appointment needs to take place when you are around 12 weeks pregnant. Alternatively, you can mention it to the ultrasound department staff when you come in for your scan and we will do our best to see you at the same time or organise an appointment for as soon as possible.

Contact for further information
If you have any further questions please do not hesitate to contact Mr Lawrence Impey or Dr Sally Collins at the address below:

The Fetal Medicine Unit
Level 6, The Women's Centre
John Radcliffe Hospital
Oxford
OX3 9DU

Phone: 01865 220129
E mail: sally.collins@obs-gyn.ox.ac.uk

Oxford Fetal Medicine Unit

Oxford Radcliffe Hospitals NHS
NHS Trust

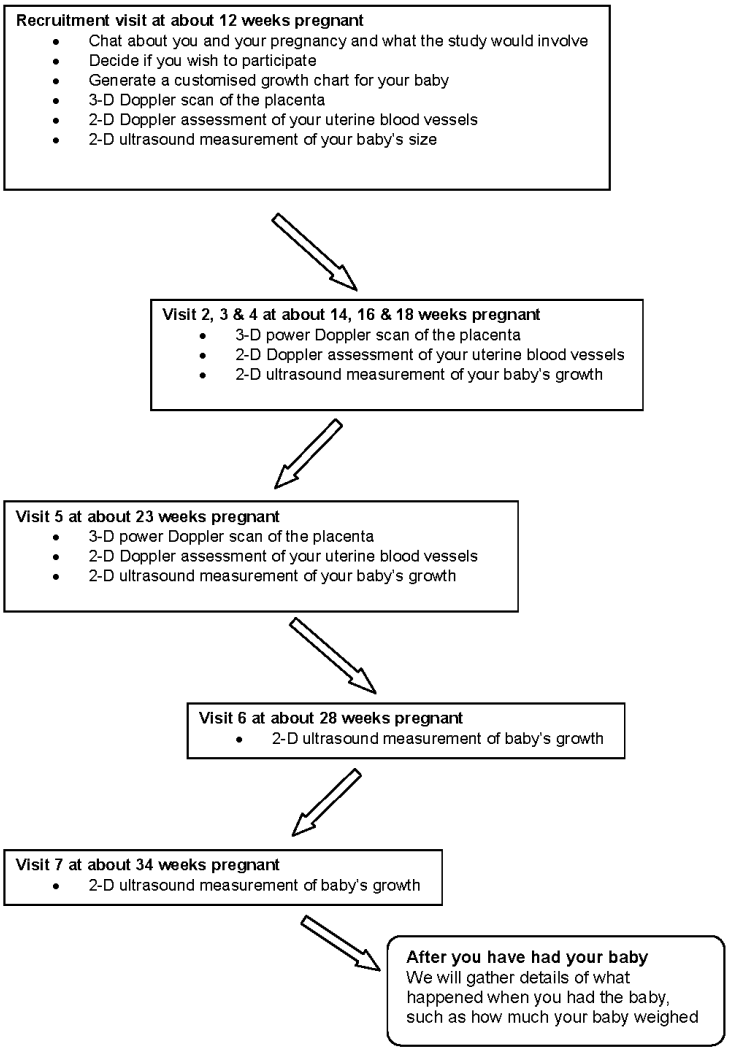

Appendix C

Machine Settings for GE Voluson® E8 Ultrasound Scanner

Power Doppler Settings		B-Mode Settings	
Quality	Norm	Speckle Reduction Imaging (SRI)	3
Wall motion filter (WMF)	Low 1	Angle	60
Pulse repetition frequency (PRF)	0.9KHz	Dynamic Contrast	6
PD Colour Map	5	Focal Zones	1
Frequency	Low	Harmonic Frequency	High
Flow Resolution	Mid 2	Gain	5
Line Filter	2	Gray map	7
Artefact	On	Tint	Clear
Smooth	Rise 4	Line Filter	Off
Line Density	6	Persistance	3
Smooth	Fall 5	Enhance	3
Ensemble	15	Line Density	Normal
Balance	150	Reject	15

Bibliography

1. K. H. Nicolaides, "Turning the pyramid of prenatal care," *Fetal Diagnosis and Therapy*, vol. 29, no. 3, p. 183–196, 2011. [Online]. Available: http://www.ncbi.nlm.nih.gov/pubmed/21389681

2. G. J. Kloosterman, "On intrauterine growth. the significance of prenatal care." *Int J Gynaecol Obstet*, vol. 8, p. 895–912, 1970.

3. D. Barker, A. Bull, C. Osmond, and S. Simmonds, "Fetal and placental size and risk of hypertension in adult life." *British Medical Journal*, vol. 301, no. 6746, p. 259, 1990.

4. T. Jansson and T. Powell, "Role of the placenta in fetal programming: underlying mechanisms and potential interventional approaches," *Clinical Science*, vol. 113, p. 1–13, 2007.

5. M. Yampolsky, C. Salafia, O. Shlakhter, D. Haas, B. Eucker, and J. Thorp, "Centrality of the umbilical cord insertion in a human placenta influences the placental efficiency," *Placenta*, vol. 30, no. 12, p. 1058–1064, 2009.

6. L. Vorvick, *Anatomy of a normal placenta*, 2010.

7. E. Ramsey and J. Harris, "The morphology of human uteroplacental vasculature," *Contributions to Embryology*, vol. 38, p. 45–56, 1966.

8. W. Hunter, *Anatomia Uteri Humani Gravidi Tabulis Illustrata... The Anatomy of the Human Gravid Uterus Exhibited in Figures*. John Baskerville, 1774.

9. K. Benirschke and P. Kaufmann, *Pathology of the human placenta*. Springer Verlag, 2000.

10. G. Burton, A. Woods, and E. Jauniaux, "Rheological and physiological consequences of conversion of the maternal spiral arteries for uteroplacental blood flow during human pregnancy," *Placenta*, vol. 30, no. 6, p. 473–482, 2009.

11. K. Ueland, M. Novy, E. Peterson, and J. Metcalfe, "Maternal cardiovascular dynamics. IV. the influence of gestational age on the maternal cardiovascular response to posture and exercise." *American Journal of Obstetrics and Gynecology*, vol. 104, no. 6, p. 856, 1969.

12. N. Assali, *Biology of gestation*. Academic Press New York, 1968, vol. 1.

13. C. Rosenfeld, "Distribution of cardiac output in ovine pregnancy," *American Journal of Physiology - Heart and Circulatory Physiology*, vol. 232, no. 3, p. H231, 1977.

14. J. Browne and N. Veall, "The maternal placental blood flow in normotensive and hypertensive women," *BJOG: An International Journal of Obstetrics & Gynaecology*, vol. 60, no. 2, p. 141–147, 1953.

15. W. Hamilton and J. Boyd, "Development of the human placenta in the first three months of gestation," *Journal of Anatomy*, vol. 94, no. Pt 3, p. 297, 1960.

16. I. Brosens, W. B. Robertson, and H. G. Dixon, "The physiological response of the vessels of the placental bed to normal pregnancy," *J Pathol Bacteriol*, vol. 93, p. 569–579, Apr. 1967.

17. P. Kaufmann, S. Black, and B. Huppertz, "Endovascular trophoblast invasion: implications for the pathogenesis of intrauterine growth retardation and preeclampsia," *Biology of reproduction*, vol. 69, no. 1, p. 1, 2003.

18. R. Pijnenborg, J. Bland, W. Robertson, and I. Brosens, "Uteroplacental arterial changes related to interstitial trophoblast migration in early human pregnancy," *Placenta*, vol. 4, no. 4, p. 397–413, 1983.

19. W. Robertson, T. Khong, I. Brosens, F. De Wolf, B. Sheppard, and J. Bonnar, "The placental bed biopsy: review from three european centers." *American Journal of Obstetrics and Gynecology*, vol. 155, no. 2, p. 401, 1986.

20. S. Robson, E. Ball, F. Lyall, H. Simpson, S. Ayis, and J. Bulmer, "Endovascular trophoblast invasion and spiral artery transformation: the "two wave" theory revisited," *Placenta*, vol. 22, p. A25, 2001.

21. F. Lyall, "The human placental bed revisited," *Placenta*, vol. 23, no. 8-9, p. 555–562, 2002.

22. I. Brosens, H. Dixon, and W. Robertson, "Fetal growth retardation and the arteries of the placental bed," *BJOG: An International Journal of Obstetrics & Gynaecology*, vol. 84, no. 9, p. 656–663, 1977.

23. D. Barker, "Maternal nutrition, fetal nutrition, and disease in later life," *Nutrition*, vol. 13, no. 9, p. 807–813, 1997.

24. ——, *Mothers, babies, and health in later life*. Elsevier Health Sciences, 1998.

25. D. Barker, K. Godfrey, P. Gluckman, J. Harding, J. Owens, and J. Robinson, "Fetal nutrition and cardiovascular disease in adult life," *The Lancet*, vol. 341, no. 8850, p. 938–941, 1993.

26. E. Ramsey, M. Donner, and R. Crosby, *Placental Vasculature and Circulation: Anatomy, Physiology, Radiology, Clinical Aspects, Atlas and Textbook*. Thieme, 1980.

27. J. Hustin, J. Schaaps *et al.*, "Echographic [corrected] and anatomic studies of the maternotrophoblastic border during the first trimester of pregnancy." *American Journal of Obstetrics and Gynecology*, vol. 157, no. 1, p. 162, 1987.

28. J. Schaaps and J. Hustin, "In vivo aspect of the maternal-trophoblastic border during the first trimester of gestation," *Trophoblast Res*, vol. 3, p. 39–48, 1988.

29. R. Jaffe, E. Jauniaux, and J. Hustin, "Maternal circulation in the first-trimester human placenta - myth or reality?" *American Journal of Obstetrics and Gynecology*, vol. 176, no. 3, p. 695–705, 1997.

30. E. Jauniaux, D. Jurkovic, and S. Campbell, "In vivo investigations of the anatomy and the physiology of early human placental circulations," *Ultrasound in Obstetrics & Gynecology*, vol. 1, no. 6, p. 435–445, 1991.

31. R. Jaffe and J. Woods Jr, "Color Doppler imaging and *in vivo* assessment of the anatomy and physiology of the early uteroplacental circulation." *Fertility and sterility*, vol. 60, no. 2, p. 293, 1993.

32. M. Coppens, P. Loquet, M. Kollen, F. De Neubourg, and P. Buytaert, "Longitudinal evaluation of uteroplacental and umbilical blood flow changes in normal early pregnancy," *Ultrasound in Obstetrics & Gynecology*, vol. 7, no. 2, p. 114–121, 1996.

33. L. Valentin, P. Sladkevicius, R. Laurini, H. Söderberg, and K. Marsál, "Uteroplacental and luteal circulation in normal first-trimester pregnancies: Doppler ultrasonographic and morphologic study," *American Journal of Obstetrics and Gynecology*, vol. 174, no. 2, p. 768–775, 1996.

34. G. Burton, E. Jauniaux, and A. Watson, "Maternal arterial connections to the placental intervillous space during the first trimester of human pregnancy: The

boyd collection revisited." *American Journal of Obstetrics & Gynecology*, vol. 181, no. 3, p. 718, 1999.

35. E. Jauniaux, J. Hempstock, N. Greenwold, and G. Burton, "Trophoblastic oxidative stress in relation to temporal and regional differences in maternal placental blood flow in normal and abnormal early pregnancies," *The American journal of pathology*, vol. 162, no. 1, p. 115–125, 2003.

36. E. Jauniaux, J. Zaidi, D. Jurkovic, S. Campbell, and J. Hustin, "Pregnancy: Comparison of colour Doppler features and pathological findings in complicated early pregnancy," *Human reproduction*, vol. 9, no. 12, p. 2432–2437, 1994.

37. J. Hustin, E. Jauniaux, and J. Schaaps, "Histological study of the materno-embryonic interface in spontaneous abortion," *Placenta*, vol. 11, no. 6, p. 477–486, 1990.

38. E. Jauniaux, A. Watson, J. Hempstock, Y. Bao, J. Skepper, and G. Burton, "Onset of maternal arterial blood flow and placental oxidative stress: a possible factor in human early pregnancy failure," *The American journal of pathology*, vol. 157, no. 6, p. 2111–2122, 2000.

39. R. Pijnenborg, G. Dixon, W. Robertson, and I. Brosens, "Trophoblastic invasion of human decidua from 8 to 18 weeks of pregnancy," *Placenta*, vol. 1, no. 1, p. 3–19, 1980.

40. R. Pijnenborg, J. Bland, W. Robertson, G. Dixon, and I. Brosens, "The pattern of interstitial trophoblastic invasion of the myometrium in early human pregnancy." *Placenta*, vol. 2, no. 4, p. 303, 1981.

41. J. Gardosi, A. Chang, B. Kalyan, D. Sahota, and E. Symonds, "Customised antenatal growth charts," *The Lancet*, vol. 339, no. 8788, p. 283–287, 1992.

42. J. Gardosi, F. Figueras, B. Clausson, and A. Francis, "The customised growth potential: an international research tool to study the epidemiology of fetal growth," *Paediatric and perinatal epidemiology*, vol. 25, no. 1, p. 2–10, 2011.

43. S. L. Collins, "Development of placental ultrasound markers to screen for the term, small for gestational age (SGA) baby," Ph.D. dissertation, Oxford University, 2012.

44. R. Bauer, B. Walter, P. Brust, F. Füchtner, and U. Zwiener, "Impact of asymmetric intrauterine growth restriction on organ function in newborn piglets," *European Journal of Obstetrics & Gynecology and Reproductive Biology*, vol. 110, p. S40–S49, 2003.

45. S. Sankaran and P. Kyle, "Aetiology and pathogenesis of IUGR," *Best Practice & Research Clinical Obstetrics & Gynaecology*, vol. 23, no. 6, p. 765–777, 2009.

46. ONS, "Death registration summary tables, England & Wales," Office for National Statistics, Tech. Rep., 2011.

47. CEMACH, "Confidential enquiry into maternal and child health (CEMACH)," Perinatal Mortality, England, Wales and Northern Ireland, Tech. Rep., 2008.

48. J. Gardosi, V. Madurasinghe, M. Williams, A. Malik, and A. Francis, "Maternal and fetal risk factors for stillbirth: population based study," *BMJ: British Medical Journal*, vol. 346, 2013.

49. S. Naylor, "Biomarkers: Current perspectives and future prospects." *Expert Review of Molecular Diagnostics*, vol. 3, no. 5, p. 525, 2003.

50. J. Smith, A. Sorensen, and J. Thrall, "Biomarkers in imaging: Realizing radiology's future," *Radiology*, vol. 227, no. 3, p. 633, 2003.

51. I. Vogel, P. Thorsen, A. Curry, P. Sandager, and N. Uldbjerg, "Biomarkers for the prediction of preterm delivery," *Acta Obstetricia et Gynecologica Scandinavica*, vol. 84, no. 6, p. 516–525, 2005.

52. G. Smith, E. Stenhouse, J. Crossley, D. Aitken, A. Cameron, and J. Connor, "Development: early-pregnancy origins of low birth weight," *Nature*, vol. 417, no. 6892, p. 916–916, 2002.

53. A. Gagnon, R. Wilson, F. Audibert, V. Allen, C. Blight, J. Brock, V. Désilets, J. Johnson, S. Langlois, A. Summers *et al.*, "Society of obstetricians and gynaecologists of canada genetics committee. obstetrical complications associated with abnormal maternal serum markers analytes," *J Obstet Gynaecol Can*, vol. 30, no. 10, p. 918–949, 2008.

54. N. Cowans, K. Spencer, and H. Meiri, "First-trimester maternal placental protein 13 levels in pregnancies resulting in adverse outcomes," *Prenatal Diagnosis*, vol. 28, no. 2, p. 121–125, 2008.

55. K. Spencer, N. Cowans, and A. Stamatopoulou, "ADAM12s in maternal serum as a potential marker of pre-eclampsia," *Prenatal Diagnosis*, vol. 28, no. 3, p. 212–216, 2008.

56. B. Thilaganathan, E. Ralph, A. Papageorghiou, K. Melchiorre, and J. Sheldon, "Raised maternal serum cystatin c: an early pregnancy marker for preeclampsia," *Reproductive Sciences*, vol. 16, no. 8, p. 788, 2009.

57. G. Smith, J. Crossley, D. Aitken, J. Pell, A. Cameron, J. Connor, and R. Dobbie, "First-trimester placentation and the risk of antepartum stillbirth," *JAMA: the Journal of the American Medical Association*, vol. 292, no. 18, p. 2249, 2004.

58. K. Melchiorre, K. Leslie, F. Prefumo, A. Bhide, and B. Thilaganathan, "First-trimester uterine artery Doppler indices in the prediction of small-for-gestational age pregnancy and intrauterine growth restriction," *Ultrasound in Obstetrics and Gynecology*, vol. 33, no. 5, p. 524–529, 2009.

59. J. Cnossen, R. Morris, G. Ter Riet, B. Mol, J. Van Der Post, A. Coomarasamy, A. Zwinderman, S. Robson, P. Bindels, J. Kleijnen *et al.*, "Use of uterine artery Doppler ultrasonography to predict pre-eclampsia and intrauterine growth restriction: a systematic review and bivariable meta-analysis," *Canadian Medical Association Journal*, vol. 178, no. 6, p. 701, 2008.

60. G. Mandruzzato, P. Bogatti, L. Fischer, and C. Gigli, "The clinical significance of absent or reverse end-diastolic flow in the fetal aorta and umbilical artery," *Ultrasound in Obstetrics and Gynecology*, vol. 1, no. 3, p. 192–196, 1991.

61. A. Baschat and C. Weiner, "Umbilical artery Doppler screening for detection of the small fetus in need of antepartum surveillance," *American Journal of Obstetrics & Gynaecology*, vol. 182, no. 1, p. 154–158, 2000.

62. C. Chang, P. Tsai, C. Yu, H. Ko, and F. Chang, "Prenatal detection of fetal growth restriction by fetal femur volume: efficacy assessment using three-dimensional ultrasound," *Ultrasound in Medicine & Biology*, vol. 33, no. 3, p. 335–341, 2007.

63. L. Law, T. Leung, D. Sahota, L. Chan, T. Fung, and T. Lau, "Which ultrasound or biochemical markers are independent predictors of small-for-gestational age?" *Ultrasound in Obstetrics and Gynecology*, vol. 34, no. 3, p. 283–287, 2009.

64. R. Bindra, V. Heath, A. Liao, K. Spencer, and K. Nicolaides, "One-stop clinic for assessment of risk for trisomy 21 at 11–14 weeks: a prospective study of 15,030 pregnancies," *Ultrasound in Obstetrics and Gynecology*, vol. 20, no. 3, p. 219–225, 2002.

65. G. Karagiannis, R. Akolekar, R. Sarquis, D. Wright, and K. Nicolaides, "Prediction of small-for-gestation neonates from biophysical and biochemical markers at 11–13 weeks," *Fetal Diagnosis and Therapy*, vol. 29, no. 2, p. 148–154, 2011.

66. E. Hafner, M. Metzenbauer, D. Hófinger, F. Stonek, K. Schuchter, T. Waldhór, and K. Philipp, "Comparison between three-dimensional placental volume at 12 weeks and uterine artery impedance/notching at 22 weeks in screening for pregnancy-induced hypertension, pre-eclampsia and fetal growth restriction in a

low-risk population," *Ultrasound in Obstetrics & Gynecology*, vol. 27, no. 6, p. 652–657, 2006.

67. J. De Wilde, A. Rivers, and D. Price, "A review of the current use of magnetic resonance imaging in pregnancy and safety implications for the fetus," *Progress in Biophysics and Molecular Biology*, vol. 87, no. 2-3, p. 335–353, 2005.

68. J. Bushberg, *The essential physics of medical imaging*. Williams & Wilkins, 2002.

69. I. Donald, J. Macvicar, and T. G. Brown, "Investigation of abdominal masses by pulsed ultrasound," *The Lancet*, vol. 271, no. 7032, pp. 1188 – 1195, 1958. [Online]. Available: http://www.sciencedirect.com/science/article/B6T1B-497S8XM-CS/2/c3a7ba953d4a0701b58d01383b760f32

70. I. Donald, "Ultrasonics in obstetrics," *British Medical Bulletin*, vol. 24, no. 1, p. 71, 1968.

71. I. Donald and U. Abdulla, "Placentography by sonar," *BJOG: An International Journal of Obstetrics & Gynaecology*, vol. 75, no. 10, p. 993–1006, 1968.

72. J. Villar, H. Knight, M. de Onis, E. Bertino, G. Gilli, A. Papageorghiou, L. Ismail, F. Barros, and Z. Bhutta, "Conceptual issues related to the construction of prescriptive standards for the evaluation of postnatal growth of preterm infants," *Archives of Disease in Childhood*, vol. 95, no. 12, p. 1034, 2010.

73. J. Noble and D. Boukerroui, "Ultrasound image segmentation: A survey," *IEEE Transactions on Medical Imaging*, vol. 25, no. 8, p. 987–1010, 2006.

74. F. Duck, "Nonlinear acoustics in diagnostic ultrasound," *Ultrasound in Medicine & Biology*, vol. 28, no. 1, p. 1–18, 2002.

75. A. Fenster, G. Parraga, and J. Bax, "Three-dimensional ultrasound scanning," *Interface Focus*, vol. 1, no. 4, p. 503, 2011.

76. A. Fenster and D. Downey, "Three-dimensional ultrasound imaging," *Annual Review of Biomedical Engineering*, vol. 2, no. 1, p. 457–475, 2000.

77. D. Robinson and P. Knight, "Interpolation scan conversion in pulse-echo ultrasound," *Ultrasonic Imaging*, vol. 4, no. 4, pp. 297–310, Oct. 1982. [Online]. Available: http://www.sciencedirect.com/science/article/pii/0161734682900141

78. S.-W. Lee and S.-B. Park, "A new scan conversion algorithm for ultrasound compound scanning," *Ultrasonic imaging*, vol. 7, no. 3, p. 215–224, 1985. [Online]. Available: http://www.sciencedirect.com/science/article/pii/0161734685900021

79. A. P. Berkhoff, H. J. Huisman, J. M. Thijssen, E. M. G. P. Jacobs, and R. J. F. Homan, "Fast scan conversion algorithms for displaying ultrasound sector images," *Ultrasonic Imaging*, vol. 16, no. 2, pp. 87–108, Apr. 1994. [Online]. Available: http://uix.sagepub.com/content/16/2/87

80. M. Zhao and S. Mo, "A GPU based high-definition ultrasound digital scan conversion algorithm," in *SPIE Medical Imaging*, 2010, p. 76252M–76252M. [Online]. Available: http://proceedings.spiedigitallibrary.org/proceeding.aspx?articleid=747991

81. S. Dymling, H. Persson, and C. Hertz, "Measurement of blood perfusion in tissue using Doppler ultrasound," *Ultrasound in Medicine & Biology*, vol. 17, no. 5, p. 433–444, 1991.

82. D. Baker, "Pulsed ultrasonic Doppler blood-flow sensing," *Sonics and Ultrasonics, IEEE Transactions on*, vol. 17, no. 3, pp. 170 – 184, Jul. 1970.

83. P. Embree and W. O'Brien Jr, "Pulsed Doppler accuracy assessment due to frequency-dependent attenuation and rayleigh scattering error sources," *IEEE Transactions on Biomedical Engineering*, vol. 37, no. 3, p. 322–326, 1990.

84. C. Kasai, K. Namekawa, A. Koyano, and R. Omoto, "Real-time two-dimensional blood flow imaging using an autocorrelation technique," *IEEE Trans. Sonics Ultrason*, vol. 32, no. 3, p. 458–464, 1985.

85. J. Jensen, *Estimation of blood velocities using ultrasound: A signal processing approach*. Cambridge Univ Pr, 1996.

86. K. W. Ferrara, J. G. Mottley, R. L. Goldberg, and S. W. Smith, "Ultrasound," in *The Biomedical Engineering Handbook, Second Edition. 2 Volume Set*, ser. Electrical Engineering Handbook. CRC Press, Dec. 1999. [Online]. Available: http://dx.doi.org/10.1201/9781420049510.ch65

87. J. Rubin, R. Bude, P. Carson, R. Bree, and R. Adler, "Power Doppler US: a potentially useful alternative to mean frequency-based color Doppler US." *Radiology*, vol. 190, no. 3, p. 853, 1994.

88. A. Welsh, "Quantification of power Doppler and the index "fractional moving blood volume" (FMBV)," *Ultrasound in Obstetrics and Gynecology*, vol. 23, no. 4, p. 323–326, 2004.

89. J. Noguchi, K. Hata, H. Tanaka, and T. Hata, "Placental vascular sonobiopsy using three-dimensional power Doppler ultrasound in normal and growth restricted fetuses," *Placenta*, vol. 30, no. 5, p. 391–397, 2009.

90. S. Collins, J. Birks, G. Stevenson, A. Papageorghiou, J. Noble, and L. Impey, "Measurement of the spiral artery jets: general principles and differences observed for small for gestational age (SGA) babies," *Ultrasound in Obstetrics & Gynecology*, vol. 40, pp. 171–178, 2012. [Online]. Available: http://dx.doi.org/10.1002/uog.10149

91. N. Jones, N. Raine-Fenning, E. Bradley, and G. Bugg, "Placental 3-d power Doppler angiography-regional variation and reliability of two ultrasonic sphere biopsy techniques," *Ultrasound in Medicine and Biology*, vol. 37, no. 3, p. 364–375, 2011.

92. R. Matijevic, J. Meekins, S. Walkinshaw, J. Neilson, and I. McFadyen, "Spiral artery blood flow in the central and peripheral areas of the placental bed in the second trimester," *Obstetrics & Gynecology*, vol. 86, no. 2, p. 289–292, 1995.

93. Ü. Özkaya, S. Özkan, S. Özeren, and A. Çorakçı, "Doppler examination of uteroplacental circulation in early pregnancy: Can it predict adverse outcome?" *Journal of Clinical Ultrasound*, vol. 35, no. 7, pp. 382–386, 2007.

94. A. Kurjak, J. Dudenhausen, T. Hafner, S. Kupesic, V. Latin, and M. Kos, "Intervillous circulation in all three trimesters of normal pregnancy assessed by color Doppler," *Journal of Perinatal Medicine-Official Journal of the WAPM*, vol. 25, no. 4, p. 373–380, 1997.

95. D. Jurkovic, E. Jauniaux, A. Kurjak, J. Hustin, S. Campbell, and K. Nicolaides, "Transvaginal color Doppler assessment of the uteroplacental circulation in early pregnancy," *Obstetrics & Gynecology*, vol. 77, no. 3, p. 365, 1991.

96. Y. Hsieh, C. Chang, H. Tsai, C. Lee, and C. Tsai, "Longitudinal Doppler sonographic measurements of vascular impedance in the central and peripheral spiral arteries throughout pregnancy," *Journal of Clinical Ultrasound*, vol. 28, no. 2, p. 78–82, 2000.

97. T. Murakoshi, N. Sekizuka, K. Takakuwa, H. Yoshizawa, and K. Tanaka, "Uterine and spiral artery flow velocity waveforms in pregnancy-induced hypertension and/or intrauterine growth retardation," *Ultrasound in Obstetrics & Gynecology*, vol. 7, no. 2, p. 122–128, 1996.

98. N. W. Jones, N. Raine-Fenning, H. Mousa, E. Bradley, and G. Bugg, "Evaluation of the intraobserver and interobserver reliability of data acquisition for three-dimensional power Doppler angiography of the whole placenta at 12 weeks gestation," *Ultrasound in Medicine & Biology*, vol. 36, no. 9, pp. 1405 – 1411, 2010.

99. W. P. Martins, A. W. Welsh, J. C. Lima, C. O. Nastri, and N. J. Raine-Fenning, "The "Volumetric" pulsatility index as evaluated by spatio-temporal imaging correlation (STIC): a preliminary description of a novel technique, its application to the endometrium and an evaluation of its reproducibility," *Ultrasound in Medicine & Biology*, vol. 33, pp. 333–333, 2011.

100. P. Lai, Y. Wang, and A. Welsh, "Reproducibility of regional placental vascularity/perfusion measurement using 3D power Doppler," *Ultrasound in Obstetrics & Gynecology*, vol. 36, no. 2, p. 202–209, 2010.

101. M. Turk and A. Pentland, "Face recognition using eigenfaces," in *Computer Vision and Pattern Recognition, 1991. Proceedings CVPR'91., IEEE Computer Society Conference on*, 1991, p. 586–591.

102. J. Daugman, "How iris recognition works," *Circuits and Systems for Video Technology, IEEE Transactions on*, vol. 14, no. 1, p. 21–30, 2004.

103. C. Papageorgiou and T. Poggio, "Trainable pedestrian detection," in *Image Processing, 1999. ICIP 99. Proceedings. 1999 International Conference on*, vol. 4, 1999, p. 35–39.

104. L. Shapiro and G. Stockman, *Computer Vision*. Prentice Hall, 2001.

105. M. Kass, A. Witkin, and D. Terzopoulos, "Snakes: Active contour models," *International Journal of Computer Vision*, vol. 1, no. 4, p. 321–331, 1988.

106. V. Caselles, R. Kimmel, and G. Sapiro, "Geodesic active contours," *International Journal of Computer Vision*, vol. 22, no. 1, p. 61–79, 1997.

107. S. Zhu and A. Yuille, "Region competition," *IEEE Trans. on Pattern Analysis and Machine Intelligence*, vol. 18, no. 9, p. 884–900, 1996.

108. J. Sethian *et al.*, "Level set methods and fast marching methods," *Journal of Computing and Information Technology*, vol. 11, no. 1, p. 1–2, 2003.

109. Y. Boykov and M. Jolly, "Interactive graph cuts for optimal boundary and region segmentation of objects in ND images," in *International Conference on Computer Vision*, vol. 1, 2001, p. 105–112.

110. Y. Boykov, O. Veksler, and R. Zabih, "Fast approximate energy minimization via graph cuts," *Pattern Analysis and Machine Intelligence, IEEE Transactions on*, vol. 23, no. 11, p. 1222–1239, 2001.

111. L. Grady, "Random walks for image segmentation," *IEEE Trans. on Pattern Analysis and Machine Intelligence*, vol. 28, no. 11, p. 1768–1783, 2006.

112. J. Udupa and S. Samarasekera, "Fuzzy connectedness and object definition: theory, algorithms, and applications in image segmentation," *Graphical Models and Image Processing*, vol. 58, no. 3, p. 246–261, 1996.

113. E. Mortensen and W. Barrett, "Intelligent scissors for image composition," in *Proceedings of the 22nd annual conference on Computer Graphics and Interactive Techniques*, 1995, p. 191–198.

114. A. Falcão, J. Udupa, S. Samarasekera, S. Sharma, B. Hirsch, and R. Lotufo, "User-steered image segmentation paradigms: Live wire and live lane," *Graphical Models and Image Processing*, vol. 60, no. 4, p. 233–260, 1998.

115. A. Squillacote and D. DeMarle, *The ParaView Guide*. Kitware, 2006.

116. J. Miller, "Volume rendering in three-dimensional display of SPECT images," in *J. Nucl. Med*, 1990.

117. Y. Sato, N. Shiraga, S. Nakajima, S. Tamura, and R. Kikinis, "Local maximum intensity projection (LMIP): a new rendering method for vascular visualization," *Journal of Computer Assisted Tomography*, vol. 22, no. 6, p. 912, 1998.

118. S. Campbell, C. Lees, G. Moscoso, and P. Hall, "Ultrasound antenatal diagnosis of cleft palate by a new technique: the 3D reverse face view," *Ultrasound in Obstetrics & Gynecology*, vol. 25, no. 1, p. 12–18, 2005.

119. M. Meißner, H. Pfister, R. Westermann, and C. Wittenbrink, "Volume visualization and volume rendering techniques," *Eurographics tutorial*, 2000.

120. G. DeVore and B. Polanko, "Tomographic ultrasound imaging of the fetal heart," *Journal of Ultrasound in Medicine*, vol. 24, no. 12, p. 1685–1696, 2005.

121. G. Rizzo, A. Capponi, M. Pietrolucci, A. Capece, E. Aiello, S. Mammarella, and D. Arduini, "An algorithm based on OmniView technology to reconstruct sagittal and coronal planes of the fetal brain from volume datasets acquired by three-dimensional ultrasound," *Ultrasound in Obstetrics & Gynecology*, vol. 38, pp. 152–164, 2011.

122. O. Bleker, G. Kloosterman, W. Breur, and D. Mieras, "The volumetric growth of the human placenta: a longitudinal ultrasonic study." *American Journal of Obstetrics and Gynecology*, vol. 127, no. 6, p. 657, 1977.

123. H. Hoogland, J. De Haan, and C. Martin Jr, "Placental size during early pregnancy and fetal outcome: a preliminary report of a sequential ultrasonographic study." *American Journal of Obstetrics and Gynecology*, vol. 138, no. 4, p. 441, 1980.

124. H. Wolf, H. Oosting, and P. Treffers, "A longitudinal study of the relationship between placental and fetal growth as measured by ultrasonography." *American Journal of Obstetrics and Gynecology*, vol. 161, no. 5, p. 1140, 1989.

125. ——, "Second-trimester placental volume measurement by ultrasound: prediction of fetal outcome." *American Journal of Obstetrics and Gynecology*, vol. 160, no. 1, p. 121, 1989.

126. J. Noble, "Ultrasound image segmentation and tissue characterization," *Proceedings of the Institution of Mechanical Engineers, Part H: Journal of Engineering in Medicine*, vol. 224, no. 2, p. 307, 2010.

127. G. Carneiro, B. Georgescu, S. Good, and D. Comaniciu, "Detection and measurement of fetal anatomies from ultrasound images using a constrained probabilistic boosting tree," *Medical Imaging, IEEE Transactions on*, vol. 27, no. 9, p. 1342–1355, 2008.

128. V. Lempitsky, M. Verhoek, J. Noble, and A. Blake, *Random forest classification for automatic delineation of myocardium in real-time 3D echocardiography*. Springer, 2009, vol. 5528.

129. M. Yaqub, M. Javaid, C. Cooper, and J. Noble, "Improving the classification accuracy of the classic RF method by intelligent feature selection and weighted voting of trees with application to medical image segmentation," *Machine Learning in Medical Imaging*, vol. 7009/2011, p. 184–192, 2011.

130. S. Rueda, C. Knight, A. Papageorghiou, and J. Noble, "Local phase-based fuzzy connectedness segmentation of ultrasound images." in *Proc. Medical Image Understanding and Analysis*, 2011, pp. 331–335.

131. P. Foroughi and P. Abolmaesumi, "Elastic registration of 3D ultrasound images," *Medical Image Computing and Computer-Assisted Intervention–MICCAI 2005*, vol. 3349, p. 83–90, 2005.

132. K. Rajpoot, J. Noble, V. Grau, C. Szmigielski, and H. Becher, "Multiview RT3D echocardiography image fusion," in *Functional Imaging and Modeling of the Heart: 5th International Conference, FIMH 2009 Nice, France, June 3-5, 2009 Proceedings*, vol. 5528, 2009, p. 134.

133. K. M. Elsayes, A. T. Trout, A. M. Friedkin, P. S. Liu, R. O. Bude, J. F. Platt, and C. O. Menias, "Imaging of the placenta: A multimodality pictorial review," *Radiographics*, vol. 29, no. 5, p. 1371 –1391, 2009. [Online]. Available: http://radiographics.rsna.org/content/29/5/1371.abstract

134. E. Hafner, T. Philipp, K. Schuchter, B. Dillinger-Paller, K. Philipp, and P. Bauer, "Second-trimester measurements of placental volume by three-dimensional ultrasound to predict small-for-gestational-age infants," *Ultrasound in Obstetrics and Gynecology*, vol. 12, no. 2, pp. 97–102, 1998.

135. E. Hafner, M. Metzenbauer, B. Dillinger-Paller, D. Hoefinger, K. Schuchter, H. Sommer-Wagner, and K. Philipp, "Correlation of first trimester placental volume and second trimester uterine artery Doppler flow," *Placenta*, vol. 22, no. 8-9, p. 729–734, 2001.

136. N. Raine-Fenning, J. Clewes, N. Kendall, A. Bunkheila, B. Campbell, and I. Johnson, "The interobserver reliability and validity of volume calculation from three-dimensional ultrasound datasets in the in vitro setting," *Ultrasound in Obstetrics and Gynecology*, vol. 21, no. 3, pp. 283–91, 2003.

137. P. Nowak, L. Nardozza, E. Araujo Júnior, L. Rolo, and A. Moron, "Comparison of placental volume in early pregnancy using multiplanar and VOCAL methods," *Placenta*, vol. 29, no. 3, p. 241–245, 2008.

138. K. Cheong, K. Leung, T. Li, H. Chan, Y. Lee, and M. Tang, "Comparison of inter- and intraobserver agreement and reliability between three different types of placental volume measurement technique (XI VOCAL, VOCAL and multiplanar) and validity in the in-vitro setting," *Ultrasound in Obstetrics and Gynecology*, vol. 36, no. 2, p. 210–217, 2010.

139. E. de Sa Barreto, H. Milani, E. Junior, K. Haratz, L. Rolo, L. Nardozza, and A. Moron, "Reliability and validity of in vitro volume calculations by 3-dimensional ultrasonography using the multiplanar, virtual organ computer-aided analysis (VOCAL), and extended imaging VOCAL methods," *Journal of Ultrasound in Medicine*, vol. 29, no. 5, p. 767, 2010.

140. M. Metzenbauer, E. Hafner, D. Hoefinger, K. Schuchter, G. Stangl, E. Ogris, and K. Philipp, "Three-dimensional ultrasound measurement of the placental volume in early pregnancy: method and correlation with biochemical placenta parameters," *Placenta*, vol. 22, no. 6, p. 602–605, 2001.

141. K. Schuchter, M. Metzenbauer, E. Hafner, and K. Philipp, "Uterine artery Doppler and placental volume in the first trimester in the prediction of pregnancy complications." *Ultrasound in Obstetrics & Gynecology*, vol. 18, no. 6, p. 590, 2001.

142. M. Metzenbauer, E. Hafner, K. Schuchter, and K. Philipp, "First-trimester placental volume as a marker for chromosomal anomalies: preliminary results from

an unselected population." *Ultrasound in Obstetrics & Gynecology: the official journal of the International Society of Ultrasound in Obstetrics and Gynecology*, vol. 19, no. 3, p. 240, 2002.

143. P. Wegrzyn, C. Faro, O. Falcon, C. Peralta, and K. Nicolaides, "Placental volume measured by three-dimensional ultrasound at 11 to 13+6 weeks of gestation: relation to chromosomal defects," *Ultrasound in Obstetrics & Gynecology*, vol. 26, no. 1, p. 28–32, 2005.

144. T. Wataganara, M. Metzenbauer, I. Peter, K. Johnson, and D. Bianchi, "Placental volume, as measured by 3-dimensional sonography and levels of maternal plasma cell-free fetal DNA," *American Journal of Obstetrics and Gynecology*, vol. 193, no. 2, p. 496–500, 2005.

145. L. Grady and E. Schwartz, "Anisotropic interpolation on graphs: The combinatorial dirichlet problem," Boston University, Tech. Rep., 2003.

146. L. Grady, *Random walk implementation*, 2011, [Online; accessed 25th February 2014]. [Online]. Available: http://cns.bu.edu/lgrady/

147. V. Developers, *VXL library homepage*, 2012, [Online; accessed 25th February 2014]. [Online]. Available: http://vxl.sourceforge.net/

148. G. Guennebaud, B. Jacob *et al.*, *Eigen version 3.0.5*, 2010, [Online; accessed 25th February 2014]. [Online]. Available: http://eigen.tuxfamily.org

149. H. Van der Vorst, "Bi-CGSTAB: a fast and smoothly converging variant of bi-CG for the solution of nonsymmetric linear systems," *SIAM Journal on scientific and Statistical Computing*, vol. 13, p. 631, 1992.

150. K. Rupp, J. Weinbub, and F. Rudolf, "Automatic performance optimization in ViennaCL for GPUs," in *Proceedings of the 9th Workshop on Parallel/High-Performance Object-Oriented Scientific Computing*, 2010, p. 6.

151. P. A. Yushkevich, J. Piven, H. Cody Hazlett, R. Gimpel Smith, S. Ho, J. C. Gee, and G. Gerig, "User-guided 3D active contour segmentation of anatomical structures: Significantly improved efficiency and reliability," *Neuroimage*, vol. 31, no. 3, p. 1116–1128, 2006.

152. J. Martin Bland and D. Altman, "Statistical methods for assessing agreement between two methods of clinical measurement," *The Lancet*, vol. 327, no. 8476, p. 307–310, 1986.

153. R. D. C. Team, *R: A Language and Environment for Statistical Computing*, Vienna, Austria, 2011. [Online]. Available: http://www.R-project.org/

154. M. Gamer, J. Lemon, I. Fellows, and P. Singh, *irr: Various Coefficients of Interrater Reliability and Agreement*, 2010, R package version 0.83. [Online]. Available: http://CRAN.R-project.org/package=irr

155. H. Bayliss, D. Churchill, M. Beevers, and D. Beevers, "Anti-hypertensive drugs in pregnancy and fetal growth: evidence for pharmacological programming in the first trimester?" *Hypertension in pregnancy*, vol. 21, no. 2, p. 161–174, 2002.

156. P. Loughna, L. Chitty, T. Evans, and T. Chudleigh, "Fetal size and dating: charts recommended for clinical obstetric practice," *Ultrasound*, vol. 17, no. 3, p. 160–166, 2009.

157. B. Petersen and D. Honigmann, "Blood flow in its context: Combining 3D b-mode and color Doppler ultrasonic data," *Visualization and Computer Graphics, IEEE Transactions on*, vol. 13, no. 4, p. 748–757, 2007.

158. W. P. Martins, "Three–dimensional power Doppler: validity and reliability," *Ultrasound in Obstetrics & Gynecology*, vol. 36, no. 5, p. 530–533, Nov. 2010.

159. M. J. Kudla and J. L. Alcázar, "Does sphere volume affect the performance of three-dimensional power Doppler virtual vascular sampling for predicting malignancy in vascularized solid or cysticsolid adnexal masses?" *Ultrasound in Obstetrics & Gynecology*, vol. 35, no. 5, p. 602–608, May 2010. [Online]. Available: http://onlinelibrary.wiley.com/doi/10.1002/uog.7601/abstract

160. K. Hormann, B. Lévy, A. Sheffer *et al.*, *Mesh parameterization: Theory and practice*. Citeseer, 2007.

161. J. Maillot, H. Yahia, and A. Verroust, "Interactive texture mapping," in *Proceedings of the 20th annual conference on Computer graphics and interactive techniques*, 1993, p. 27–34.

162. B. Lévy and J. Mallet, "Non-distorted texture mapping for sheared triangulated meshes," in *Proceedings of the 25th annual conference on Computer graphics and interactive techniques*, 1998, p. 343–352.

163. A. Lee, W. Sweldens, P. Schröder, L. Cowsar, and D. Dobkin, "MAPS: multiresolution adaptive parameterization of surfaces," in *Proceedings of the 25th annual conference on Computer graphics and interactive techniques*, 1998, p. 95–104.

164. K. Hormann, "MIPS: An efficient global parametrization method," DTIC Document, Tech. Rep., 2000.

165. S. Haker, S. Angenent, A. Tannenbaum, R. Kikinis, G. Sapiro, and M. Halle, "Conformal surface parameterization for texture mapping," *Visualization and Computer Graphics, IEEE Transactions on*, vol. 6, no. 2, p. 181–189, 2000.

166. S. Halier, S. Angenent, A. Tannenbaurn, and R. Kikinis, "Nondistorting flattening maps and the 3D visualization of colon CT images," *Medical Imaging, IEEE Transactions on*, vol. 19, no. 7, p. 665–670, 2000.

167. W. Hong, X. Gu, F. Qiu, M. Jin, and A. Kaufman, "Conformal virtual colon flattening," in *Proceedings of the 2006 ACM symposium on Solid and physical modeling*, 2006, p. 85–93.

168. A. Sheffer, E. Praun, and K. Rose, "Mesh parameterization methods and their applications," *Foundations and Trends in Com. Graphics and Vision*, vol. 2, no. 2, p. 105–171, 2006.

169. W. Tutte, "How to draw a graph," *Proc. London Math. Soc*, vol. 13, no. 3, p. 743–768, 1963.

170. E. Wachspress, *A rational finite element basis*. Academic Press, 1975, vol. 114.

171. M. Eck, T. DeRose, T. Duchamp, H. Hoppe, M. Lounsbery, and W. Stuetzle, "Multiresolution analysis of arbitrary meshes," in *Proceedings of the 22nd annual conference on Computer graphics and interactive techniques*, 1995, p. 173–182.

172. M. Floater, "Mean value coordinates," *Computer Aided Geometric Design*, vol. 20, no. 1, p. 19–27, 2003.

173. M. Desbrun, M. Meyer, and P. Alliez, "Intrinsic parameterizations of surface meshes," in *Computer Graphics Forum*, vol. 21, 2002, p. 209–218.

174. U. Pinkall and K. Polthier, "Computing discrete minimal surfaces and their conjugates," *Experimental Mathematics*, vol. 2, no. 1, p. 15–36, 1993.

175. R. Haralick, S. Sternberg, and X. Zhuang, "Image analysis using mathematical morphology," *Pattern Analysis and Machine Intelligence, IEEE Transactions on*, vol. 9, no. 4, p. 532–550, 1987.

176. W. Lorensen and H. Cline, "Marching cubes: A high resolution 3D surface construction algorithm," in *ACM Siggraph Computer Graphics*, vol. 21, 1987, p. 163–169.

177. C. Dietrich, C. Scheidegger, J. Schreiner, J. Comba, L. Nedel, and C. Silva, "Edge transformations for improving mesh quality of marching cubes," *Visualization and Computer Graphics, IEEE Transactions on*, vol. 15, no. 1, p. 150–159, 2009.

178. S. Collins, G. Stevenson, J. Noble, and L. Impey, "Developmental changes in spiral artery blood flow in the human placenta observed with colour Doppler ultrasonography," *Placenta*, vol. 33, pp. 782–787, 2012.

179. D. Pretorius, T. Nelson, R. Baergen, E. Pai, and C. Cantrell, "Imaging of placental vasculature using three-dimensional ultrasound and color power Doppler: a preliminary study," *Ultrasound in Obstetrics and Gynecology*, vol. 12, no. 1, p. 45–49, 1998.

180. R. Greenberg, G. Taylor, J. Stapleton, C. Hillsley, and D. Spinak, "Analysis of regional cerebral blood flow in dogs, with an experimental microbubble-based US contrast agent." *Radiology*, vol. 201, no. 1, p. 119–123, 1996.

181. G. Taylor, "Regional cerebral blood flow estimates in newborn lamb using amplitude-mode color Doppler ultrasound," *Pediatric Radiology*, vol. 26, no. 4, p. 282–286, 1996.

182. A. Schuster, F. Frauscher, H. Strasser, W. Recheis, L. Pallwein, R. Herwig, G. Bartsch, D. z. Nedden, and G. M. Pinggera, "Power Doppler ultrasound imaging for quantification of urinary bladder neck blood flow changes," *Ultrasound in Medicine and Biology*, vol. 30, no. 10, pp. 1379 – 1384, 2004. [Online]. Available: http://www.sciencedirect.com/science/article/pii/S030156290400211X

183. S. Pinter and J. Lacefield, "Objective selection of high-frequency power Doppler wall filter cutoff velocity for regions of interest containing multiple small vessels," *Medical Imaging, IEEE Transactions on*, vol. 29, no. 5, p. 1124–1139, 2010.

184. J. Rubin, R. Bude, J. Fowlkes, R. Spratt, P. Carson, and R. Adler, "Normalizing fractional moving blood volume estimates with power Doppler US: defining a stable intravascular point with the cumulative power distribution function." *Radiology*, vol. 205, no. 3, p. 757, 1997.

185. J. Rubin, R. Adler, J. Fowlkes, S. Spratt, J. Pallister, J. Chen, and P. Carson, "Fractional moving blood volume: estimation with power Doppler US." *Radiology*, vol. 197, no. 1, p. 183, 1995.

186. E. Hernandez-Andrade, A. Thuring-Jönsson, T. Jansson, G. Lingman, and K. Marsál, "Fractional moving blood volume estimation in the fetal lung using power Doppler ultrasound: a reproducibility study," *Ultrasound in Obstetrics and Gynecology*, vol. 23, no. 4, pp. 369–373, 2004.

187. E. Hernandez-Andrade, T. Jansson, D. Ley, M. Bellander, M. Persson, G. Lingman, and K. Marsál, "Validation of fractional moving blood volume measurement with power Doppler ultrasound in an experimental sheep model," *Ultrasound in Obstetrics and Gynecology*, vol. 23, no. 4, pp. 363–368, 2004.

188. E. Hernandez-Andrade, T. Jansson, H. Figueroa-Diesel, H. Rangel-Nava, R. Acosta-Rojas, and E. Gratacos, "Evaluation of fetal regional cerebral blood perfusion using power Doppler ultrasound and the estimation of fractional moving blood volume," *Ultrasound in Obstetrics and Gynecology*, vol. 29, no. 5, pp. 556–561, 2007.

189. A. Welsh, J. Rubin, J. Fowlkes, and N. Fisk, "Standardization of power Doppler quantification of blood flow in the human fetus using the aorta and inferior vena cava," *Ultrasound in Obstetrics and Gynecology*, vol. 26, no. 1, p. 33–43, 2005.

190. H. Pairleitner, H. Steiner, G. Hasenoehrl, and A. Staudach, "Three–dimensional power Doppler sonography: imaging and quantifying blood flow and vascularization," *Ultrasound in Obstetrics & Gynecology*, vol. 14, no. 2, p. 139–143, Aug. 1999. [Online]. Available: http://onlinelibrary.wiley.com/doi/10.1046/j.1469-0705.1999.14020139.x/abstract

191. J. L. Alcázar, "Three-dimensional power Doppler derived vascular indices: what are we measuring and how are we doing it?" *Ultrasound in Obstetrics & Gynecology*, vol. 32, no. 4, p. 485–487, Sep. 2008. [Online]. Available: http://onlinelibrary.wiley.com/doi/10.1002/uog.6144/abstract

192. A. Welsh, "A caution regarding standardization of power Doppler to measure perfusion in placental tissue," *Ultrasound in Obstetrics and Gynecology*, vol. 31, no. 1, p. 111–112, 2008.

193. ——, "The questionable value of VOCAL indices of perfusion," *Ultrasound in Obstetrics and Gynecology*, vol. 36, no. 1, p. 126–127, 2010.

194. W. P. Martins and N. J. Raine-Fenning, "Analysis and acquisition reproducibility of 3D power Doppler," *Ultrasound in Obstetrics & Gynecology*, vol. 36, no. 3, p. 392–393, Sep. 2010. [Online]. Available: http://onlinelibrary.wiley.com/doi/10.1002/uog.7757/abstract

195. N. Jones, E. Hutchinson, P. Brownbill, I. Crocker, D. Eccles, G. Bugg, and N. Raine-Fenning, "In vitro dual perfusion of human placental lobules as a flow phantom to investigate the relationship between fetoplacental flow and quantitative 3D power Doppler angiography," *Placenta*, vol. 30, no. 2, p. 130–135, Feb. 2009. [Online]. Available: http://www.sciencedirect.com/science/article/pii/S0143400408003688

196. N. J. Raine-Fenning, N. M. Nordin, K. V. Ramnarine, B. K. Campbell, J. S. Clewes, A. Perkins, and I. R. Johnson, "Determining the relationship between three–dimensional power Doppler data and true blood flow characteristics: an *in-vitro* flow phantom experiment," *Ultrasound in Obstetrics & Gynecology*, vol. 32, no. 4, p. 540–550, 2008. [Online]. Available: http://onlinelibrary.wiley.com/doi/10.1002/uog.6110/abstract

197. O. Morel, F. Pachy, P. Chavatte-Palmer, M. Bonneau, E. Gayat, P. Laigre, D. Evain–Brion, and V. Tsatsaris, "Correlation between uteroplacental three-dimensional power Doppler indices and true uterine blood flow: evaluation in a pregnant sheep model," *Ultrasound in Obstetrics & Gynecology*, vol. 36, no. 5, p. 635–640, Nov. 2010. [Online]. Available: http://onlinelibrary.wiley.com/doi/10.1002/uog.7741/abstract

198. N. J. Raine-Fenning, N. M. Nordin, K. V. Ramnarine, B. K. Campbell, J. S. Clewes, A. Perkins, and I. R. Johnson, "Evaluation of the effect of machine settings on quantitative three-dimensional power Doppler angiography: an *in-vitro* flow phantom experiment," *Ultrasound in Obstetrics & Gynecology*, vol. 32, no. 4, p. 551–559, Sep. 2008. [Online]. Available: http://onlinelibrary.wiley.com/doi/10.1002/uog.6138/abstract

199. M. Schulten-Wijman, P. Struijk, C. Brezinka, N. De Jong, and E. Steegers, "Evaluation of volume vascularization index and flow index: a phantom study," *Ultrasound in Obstetrics & Gynecology*, vol. 32, no. 4, p. 560–564, 2008.

200. W. Martins, N. Raine-Fenning, R. Ferriani, and C. Nastri, "Quantitative three-dimensional power Doppler angiography: a flow-free phantom experiment to evaluate the relationship between color gain, depth and signal artifact," *Ultrasound in Obstetrics & Gynecology*, vol. 35, no. 3, p. 361–368, 2010.

201. S. Collins, G. Stevenson, J. Noble, L. Impey, and A. Welsh, "Influence of power Doppler gain setting on virtual organ computer AnaLysis (VOCAL\tm) indices in vivo: Can use of the individual sub-noise gain (SNG) level optimise information?" *Ultrasound in Obstetrics & Gynecology*, vol. 40, no. 1, pp. 75–80, 2011.

202. A. Welsh, P. Lai, and A. Wang, "Reply," *Ultrasound in Obstetrics & Gynecology*, vol. 36, no. 3, p. 393–394, Sep. 2010. [Online]. Available: http://onlinelibrary.wiley.com/doi/10.1002/uog.7759/abstract

203. J. Bello-Muñoz, "Volume perfusion index (VPI): developing a new tool for measuring fetal blood flow by using four dimensional ultrasound and power Doppler signal," Ph.D. dissertation, Universitat Autonoma De Barcelona, 2012.

204. S. Gudmundsson, L. Valentin, J. Pirhonen, P. Olofsson, M. Dubiel, and K. Marsál, "Factors affecting color Doppler energy ultrasound recordings in an in-vitro model," *Ultrasound in Medicine & Biology*, vol. 24, no. 6, p. 899–902, 1998.

205. M. Dubiel, A. Hammid, A. Breborowicz, M. Pietryga, P. Sladkevicius, P. Olofsson, G. Breborowicz, and S. Gudmundsson, "Flow index evaluation of 3-D volume flow images: An *in vivo* and *in vitro* study," *Ultrasound in Medicine and Biology*, vol. 32, no. 5, p. 665–671, 2006.

206. J. Alcázar, D. Rodriguez, P. Royo, R. Galván, S. Ajossa, and S. Guerriero, "Intraobserver and interobserver reproducibility of 3-dimensional power Doppler vascular indices in assessment of solid and cystic-solid adnexal masses," *Journal of Ultrasound in Medicine*, vol. 27, no. 1, p. 1–6, 2008.

207. H. Guimarães Filho, R. Mattar, E. Araujo Júnior, L. da Costa, C. de Mello Junior, L. Nardozza, P. Nowak, and A. Moron, "Reproducibility of three-dimensional power Doppler placental vascular indices in pregnancies between 26 and 35 weeks," *Archives of gynecology and obstetrics*, vol. 283, no. 2, p. 213–217, 2011.

208. G. Rizzo and A. Capponi, "Effects of chorionic villus sampling on placental hemodynamic assessed by three-dimensional power Doppler ultrasonography," *Prenatal Diagnosis*, vol. 27, no. 6, p. 581–582, 2007.

209. C. Guiot, P. Gaglioti, M. Oberto, E. Piccoli, R. Rosato, and T. Todros, "Is three-dimensional power Doppler ultrasound useful in the assessment of placental perfusion in normal and growth-restricted pregnancies?" *Ultrasound in Obstetrics and Gynecology*, vol. 31, no. 2, pp. 171–176, 2008.

210. M. Tuuli, M. Houser, L. Odibo, K. Huster, G. Macones, and A. Odibo, "Validation of placental vascular sonobiopsy for obtaining representative placental vascular indices by three-dimensional power Doppler ultrasonography," *Placenta*, vol. 31, no. 3, p. 192–196, 2010.

211. E. Hafner, M. Metzenbauer, I. Stümpflen, T. Waldhör, and K. Philipp, "First trimester placental and myometrial blood perfusion measured by 3D power Doppler in normal and unfavourable outcome pregnancies," *Placenta*, vol. 31, no. 9, p. 756–763, 2010.

212. S. Collins, J. Birks, A. Papageorghiou, G. Stevenson, and L. Impey, "Direct measurement of blood flow into the intervillous space and its relationship with uterine artery blood flow," *ISUOG*, vol. 36, no. S1, p. 34, 2010.

213. C. Martinoli, L. Derchi *et al.*, "Gain setting in power Doppler US." *Radiology*, vol. 202, no. 1, p. 284, 1997.

214. F. Martini and W. Ober, *Fundamentals of anatomy and physiology*. Prentice Hall, 2001. [Online]. Available: http://books.google.com.au/books?id=EZt8QgAACAAJ

215. L. Chang, K. Chua, Y. Yong, and R. Sivasamboo, "Some hematological differences between the blood of mothers and their newborn infants." *Singapore Medical Journal*, vol. 13, no. 6, p. 280, 1972.

216. J. Jopling, E. Henry, S. Wiedmeier, and R. Christensen, "Reference ranges for hematocrit and blood hemoglobin concentration during the neonatal period: data from a multihospital health care system," *Pediatrics*, vol. 123, no. 2, p. e333–e337, 2009.

217. R. Christensen, E. Henry, J. Jopling, and S. Wiedmeier, "The CBC: reference ranges for neonates," in *Seminars in Perinatology*, vol. 33, 2009, p. 3–11.

218. K. Shung, G. Cloutier, and C. Lim, "The effects of hematocrit, shear rate, and turbulence on ultrasonic Doppler spectrum from blood," *IEEE Transactions on Biomedical Engineering*, vol. 39, no. 5, p. 462–469, 1992.

219. L. Mo and R. Cobbold, "A unified approach to modeling the backscattered Doppler ultrasound from blood," *IEEE Transactions on Biomedical Engineering*, vol. 39, no. 5, p. 450–461, 1992.

220. O. Linderkamp, P. Ozanne, P. Wu, and H. Meiselman, "Red blood cell aggregation in preterm and term neonates and adults," *Pediatric Research*, vol. 18, no. 12, p. 1356–1360, 1984.

221. O. Linderkamp, H. Versmold, K. Riegel, and K. Betke, "Contributions of red cells and plasma to blood viscosity in preterm and full-term infants and adults," *Pediatrics*, vol. 74, no. 1, p. 45–51, 1984.

222. C. Burchell, "Arterial blood flow in the human intervillous space." *American Journal of Obstetrics and Gynecology*, vol. 98, pp. 303–311, 1969.

223. *matplotlib version 1.1.0*, [Online; accessed 25th February 2014]. [Online]. Available: http://matplotlib.sourceforge.net/contents.html

224. *NumPy version 1.6.1*, [Online; accessed 25th February 2014]. [Online]. Available: http://numpy.scipy.org/

225. *Python(x,y) version 2.7.2*, [Online; accessed 25th February 2014]. [Online]. Available: http://code.google.com/p/pythonxy/

226. R. Jaffe and S. Warsof, "Color Doppler imaging in the assessment of uteroplacental blood flow in abnormal first trimester intrauterine pregnancies. an attempt to define etiologic mechanisms." *Journal of Ultrasound in Medicine*, vol. 11, no. 1, p. 41–44, 1992.

227. P. Schwärzler, D. Holden, S. Nielsen, M. Hahlin, P. Sladkevicius, and T. Bourne, "The conservative management of first trimester miscarriages and the use of colour Doppler sonography for patient selection," *Human Reproduction*, vol. 14, no. 5, p. 1341–1345, 1999.

228. S. Clark, P. Koonings, J. Phelan *et al.*, "Placenta previa/accreta and prior cesarean section." *Obstetrics and Gynecology*, vol. 66, no. 1, p. 89, 1985.

229. D. Miller, J. Chollet, and T. Goodwin, "Clinical risk factors for placenta previa–placenta accreta," *American Journal of Obstetrics and Gynecology*, vol. 177, no. 1, p. 210–214, 1997.

230. J. Shih, J. Jaraquemada, Y. Su, M. Shyu, C. Lin, S. Lin, and C. Lee, "Role of three-dimensional power Doppler in the antenatal diagnosis of placenta accreta: comparison with gray-scale and color Doppler techniques," *Ultrasound in Obstetrics & Gynecology*, vol. 33, no. 2, p. 193–203, 2009.